

DELFT UNIVERSITY OF TECHNOLOGY
FACULTY OF AEROSPACE ENGINEERING

Wind Tunnel Test AE2130-II
2020-2021

Test Date: 2nd December, 2020
Date of delivery: 29th March, 2022
Group #4
Assistant: Giulia Zoppini

Names	Initials	Student number	Email address
Walid Amezguiou	W.A.	5050995	W.Amezguiou@student.tudelft.nl
Bahier Khan	B.A.K.	5051908	B.A.Khan@student.tudelft.nl
Anibal Luciano Pastinante	A.L.P.	5010276	A.L.Pastinante@student.tudelft.nl
João Rodríguez	J.P.R.	4993578	J.P.RodriguezGordon@student.tudelft.nl
Oliver Ross	O.J.R	5008042	O.J.Ross@student.tudelft.nl
Oscar Rots	O.F.H.R.	5063345	O.F.H.Rots@student.tudelft.nl
Benjamin Slijper	B.C.S.	5051851	B.C.Slijper@student.tudelft.nl
Lorenz Veithen	L.A.V.	5075211	L.A.V.Veithen@student.tudelft.nl
Eliot Watson	E.J.C.W.	4993357	E.J.C.Watson@student.tudelft.nl
Niek Zandvliet	J.H.	4796403	J.H.Zandvliet@student.tudelft.nl

Approved:

by:

Summary

Every produced aircraft, flying millions of people and goods worldwide every year, relies on the design of many engineers to ensure safe and efficient flight conditions. But when it comes to aerodynamics, how does one verify the design before testing with humans, or large investment into flying prototypes which otherwise may not even function? The most common techniques include computer simulations and wind tunnels, but they are both open to errors, inaccuracies, or differences from the real world results, especially in the case of simulations. It is also possible to test an airfoil, when planform dimensions are not yet chosen, or to test a full wing where the planform design has been chosen at this point. Often, wind tunnels are fully booked and are too expensive or inaccessible. In this case, it is vital to understand the differences between simulations and experimental results in order to predict what the real world results may be.

This report aims to test, show results for, and compare the above tests for a NACA 64₂A – 015 airfoil, while also showing and explaining the key expected phenomena of the wing in each of the following cases:

- In the first case (the simulation case) the airfoil and wing are simulated in XFLR5, which is shown to overestimate the characteristics of the airfoil and wing due to simplifications, and underestimate the induced drag by the wing tip vortices in the finite wing case, as well as being unable to predict the effects of viscosity.
- In the second case (the experimental case) the airfoil is tested in the Low speed wind tunnel at the TU Delft. This case is much more accurate and capable of displaying characteristics including the stall characteristics of the wing than the simulation, especially in the airfoil case where the 2D simulation theory cannot predict separation or turbulence accurately.

Many flow phenomena were noted, and their occurrence with respect to angle of attack, location on the chord, and strength are compared and noted for each case. These include laminar and turbulent boundary layers, laminar separation bubbles, turbulent separation, stall, hysteresis, and flow reattachment. These phenomena are found and analysed using visible light cameras, electronic pressure scanners, infra red cameras and heat lamps, wake pressure rakes, and force balances.

These flow phenomena all have significant impact on the different polars observed for the airfoil and wing. The main findings were that a second linear part is initiated in the $C_{l/L} - \alpha$ curve, the sudden drop in lift and moment coefficient and increase in drag coefficient due to laminar stall. However, the above mentioned account more for the experiment than the simulation. For the simulation the main finding was that it is quite accurate until stall for the 2D airfoil analysis as for the airfoil analysis the program did account for the viscous effects. While for the wing the viscous effects were interpolated from the airfoil analysis leading to bigger differences.

It is advised to use a combination of all methods when testing a wing, so as to streamline and minimise costs, and since this report has shown that particularly for the 3D case, there are a number of vital characteristics especially in the critical stall regions, but also even in the cruise regions of angles of attack which are not accurately modelled in XFLR5 simulations. Nevertheless, when taking that into account while being in the preliminary phase of the design it can be used as a reasonable indication of what to expect.

Contents

Summary	i
List of Symbols	iv
List of Figures	v
List of Tables	vi
List of Abbreviations	vii
1 Introduction	1
2 Description of the Test Setup	2
2.1 Low Speed Wind Tunnel	2
2.2 Airfoil and Wing Models	2
2.2.1 2D model	3
2.2.2 3D model	3
2.3 Measurement Techniques	4
2.4 Variables	5
2.5 Methodology	5
3 Simulation Considerations	7
3.1 Background Information	7
3.1.1 Vortex Panel Method	7
3.1.2 Lifting-Line Theory, Vortex Lattice Method and 3D Panel Method	8
3.2 Limitations and Shortcoming of the Software	9
3.3 Details on the Analysis	11
3.3.1 Model of the Wing on XFLR5	11
3.3.2 Parameters used for the Simulation	13
4 Data Acquisition and Correction	15
4.1 Pressures Leading to 2D Coefficients	15
4.2 Balance Data Leading to 3D Coefficients	17
4.3 Velocity and Dynamic Pressure	18
4.4 Wall Corrections	18
4.4.1 Lift Interference	18
4.4.2 Model Blockage	19
4.4.3 Wake Blockage	20
4.4.4 Influence of the Wall Corrections on the Data	20
5 Results	22
5.1 Airfoil Analysis	22
5.1.1 Pressure Coefficient Graphs	22
5.1.2 C_l vs α Polar	25
5.1.3 C_d vs α Polar	29
5.1.4 C_l vs C_d Polar	30
5.1.5 C_l/C_d vs α Polar	31
5.1.6 C_m vs α Polar	32

5.1.7	Conclusion Airfoil Analysis	33
5.2	Wing Analysis	34
5.2.1	C_L vs α Polar	34
5.2.2	C_D vs α polar	39
5.2.3	C_L vs C_D Polar	40
5.2.4	C_L/C_D vs α Polar	41
5.2.5	C_M vs α Polar	42
5.2.6	Conclusion on the Wing Analysis	45
5.3	Flow Phenomena	46
5.3.1	Laminar Separation Bubble	46
5.3.2	Hysteresis	48
5.3.3	Tip vortices	49
5.4	Further Analysis	51
5.4.1	Comparison between 2D and 3D Wing	51
5.4.2	Comparison of Viscous and Inviscid Simulation in XFLR5	53
5.4.3	Transition Position from XFLR5	55
5.5	Comparison Experimental and Numerical Analysis	56

6 Conclusion and Recommendations	58
---	-----------

References	60
-------------------	-----------

A Pressure Coefficient Graphs

B Task Distribution

List of Symbols

Latin Letters	Quantity	Symbol Unit
A	Aspect ratio	[-]
A	Area (continuity)	[-]
c	Chord length	[m]
C_l	Airfoil lift coefficient	[-]
C_d	Airfoil drag coefficient	[-]
C_m	Airfoil moment coefficient	[-]
C_n	Normal coefficient	[-]
C_p	Pressure coefficient	[-]
C_{p_l}	Pressure coefficient lower side airfoil	[-]
C_{p_u}	Pressure coefficient upper side airfoil	[-]
C_L	Wing lift coefficient	[-]
C_D	Drag coefficient	[-]
C_{L_α}	Slope of the $C_L - \alpha$ curve	1/rad
D	Drag	N
e	Span efficiency factor	[-]
L	Lift	N
M	Mach number (compressibility)	[-]
M	Moment	Nm
N_{crit}	Measure of free flow turbulence	[-]
p	Pressure	Pa
p_0	Static Pressure	Pa
p_{tot}	Total Pressure	Pa
p_∞	Freestream Pressure	Pa
p_l	Pressure lower side airfoil	Pa
p_u	Pressure upper side airfoil	Pa
q	Dynamic pressure	Pa
q_∞	Freestream Dynamic pressure	Pa
S	Surface area	m^2
V	Velocity	ms^{-1}
V_∞	Freestream Velocity	ms^{-1}
V_i	Velocity vector on airfoil surface	ms^{-1}
n_i	Normal vector on airfoil surface	ms^{-1}
\mathcal{V}	Volume	m^3

Greek Letters	Quantity	Symbol Unit
α	Angle of Attack	deg
ρ	Density	kg/m^3
ν	Kinematic viscosity	$m^2 s^{-1}$

List of Figures

2.1	Test section room	2
2.2	Schematic of the wind tunnel	2
2.3	2D setup	3
2.4	2D setup drawing	3
2.5	3D setup including wake rake	3
2.6	3D setup drawing	3
2.7	Low Aspect Ratio Wing Model	4
2.8	Close view of wingtip	4
2.9	6-component balance	4
2.10	Ports electronic pressure scanner	4
2.11	Schematic of the 6-component balance	5
3.1	Depiction of flow-tangency condition [5]	8
3.2	A horseshoe vortex [7]	8
3.3	Xfoil and LLT with IBL loop vs. Panel method without IBL loop [9]	10
3.4	Example to represent that flat quad panels do not cover the surface entirely [9].	10
3.5	Numerical analysis vs Experimental DU 91-W2-250 airfoil	11
3.6	Diagram Depicting Wing Tip Rounding	12
3.7	Wing Model made on XFLR5	12
4.1	The forces acting on an airfoil [1]	15
4.2	Example of a pressure coefficient graph with the different parts indicated [12]	16
4.3	Drag analysis for a 2D-airfoil [1]	16
4.4	The rotational axis of an aircraft [14]	17
4.5	Visualisation of the effect the walls have on the flow [Own work]	19
4.6	Effect of model blockage on the velocity and static pressure [15]	19
4.7	Airfoil with wake generated. [6]	20
4.8	Effect of wake on the velocity and static pressure [15]	20
4.9	Uncorrected and corrected polars for the NACA 64 ₂ A – 015 airfoil tested in the wind tunnel at Re ≈ 860 000.	21
4.10	A better visualisation of the differences between the two corrected and uncorrected polars	21
5.1	C_p vs x/c graphs	23
5.2	Pressure lines on the airfoil for a positive angle of attack [12]	24
5.3	C_l vs α polar for the NACA64 ₂ A015 Airfoil	25
5.4	Temperature heatmaps at AoA -3°, 0°and 4°	26
5.5	Temperature heatmaps at AoA 5°, 6°and 7°	26
5.6	Tuft naming and the movement in larger amplitudes of tuft 1	27
5.7	Tuft agitation on the infinite wing	27
5.8	Heatmaps before and after the LSB burst	28
5.9	Tuft movement at 16 °AoA	28
5.10	Comparing heatmaps at the same angle of attack after reattachment	29
5.11	C_d vs α polar for the NACA64 ₂ A – 015 Airfoil	29
5.12	C_l vs C_d polar for the NACA64 _{2a} 015 Airfoil	30
5.13	$\frac{C_l}{C_d}$ vs α polar for the NACA64 _{2a} 015 Airfoil	31
5.14	C_m vs α polar for the NACA64 _{2a} 015 Airfoil	32
5.15	C_L vs α polar at V = 51.69 m/s	34
5.16	State of the flow at AoA of -1°	35

5.17	Temperature heatmaps at AoA 4°, 6°and 8°	36
5.18	Slope between two points on Figure 5.15 as a function of the angle of attack	36
5.19	Temperature heatmap for AoA of 9°	37
5.20	Typical stall behaviour for $(t/c)_{max} \geq 14\%$ wings from [12]	37
5.21	State of the tufts at an AoA of 15.5°for maximum lift coefficient	38
5.22	State of the tufts at an AoA of 18°	38
5.23	The drag coefficient, C_D , plotted against the Angle of Attack, α , at V=51.9 m/s	39
5.24	The lift coefficient C_L plotted against the drag coefficient C_D at V=51.9 m/s.	40
5.25	Experimental and simulation results of C_L/C_D ratio plotted for different angles of attack at V = 51.9 m/s	41
5.26	The moment coefficient, C_M , plotted against the Angle of Attack, α , at V = 51.9 m/s	42
5.27	Variation in Moment Coefficients, C_M due to Variation in x_{cg} location	43
5.28	XFLR5 Simulation of Lift for x_{cg} at Leading Edge	44
5.29	XFLR5 Simulation of Lift for x_{cg} at centroid	44
5.30	XFLR5 Simulation of Lift for x_{cg} at Quarter-Chord Point	44
5.31	Laminar flow sketch	46
5.32	Laminar separation bubble sketch	46
5.33	Velocity profile over airfoil in presence of an LSB	47
5.34	Stall sketch	47
5.35	Visualisation of the LSB on infrared images	48
5.36	Infrared picture hysteresis analysis	48
5.37	XFLR5 representation of tip vortices affecting the lift performance of three dimensional finite wings	49
5.38	Lift Distribution of a Finite Wing	49
5.39	Depiction of the Angle of Attack Reduction due to Tip Vortices, source: [24]	50
5.40	Lift Coefficient, C_L versus Angle of Attack, α for 2D and 3D Experiments	51
5.41	Drag Coefficient, C_D versus Angle of Attack, α for 2D and 3D Experiments	51
5.42	Moment Coefficient, C_M versus Angle of Attack, α for 2D and 3D Experiments	51
5.43	Lift to Drag Ratio, $\frac{C_L}{C_D}$ versus Angle of Attack, α for 2D and 3D Experiments	51
5.44	Lift Coefficient, C_M versus Drag Coefficient, C_D for 2D and 3D Experiments	52
5.45	Viscous vs inviscid simulation	53
5.46	Viscous vs inviscid simulation	54
5.47	Pressure distribution from XFLR5 at 0°AoA for $Re = 1\ 000\ 000$ and $Re = 500\ 000$	55
5.48	Infrared image of the airfoil at 0°AoA	55
5.49	Skin friction coefficient as a function of x/c	55

List of Tables

2.1	α increments for different flow conditions	6
3.1	Points used for the model in XFLR5	12
3.2	2D simulation parameters	14
3.3	3D simulation parameters	14
5.1	Skin friction coefficient	56

List of Abbreviations

AoA - *Angle of attack*

IBL - *Interactive boundary layer*

LE - *Leading edge*

LSB - *Laminar separation bubble*

LLT - *Lifting Line Theory* LTT - *Low Turbulence Tunnel*

Re - *Reynold's number*

TE - *Trailing edge*

TWT - *Thin wing theory*

VLM - *Vortex Lattice Method*

VPM - *Vortex Panel Method*

Introduction 1

Wind tunnels were first used in the XIX century and in some of the earliest experiments in aviation history. Since that moment, those tunnels have grown to become more reliable and diverse in types depending on their application. A wind tunnel experiment is always necessary to assess the performance of a wing profile, since all simulations include simplifications and assumptions making the numerical solution accurate only to some extent while the exact wing characteristics need to be assessed for safety of the design.

The aim of this report is to assess the characteristics of the NACA 64₂A – 015 airfoil in the case of both an infinite and a low-aspect ratio straight wing and to compare both cases. Those are determined through numerical and experimental methods of which the results are presented. The experimental data was obtained using the low speed wind tunnel from the TU Delft and are compared to the results of simulations performed in XFLR5. Python was used to process all the data. Among the most important part of the analysis is the determination of the lift, drag and pitching moment polars, the flow behaviour and the hysteresis of both the finite and infinite wing.

The structure of this report is as follows, chapter 2 provides a description of the test setup including the measurement devices used and the methodology followed during the practical. Then the simulation software and variables are described in chapter 3 while chapter 4 gives an overview of the experimental data acquisition methods used during the test and the corrections that had to be applied on the data. This is followed by chapter 5 presenting the results of both the numerical and experimental analysis, along some further carried studies. At last, chapter 6 consists of a conclusion on the results obtained and recommendations for further work on the subject.

Description of the Test Setup

2

In this chapter, a brief description of the test setup will be addressed and discussed. Section 2.1 explains how the wind tunnel operates and its characteristics. In Section 2.2, the 2D and 3D models are discussed. Next, in Section 2.3 the instruments and equipment used will be explained. Then, in Section 2.4 the variable in the experiment are presented and explained. Finally, in Section 2.5 the method used to perform the experiment is explained

2.1 Low Speed Wind Tunnel

The LTT is an atmospheric tunnel of the closed-throat single-return type. The fan and engines are mounted on ground level whereas the settling chamber and test section are on the second floor. Due to a large contraction ratio of 17.8, the free-stream turbulence level in the test section varies very little [1]. The schematic drawing of the LTT tunnel can be seen in Figure 2.2.

The wind tunnel experiment was performed in the test section located on the second floor of the building, section 9 shown on the schematic below and presented on Figure 2.1. The operation of the tunnel is as follows: first a fan brings the air into motion, then the corner vanes guides the flow around the corners smoothly. The flow then passes through anti-turbulence screens and finally converges to the desired velocity.



Figure 2.1: Test section room, located on the second floor of the building

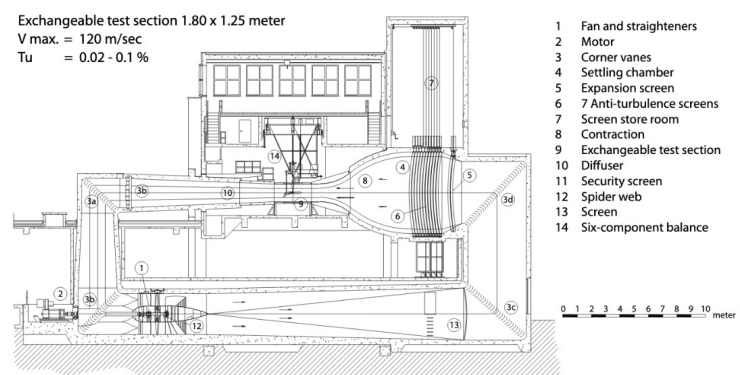


Figure 2.2: Schematic of the wind tunnel used for the experiment

2.2 Airfoil and Wing Models

Both the airfoil and wing model consists of a straight low aspect ratio wing attached to a turning table to allow for changes in angle of attack. The model setup and turning table can be seen on Figure 2.3 and 2.5. In subsection 2.2.1 the 2D model will be explained and, later on subsection 2.2.2, the 3D model will be explained.

2.2.1 2D model

The 2D test model contains several pressure taps along the chord direction of the airfoil. In order to simulate the physical model as a 2D airfoil section the wing was placed between two flat surfaces, namely the tunnel wall and a table present at the tip of the wing. This is done to avoid wing tip vortices which otherwise would induce a downwash and, consequently, a different pressure distribution along the span. This can be seen in Figure 2.3. A drawing of the model is also provided below (Figure 2.4).



Figure 2.3: 2D setup

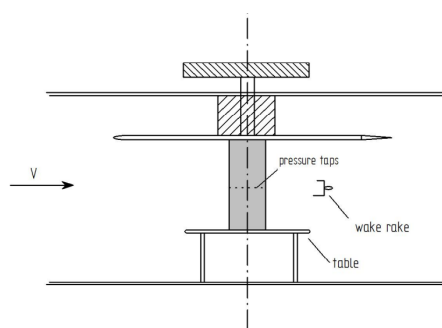


Figure 2.4: 2D setup drawing

2.2.2 3D model

The 3D setup is very similar to the 2D setup. The difference being the removal of one wall from the wing and adding a removable tip (Figure 2.8). Adding a wingtip introduces 3D effects such as wingtip vortices. The airfoil with the introduced wingtip can be seen in Figure 2.5. These 3D effects change the pressure distribution along the spanwise direction and thus, for the 3D experiment, an external 6-component force balance system is used to obtain the data.



Figure 2.5: 3D setup including wake rake

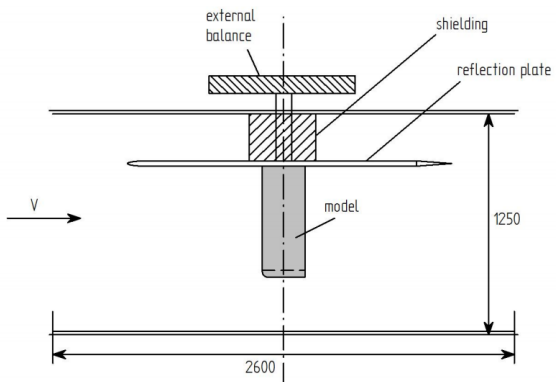


Figure 2.6: 3D setup drawing

A drawing with the model dimension is provided on Figure 2.7. Note that, the dimension for the 2D model can also be derived from this Figure. From the values present below, calculating the Aspect Ratio of the 3D model is also possible by making use of Equation 2.1, yielding a value of $A = 5.3$. This will later be used for Equation 5.1

$$A = \frac{b}{c} \quad (2.1)$$

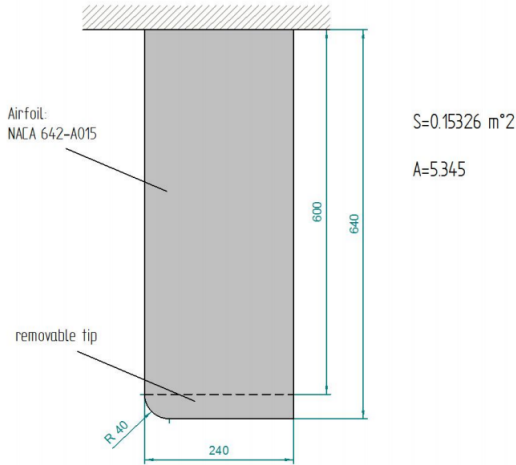


Figure 2.7: Low Aspect Ratio Wing Model



Figure 2.8: Close view of wingtip

2.3 Measurement Techniques

The model and turning table are attached to an external 6-component balance to measure lift, drag and pitching moment for the 3D wing model, as previously explained on subsection 2.2.2. The balance can be seen on Figure 2.9. A schematic drawing of the balance is also provided in Figure 2.11.

Apart from the 6-component balance, the wind tunnel is also equipped with 192 ports electronic pressure scanner system (Figure 2.10), wake rake (Figure 2.5) and hot wire anemometry. For the purpose of flow visualization, an infra-red camera system is available that allows to visualize the boundary layer transition due to difference in temperature along the chord wise direction. Additionally, tufts were used for flow visualization. The tufts, stuck on the model surface, orientation with respect to the freestream flow would indicate flow features like separation, reattachment and recirculation region [2].



Figure 2.9: 6-component balance



Figure 2.10: Ports electronic pressure scanner

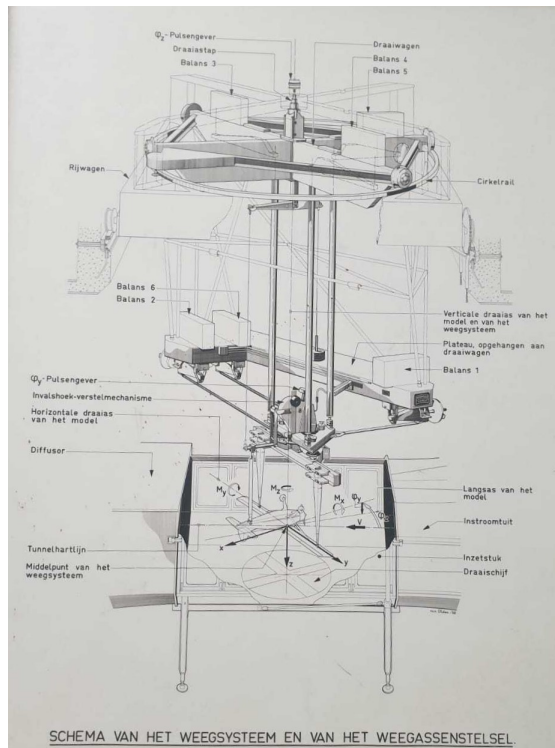


Figure 2.11: Schematic of the 6-component balance

2.4 Variables

A distinction is made in this subsection between the different variable types present in the experiment. Namely, the independent, dependent and control variables.

The independent variable is the cause and its value is independent, as the name suggests, of other variables in the study [3]. For this experiment, the independent variable is the angle of attack, α . The dependent variable is the effect and its value depends on changes of the independent variable. This would be the pressure data over the airfoil and important coefficients such as the drag coefficient. As it can be expected, different values of the dependent variable will arise for different values of the independent variable, namely α .

The velocity in the test section was roughly kept constant and verified by a pitot tube located in front of the model. The tunnel rpm was changed accordingly to ensure a velocity reading of 52 m/s during all measurements. In reality, small variations would arise between different measurement but all readings were within a $\pm 1 \text{ ms}^{-1}$ margin from the control value of 52 ms^{-1} .

It should be noted that the velocity measured ahead of the model, in the beginning of the test section, is not reliable as a measurement of the wind tunnel speed. This is due to the model in the tunnel causing blockage, nonetheless, this can be used as a controlling measure. The true velocity is found by using the pressure difference in the settling chamber and the contraction area in combination with a calibration curve. The pressure in the settling chamber is measured by a total pressure tube whereas the pressure in the contraction is obtained by a static pressure tube.

2.5 Methodology

Different measurements were recorded for different values of angle of attack. For this, α was varied in small incremental steps depending on the flow condition. The different steps are illustrated below on Table 2.1. As shown on the Table, the first value of the angle of attack is -3° and that gradually increases with incremental steps of 1° up to 0° . This was chosen to verify the zero lift AoA at 0° angle of attack, due to the symmetrical nature of the airfoil geometry.

Table 2.1: α increments for different flow conditions

From	To	Increment
-3°	0°	$+1^\circ$
0°	LSB	$+0.5^\circ$
LSB	$C_{l_{max}}$	$+0.5^\circ$
$C_{l_{max}}$	α_s	$+0.5^\circ$
α_s	$\alpha_s + 2^\circ$	$+0.5^\circ$
$\alpha_s + 2^\circ$	reconnection	-0.5°

For each angle of attack, a set of operations would be followed to ensure a consistent data collection. These operations would follow a sequence of events as follow:

- Change angle of attack
- Check wake rake positioning
- Take video of the tufts
- Take thermal pictures
- Take measurements

For each α several useful parameters would be recorded including but not limited to C_l , C_d , C_m and C_p . Moreover, 6 thermal pictures would be taken for each AoA and the pictures would be averaged to avoid noise. This enables the observation of the boundary layer transition for different angles of attack, seen that temperature is lower for turbulent flows. Higher temperatures implies a laminar flow since the boundary layer absorbs less heat, yielding a difference in temperature between the laminar and turbulent region.

For the 2D wing test, the pressure ports located along the chord-wise direction is used to determine the C_l coefficients for different angle of attacks. As the pressure distribution along the span-wise direction is constant for a 2D configuration, the data from the pressure ports is used to obtain C_l and C_m by integrating C_n and C_t . This process will be will be further explained in chapter 4. For the C_d , the wake rake present after the model measures the momentum deficit which can then be used to obtained the drag coefficient.

For the 3D test, the process is quite similar. For the C_D , the same methodology is used by making use of the momentum deficit determined by the wake rake. For the C_L and C_M , however, it would not be appropriate to determine these coefficient by making use of the pressure data seen that the pressure measurements are taken at a specific position along the span. Due to downwash, the pressure measurement along the chord would vary along the span. So, for the C_L and C_M for the 3D model, a 6-component balance is used instead to obtain those coefficients.

Simulation Considerations

3

In addition to the experiment, a computer simulation was performed to assess the accuracy of the airfoil and wing flow analysis software. The software used in this case is XFLR5. This section serves to give background information on this program, elaborate on the assumptions and flaws used for the development of the code and explaining the procedure required to obtain results from the software. First, section 3.1 presents the theory on which XFLR5 is based to perform the calculations, then section 3.2 gives an overview of the limitations of the software. Finally, section 3.3 shows the parameters and models used for the simulations.

3.1 Background Information

The program used to obtain airfoil and wing characteristics is XFLR5. This software can be used to analyse airfoils and wings at low Reynolds number. Part of the software is built on top of XFOIL [4], a program used solely for the analysis of airfoils. To obtain the finite and infinite wing characteristics XFLR5 numerically solves the Laplace's equation under certain boundary conditions. This method varies depending on whether an airfoil or wing is analysed as the latter must also incorporate three-dimensional effects. The method used for two-dimensional flows is based on the Vortex Panel Method, abbreviated as VPM, and will be discussed in subsection 3.1.1. For three-dimensional flows, the analysis is based on the Lifting-Line Theory, Vortex Lattice Method, abbreviated as VLM, and the 3D Panel Method (see subsection 3.1.2). Those are discussed below.

3.1.1 Vortex Panel Method

Laplace's equation holds for an inviscid, irrotational, incompressible flow, meaning that this equation must be satisfied everywhere in the flow field. In addition to this requirement, the imposed boundary conditions must be satisfied along the surface of the airfoil as well. Mathematically, Laplace's equation is written in the form of Equation 3.1.

$$\Delta\phi = 0 \quad (3.1)$$

Equation 3.1 is a linear differential equation, therefore, any linear combination of solutions of the equation is a solution as well. This property can be used to mimic the effect of an airfoil on a flow field. First, an expression which satisfies Laplace's equation must be found from a linear combination of elementary solutions of Equation 3.1. This comes down to placing many elementary vortices on the airfoil surface. This is done by discretising the airfoil in multiple panels on which the elementary vortices are placed (hence the name vortex panel method). The location at which the elementary vortex is applied is called the control point. Secondly, the flow-tangency boundary condition must be applied at each control point. This comes down to Equation 3.2.

$$\vec{V}_i \cdot \vec{n}_i = 0 \quad (3.2)$$

Meaning that the velocity vector at control point i must be normal to the surface vector of panel i (recall that the latter is normal to the panel itself). The flow-tangency condition can also be interpreted in the following way.

$$V_{\infty,n} + w_{induced} = \frac{dz}{dz} \quad (3.3)$$

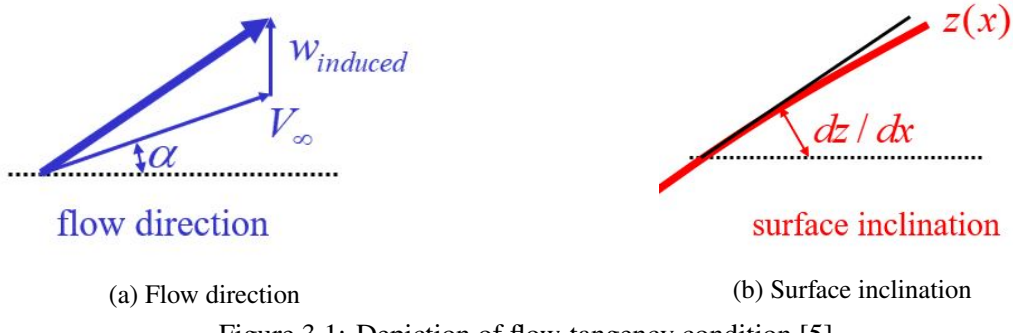


Figure 3.1: Depiction of flow-tangency condition [5]

This essentially comes down to the same reasoning: the normal freestream velocity component and the induced velocity from the vortices should equal the slope of the airfoil surface. This is depicted in Figure 3.1.

Finally, the Kutta condition stating that the flow at the trailing edge must leave the surface smoothly [6] can be applied. This results in a system of N equations with boundary conditions and N unknowns being the vortex strength of the elementary vortices that can be solved. Having solved this system of equations a flow field is obtained incorporating the effect of an airfoil. The pressure coefficient is given by Equation 3.4.

$$C_p = \frac{p - p_\infty}{\frac{1}{2} \rho v^2} = 1 - \left(\frac{V}{V_\infty} \right)^2 \quad (3.4)$$

Since the vortex strength at each control point was solved for in the first place, the velocity at a certain control point can be obtained easily. From the pressure coefficient distribution many relevant airfoil parameters can be derived.

3.1.2 Lifting-Line Theory, Vortex Lattice Method and 3D Panel Method

Three-dimensional effects must be taken into account when dealing with wings rather than airfoils. Helmholtz's theorems are used for this method and are given in the following:

1. The vortex strength is constant along its length
2. A vortex cannot end abruptly and must therefore extend to infinity or form a closed path

Those imply in turn that for three-dimensional flows the vortex along the span must be deflected backwards at the tips of the wing thereby creating tip vortices. The shape of this vortex closely resembles a horseshoe vortex. This so-called horseshoe vortex is illustrated in Figure 3.2.

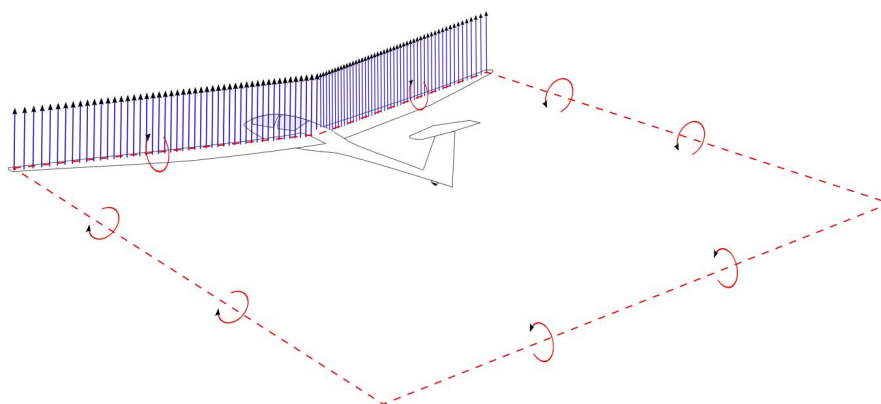


Figure 3.2: A horseshoe vortex [7]

In two-dimensional flows, the vortex extends to infinity and consequently no such tip vortices exist. XFLR5 uses three methods to address three-dimensional effects: the lifting-line theory, vortex lattice method and the 3D panel method.

The lifting-line theory works by using one horseshoe vortex filament which gradually sheds its strength in the wake along the wing. The vortex lattice method works similarly to the VPM as the wing must be discretised into panels first: a horseshoe vortex or ring vortex is placed on each panel and the flow-tangency condition is applied at each panel. This results in many thin lifting surfaces. The 3D panel method works similarly. However, instead of placing an elementary vortex at each panel, an elementary doublet and a elementary source/sink is placed. This results in many thick lifting surfaces. The exact workings of these methods is not discussed in greater detail as this is considered out of the scope of the present report.

3.2 Limitations and Shortcoming of the Software

XFLR5 is in no way a depiction of reality, in fact [8] states:

"The resulting software is not intended as a professional product, and thus it does not offer any guarantees of robustness, accuracy or product support. It is merely a personal use application, developed as a hobby, and provided under GPL rules for use by all."

According to [9], XFLR5 has the following limitations:

- Viscosity
- Panel Modeling
- Flat wake

In this section, each of these, will be discussed. Furthermore, a short conclusion will be given on why the use of software, such as XFLR5, is still necessary regardless of its shortcomings.

Viscosity

There are two issues in XFLR5 that arise from viscosity:

1. Lack of a viscous interactive boundary layer (IBL) loop for VLM and panel methods excluding Lifting Line Theory (LLT)
2. The viscous drag estimation for the 3D panel method and VLM method.

The IBL is a coupling method between the potential flow and viscous flow on the surfaces. A boundary layer changes the geometry over surfaces and thus impacts the inviscid potential flow on the surface. To get these effects in a program such as XFLR5 a IBL loop should be included, however XFLR5 does not have such a loop.

Due to this, XFLR5 has some limitations concerning the VLM and Panel methods. Figure 3.3, shows different $C_L - \alpha$ lines for the different methods at the same Reynolds number. Here, it is clearly visible that Xfoil and the LLT both have the viscosity effects included due to the line not being linear, but looking at the panel method, the line is a function of the angle of attack. That is, as mentioned above, only the inviscid case is inspected due to the lack of a viscous IBL loop.

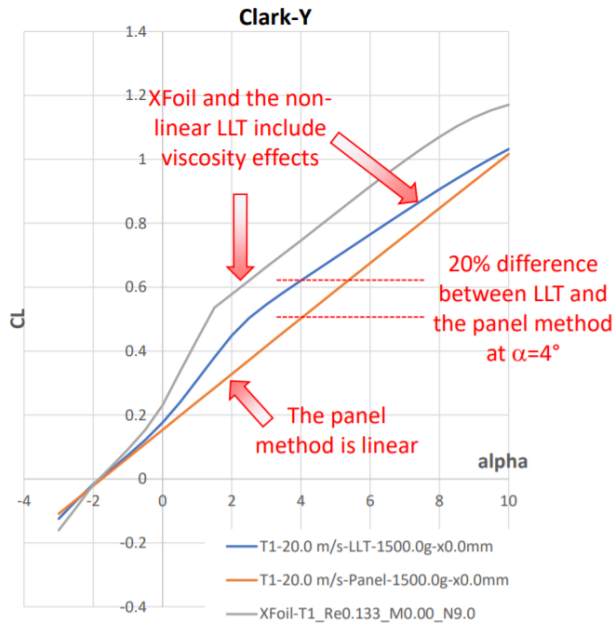


Figure 3.3: Xfoil and LLT with IBL loop vs. Panel method without IBL loop [9]

It also causes for quite significant differences in the predicted C_L for low Reynolds number as can be seen. However, because the potential flow method is only valid in conditions where limited flow separation takes place, this method does give good predictions if the analysis is limited to these conditions. Those are listed in the following:

- High Reynolds number
- Low angles of attack
- Low flap deflections

Next to the above mentioned shortcoming of XFLR5 the viscous drag estimation for VLM and the 3D panel method is also a problem. The viscous drag estimation for these is interpolated from the 2D case of local wing lift. This causes the issue that the viscous drag estimation can merely be used as an order of magnitude indication and the transition location from laminar to turbulent flow is not fully reliable. Furthermore, the biggest impact it has is that the total drag is underestimated meaning a *substantial* overestimation in the glide ratio.

Panelling Method

XFLR5 encounters some problems when it comes to the modelling of the wing with panels. The issue relevant for the analysis that is being done in this report is:

- Flat quad panel (VLM and panel method excluding LLT)

The 3D panel method requires two things when the wing is being modeled. These are that all four point of the quad panel need to be in the same plane and that the volumes are entirely enclosed by surface elements. The issue here is that general surfaces can not be decomposed in flat quad panels, see Figure 3.4.

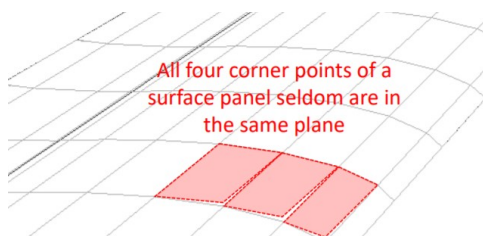


Figure 3.4: Example to represent that flat quad panels do not cover the surface entirely [9].

XFLR5 does not take this into account meaning that the 3D surface is enclosed in warped panels, but the flat panel method is used for analysis. This results in numerical errors which increase with the warping or twisting of the panels. Even though it is expected that the magnitude of the error is low, this is not a certainty as the evaluation of this problem is difficult.

Flat Wake

The final limitation/shortcoming XFLR5 has is that it has a flat wake. In XFLR5 the wake is modeled as flat panels or vortex lines behind the trailing edge and acts as an extension. In reality a wake takes the shape of the streamlines and thus it would be logical for the program to implement that the wake panels take this shape. This would be called a wake roll up.

Nevertheless, due to the fact that it would make the software less user friendly, especially as the wake would have to be tuned on a case-by-case basis, XFLR5 has decided to disable this. This does bring some quite big impacts to the accuracy of the numerical solutions found. The vortex and doublet strength are overestimated, as well as the estimation of the lift. For the lift and induced drag the error can be in the range of 1% to 10% for a standalone wing, which is exactly what is being analysed in this report. When modelling a complete aircraft the panels of the main wing may intersect with that of the elevator and fin panels resulting in unwanted interaction.

Conclusion

Looking back at the opening statement of this section, it is clear that XFLR5 has quite a lot of shortcomings which limit the analysis that can be done with the program. This also the case for computer fluid dynamics (CFD) programs and other programs such as Xfoil, like Rfoil. Results against the experimental values show great variation between the two, see Figure 3.5. This shows quite a difference in the predicted lift coefficient and stall angle by the CFD, Xfoil, Rfoil and the experimental values. These deviations are there because these programs all have their own shortcomings and modelling the "reality" perfectly is unfortunately not possible.

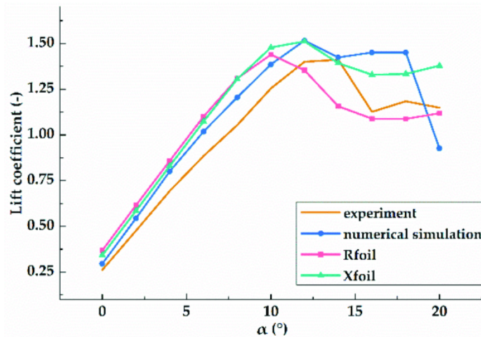


Figure 3.5: Comparison between the numerical results, Rfoil, Xfoil and experimental data for the DU 91-W2-250 airfoil

Nevertheless, doing experiments in a wind tunnel is expensive and it has a long waiting list. This means that programs such as XFLR5 are needed in order to get a feel on the orders of magnitude, the trend and to understand the sensitivity of the parameters [9].

3.3 Details on the Analysis

This section deals with the parameters and assumptions made to carry the analysis. subsection 3.3.1 presents the model used to perform the 3D wing analysis and subsection 3.3.2 gives an overview of the various options used.

3.3.1 Model of the Wing on XFLR5

The process for modelling the wing in XFLR5 is fairly straightforward. In the two dimensional airfoil analysis, the airfoil profile was already defined. As a result, this airfoil profile simply needs to be extended over the span

of the wing (the airfoil shape remains conserved everywhere along the wing). This is done by first defining the wing span of the three dimensional wing (which is known to be 640 mm), and then defining the chord length of the wing at specific locations of interest. In this case, the three dimensional wing which is to be considered has the same chord length (240 mm) over the whole span of the wing until the wing tip is reached.

The modelling of the wing tip is slightly more complicated, as it consists of a rounded shape, resulting in a shorter chord length at the very end of the wing tip. As described in the reader, the contour of the rounding of the wing tip is described by an arc with a radius of 40 mm. As a result, the chord length before the rounding is 240mm, and the chord length after the rounding is 200mm. At locations during the rounding, the chord length may therefore be defined as (see Figure 3.6):

$$c = 240 \cdot \cos \theta \quad (3.5)$$

This formula was used to define points of the rounding in XFLR5. Note that the software connects defined points using straight lines. Therefore, a sufficient number of points in the rounding curve must be defined such that the curve may be approximated as a series of straight lines. This was found to be approximately 6 points.

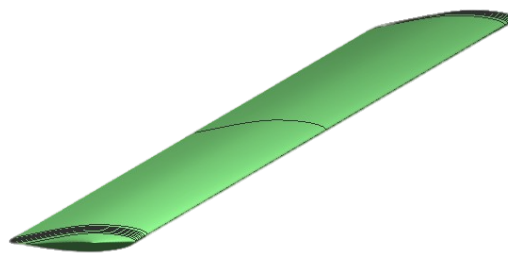
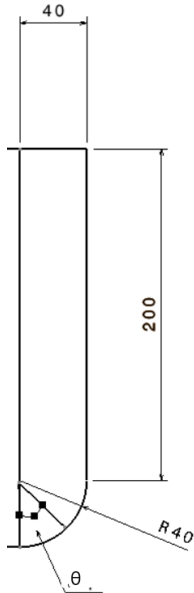


Figure 3.7: Wing Model made on XFLR5

Figure 3.6: Diagram Depicting Wing Tip Rounding

Table 3.1 outlines the data points used to outline the geometry of the wing model on XFLR5.

Table 3.1: Points used for the model in XFLR5

Span-Wise Position [mm]	Chord Length [mm]
0.000	240.000
600.000	240.000
610.000	238.637
615.000	237.090
620.000	234.641
625.000	231.520
630.000	226.240
635.000	219.392
640.000	200.000

3.3.2 Parameters used for the Simulation

In this section, the parameters used in the XFLR5 simulations are mentioned and the values that were chosen for these parameters are explained. The red line in the provided rationale is that the simulation conditions must be as close to the test conditions as possible.

2D Airfoil Analysis

For the 2D analysis, the following parameters could be defined:

- Reynolds number
- Mach number
- N_{crit}

The Reynolds number was chosen to be 860000, as this is the approximate value of the Reynolds number during the test. The Mach number was chosen to be 0. The reason why zero was chosen instead of the actual Mach number of the flow during the test has to do with compressibility effects being negligible. Indeed, although the true Mach number really never was zero due to the non-zero flow velocity, it is a fair assumption as $M < 0.3$ at all times. Additionally, the velocity at which the 2D test was performed is 51.7 ms^{-1} . At standard ISA sea level conditions, this converts to a Mach number of 0.15. Using the Prandtl-Glauert correction in Equation 3.6, it is possible to see that the actual lift coefficient is only about 1% greater than the lift coefficient at a Mach number of 0. The same applies for the drag and moment coefficients. This difference is so small, that the effects of compressibility can be assumed to be negligible.

$$C_l = \frac{C_{l_0}}{\sqrt{1 - M^2}} \quad (3.6)$$

The value of N_{crit} was chosen to be 9. The N_{crit} value is related to laminar-turbulent transition and it arises from the e^N method for transition prediction, which XFLR5 uses. A description regarding this method is deemed outside of the scope of this report. Detailed information can be found in [10]. In this article, it is mentioned that the N_{crit} value of 9 is widely used value in airfoil analysis, which is why it was chosen for the performed simulations. All the mentioned values can also be seen in Table 3.2.

3D Wing Analysis

For the 3D analysis the following parameters could be defined:

- Velocity
- Density
- Kinematic viscosity
- Analysis method

The velocity, density and kinematic viscosity were all chosen to resemble the test conditions as closely as possible. Therefore, the velocity was chosen to be 51.7 ms^{-1} , the density was chosen to be the ISA sea level density of 1.225 kgm^{-3} , and the kinematic viscosity was chosen to be the ISA sea level value of $1.461 \cdot 10^{-5} \text{ m}^2\text{s}^{-1}$.

The analysis method was chosen to be VLM2, or the Ring Vortex method. This is a VLM method, or vortex lattice method. A brief description of how this method works is given in subsection 3.1.2. Vortex lattice methods

are different from other panel methods in the fact that a VLM is 'lift-oriented'. This makes it more suitable to find the global lift coefficient, pressure and lift distributions, induced drag and information regarding stability [11]. As this is the information required, the VLM was chosen over other panel methods. In Table 3.2 and Table 3.3, the values used for both the 2D and 3D XFLR5 simulations are compiled.

Table 3.2: 2D simulation parameters

Parameter	Value	Unit
Re	860000	[\cdot]
M	0	[\cdot]
N_{crit}	9	[\cdot]

Table 3.3: 3D simulation parameters

Parameter	Value	Unit
V	51.7	ms^{-1}
ρ	1.225	kgm^{-3}
ν	$1.461 \cdot 10^{-5}$	m^2s^{-1}
Analysis method	VLM2	-

Data Acquisition and Correction 4

The experiment took place in a wind tunnel. To get data from the experiment measurement equipment was used and from those measurements with the help of calculations the aerodynamic coefficients for the airfoil and wing were determined (section 4.1 and section 4.2). During the wind tunnel experiment there are several hindrances that interfere with freestream flow around the wing and airfoil, to correct for these several wall corrections mentioned in section 4.4 are applied to the obtained data in order to obtain more realistic values.

4.1 Pressures Leading to 2D Coefficients

The aerodynamic forces acting on the airfoil in the 2D case are presented in Figure 4.1, for these forces the following 2D aerodynamic coefficients; lift coefficient (C_l), drag coefficient (C_d) and the pitching moment coefficient (C_m) are determined in the wind tunnel. These are derived from the pressure distributions that act on the airfoil. The pressure is measured by suction cups along the airfoil and gives the (static) pressure over the upper and lower part of the airfoil. Because it is a 2D airfoil, the pressure along the span at a certain chord position should be the same. By using Equation 4.1 [6], these pressures get converted into pressure coefficients.

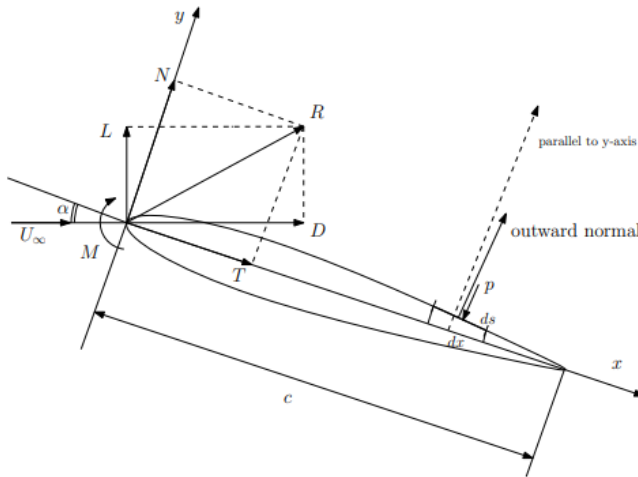


Figure 4.1: The forces acting on an airfoil [1]

$$C_p = \frac{p - p_\infty}{\frac{1}{2} \rho V_\infty^2} = \frac{p - p_\infty}{q_\infty} \quad (4.1)$$

Here p is the local static pressure, p_∞ is the freestream static pressure, ρ the density, V_∞ is the freestream velocity and q_∞ is the freestream dynamic pressure. In Figure 4.2 an example of a pressure coefficient distribution along the chord is presented.

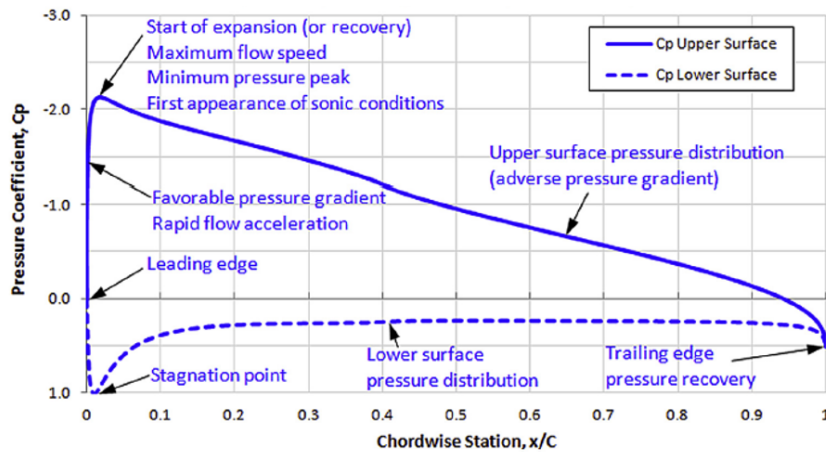


Figure 4.2: Example of a pressure coefficient graph with the different parts indicated [12]

With the pressure coefficient distribution known using Equations 4.3-4.10, the 2D aerodynamic coefficients can be calculated. The first that will be discussed is the normal force coefficient. The normal force coefficient can be obtained by integrating over the pressure distribution. The equation for the normal coefficient in terms of difference between the pressure on the upper side and lower side of the airfoil is given by Equation 4.2 [1]. The form which is rewritten with Equation 4.1 to obtain the normal coefficient as a function of the pressure coefficients is given by Equation 4.3 [1].

$$C_n = \frac{N}{\frac{1}{2}\rho U_\infty^2 c} = - \int_0^1 \frac{p_u - p_l}{\frac{1}{2}\rho U_\infty^2} d\frac{x}{c} \quad (4.2)$$

$$C_n = \int_0^1 (C_{p_l} - C_{p_u}) d\frac{x}{c} \quad (4.3)$$

In these equations the subscript l is used to indicate the lower surface of the airfoil and the subscript u for the upper surface of the airfoil.

The pitching moment coefficient is obtained in a similar way to that of the normal coefficient. Equation 4.4 [1] shows the general equations for the pitching moment coefficient for a 2D airfoil and Equation 4.5 [1] displays the equation for the moment coefficient at the quarter chord point.

$$C_m = \frac{M}{q_\infty c^2} = \int_0^1 \frac{(p_u - p_l)x}{q_\infty c^2} dx = \int_0^1 (C_{p_u} - C_{p_l}) \frac{x}{c} d\frac{x}{c} \quad (4.4)$$

$$C_{m_{0.25c}} = C_{m_e} + 0.25C_n \quad (4.5)$$

The drag coefficient calculation is a bit more complicated. Because the wake rake is installed closely to the airfoil model, the static pressure (p_1) behind the airfoil is not equal to the static freestream pressure (p_∞), see Figure 4.3.

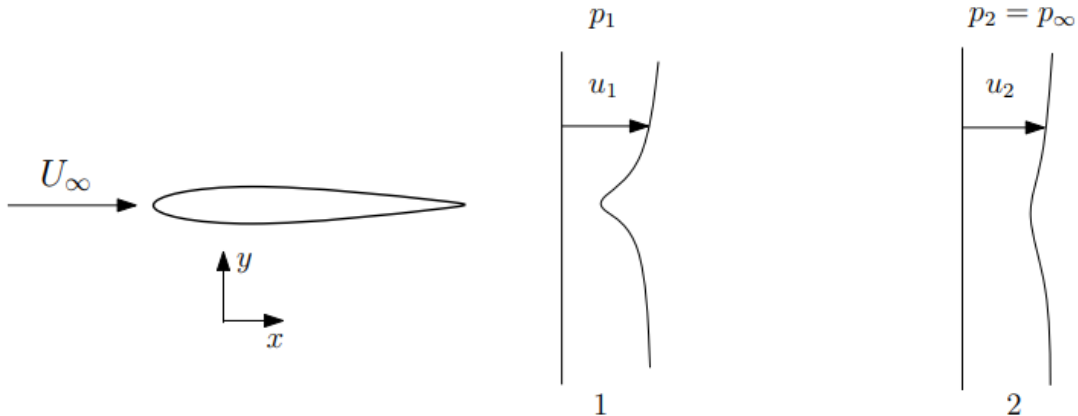


Figure 4.3: Drag analysis for a 2D-airfoil [1]

The reason behind this is explained later on in subsection 4.4.3, for now the Law of continuity (Equation 4.6 [6]) and the fact that total pressure is constant along a streamline ($p_{t_1} = p_{t_2}$), has to be applied to the drag coefficient equation which assumes that $p_2 = p_\infty$ (Equation 4.7 [1]). That equation than turns it into the drag coefficient equation which account for the fact that $p_1 \neq p_\infty$ (Equation 4.8 [1]).

$$\rho u_1 dy_1 = \rho u_2 dy_2 \quad (4.6)$$

$$C_d = 2 \int \sqrt{C_{p_t}} \left(1 - \sqrt{C_{p_t}} \right) d \frac{y_2}{c} \quad (4.7)$$

$$C_d = 2 \int \sqrt{C_{p_t} - C_{p_s}} \left[1 - \sqrt{C_{p_t}} \right] d \frac{y_1}{c} \quad (4.8)$$

The final coefficient that has to be determined is the lift coefficient. The equation for the lift coefficient (Equation 4.10 [13]) is derived by using the relation between lift, drag, normal force and tangential force relations (Equation 4.9) [13]. These equations are derived from Figure 4.1.

$$\begin{cases} C_l = C_n \cos \alpha - C_t \sin \alpha \\ C_d = C_t \cos \alpha + C_n \sin \alpha \end{cases} \quad (4.9)$$

$$C_l = C_n \left(\cos \alpha + \frac{(\sin \alpha)^2}{\cos \alpha} \right) - C_d \tan \alpha \quad (4.10)$$

4.2 Balance Data Leading to 3D Coefficients

In the wind tunnel setup for the 3D wing model a balance was used to measure the forces and moments acting on it; Lift (L), Drag (D) and the moment around one of the axis indicated in Figure 4.4 (M). In this section an explanation will be given on how the 3D coefficients; lift coefficient (C_L), drag coefficient (C_D) and the moment coefficient (C_M) were obtained from the data measured by the balance.

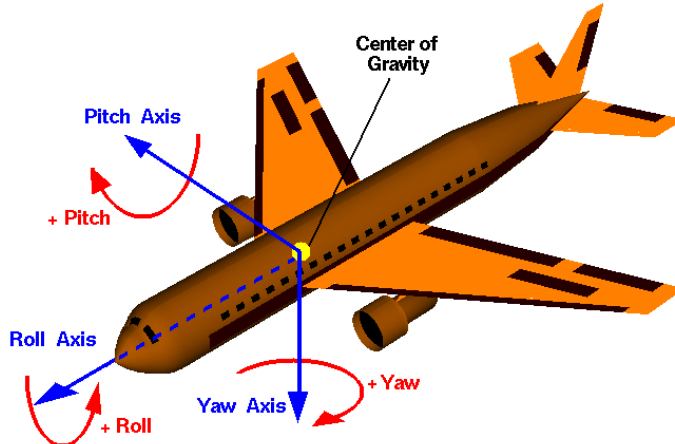


Figure 4.4: The rotational axis of an aircraft [14]

The first coefficient that will be discussed is the lift coefficient. This coefficient can be calculated with the help of Equation 4.11 [6].

$$C_L = \frac{L}{\frac{1}{2} \rho V^2 S} = \frac{L}{q_\infty S} \quad (4.11)$$

The drag coefficient is calculated using Equation 4.12. This result can be validated as the drag coefficient exists out of two parts the induced drag coefficient (C_{D_i}) and the profile drag (C_{D_0}) (Equation 4.13). The profile drag can be obtained from the 2D analysis and the induced drag can be calculated using Equation 4.14. This should lead to approximately the same drag coefficients.

$$C_D = \frac{D}{\frac{1}{2}\rho V^2 S} = \frac{D}{q_\infty S} \quad (4.12)$$

$$C_D = C_{D_0} + C_{D_i} \quad (4.13)$$

$$C_{D_i} = \frac{C_L^2}{\pi A e} \quad (4.14)$$

The last coefficient calculation that will be discussed in the moment coefficient calculation. The moment is measured around 3-axis; pitch, roll and yaw, see Figure 4.4. For each of these axis a moment coefficient can be calculated using Equation 4.15.

$$C_M = \frac{M}{\frac{1}{2}\rho V^2 Sc} \quad (4.15)$$

4.3 Velocity and Dynamic Pressure

The wind tunnel has a six-bladed fan which is driven by a 525 kW DC motor. The rotations per minute (rpm) of the motor can be adjusted so that a certain speed can be set. In the wind tunnel at the position of the wake rake there are 2 rows of tubes. The bottom row measures the total pressure and the upper row measures the static pressure. The difference between these two pressures is the dynamic pressure, from Bernoulli's equation (see Equation 4.16), the total pressure is constant along a streamline and is equal to the summation of the static and dynamic pressure. In order to use this equation the following assumptions must be adhered:

- The viscous forces can be neglected; the flow is inviscid
- The flow is incompressible; the density does not change
- The flow is steady; the flow does not change with time

$$\frac{1}{2}\rho V_\infty^2 + p_0 = p_{tot} \quad (4.16)$$

4.4 Wall Corrections

In the wind tunnel there were 3 types of wall corrections, these are corrections due to:

- Lift interference
- Model blockage
- Wake blockage

Each of these will be discussed along their subsequent effects.

4.4.1 Lift Interference

The wind tunnel has solid walls that are impossible for the flow to penetrate. So, for viscous flow the friction that is present between the flow and the surface creates a boundary layer, with zero velocity at the surface. However, for inviscid flow this means that the flow must be tangent to the surface with a finite velocity [6]. This is called the wall tangency condition. The walls which limit the space of the incoming airflow are now acting as a streamline. This prevents the other ones from expanding. The result of this is that the other streamlines are now closer together compared to the freestream flow, see Figure 4.5 . The effect this has, is that the perceived camber of the airfoil is larger than it actually is. According to [12], an increase in camber means a subsequent increase in the perceived lift.

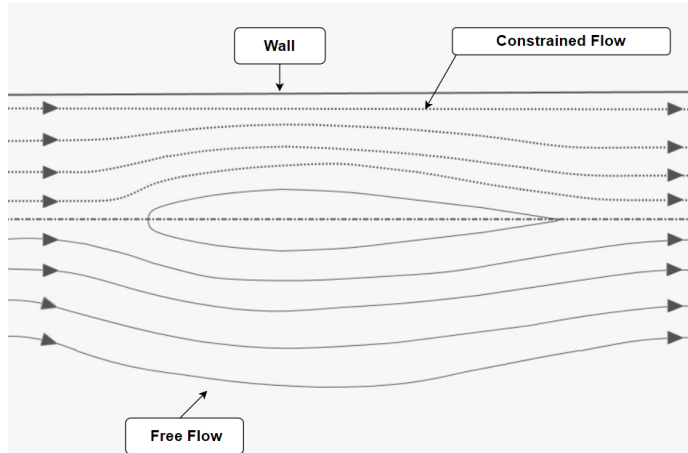


Figure 4.5: Visualisation of the effect the walls have on the flow [Own work]

4.4.2 Model Blockage

Model blockage is a form of solid blockage. In the test section, the area for the flow to pass is reduced and is no longer undisturbed and unrestricted. The continuity equation (Equation 4.17) can give more insight in this.

$$\frac{\partial}{\partial t} \iiint_V \rho dV + \iint_S \rho \mathbf{V} \cdot d\mathbf{S} = 0 \quad (4.17)$$

From Equation 4.17, the following relation for quasi-one-dimensional flow in a duct can be derived (Equation 4.18):

$$\rho_1 V_1 A_1 = \rho_2 V_2 A_2 \quad (4.18)$$

Because the flow is incompressible it means that the density stays constant. This means that if the area decreases, the velocity of the flow must increase around the airfoil model. The continuity equation then requires the flow to return to the undisturbed flow state. This increase in velocity around the airfoil increases the dynamic pressure and this increases the lift.

This effect can be seen from Figure 4.6. In the vicinity of the body where the velocity is increased this shows an increase in the ratio of freestream velocity vs local velocity. Also, according to bernoulli the total pressure stays constant so an increase in the dynamic pressure means a decrease in the static pressure leading to a decrease in the freestream static pressure vs local static pressure.

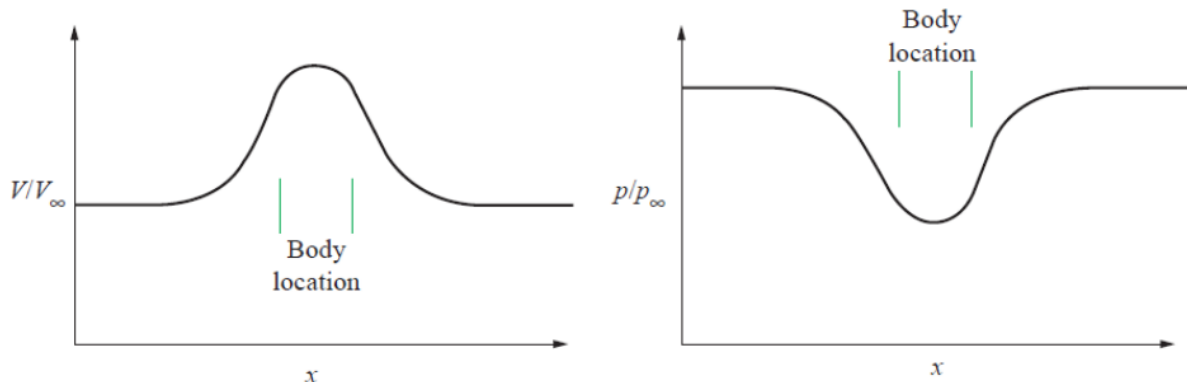


Figure 4.6: Effect of model blockage on the velocity and static pressure [15]

4.4.3 Wake Blockage

Due to flow separating from the surface of the airfoil a wake is caused, see Figure 4.7. This flow is a low energy recirculating flow, this means that the velocity at that point is lower than the freestream velocity. However, the continuity equation states that constant mass flow is needed and to achieve this the velocity behind and over the wake has to have a higher velocity than inside the wake. Thus, the wake blockage causes a velocity increase over and behind the airfoil. As mentioned in subsection 4.4.2, an increase in velocity means a decrease in the static pressure. This is made visual again in Figure 4.8

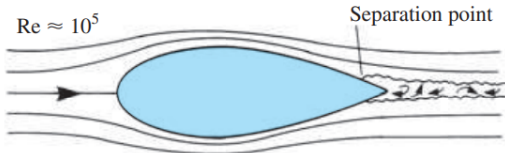


Figure 4.7: Airfoil with wake generated. [6]

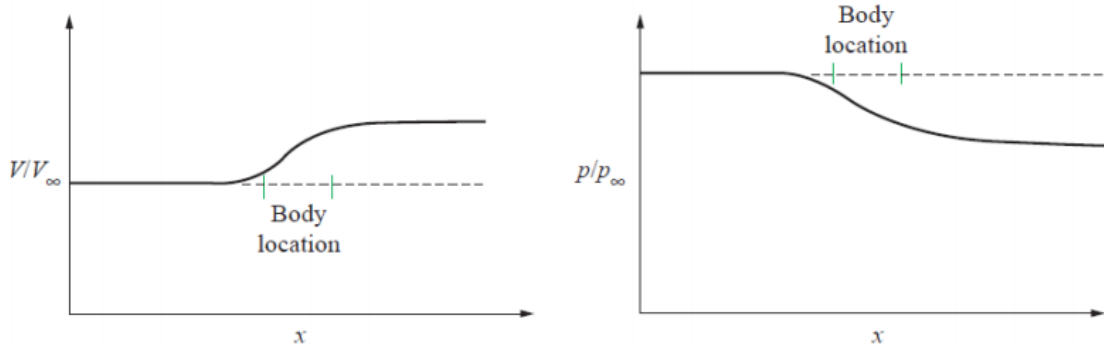


Figure 4.8: Effect of wake on the velocity and static pressure [15]

4.4.4 Influence of the Wall Corrections on the Data

From the subsection 4.4.1 to subsection 4.4.3, it became clear that a correction has to be applied to the data in order to obtain more realistic values. The recurring theme through all these sections was that because the speed increases, the dynamic pressure increases and thus the static pressure decreases. Thus, the logical correction to apply is a decrease in the dynamic pressure in order to obtain more realistic values.

In Figure 4.9, the various polars can be found which compare the corrected data against the uncorrected data. The graphs do not show much difference between them, but Figure 4.9a and Figure 4.9b do show a some more offset at higher angles of attacks. This makes sense as model blockage and wake blockage play a bigger part at higher angles of attack increasing the dynamic pressure. This will decrease the static pressure on the airfoil, decreasing the C_p (Equation 4.1), increasing the C_n (Equation 4.2) and increasing the lift and drag coefficient (Equation 4.10 and Equation 4.8). This means that these have to be corrected to a lower value and that is what happens.

For the moment coefficient again no difference can be seen in the polar, but from Equation 4.4 it is expected that if the dynamic pressure increases if the dynamic pressure gets corrected to a lower value. This is because the moment coefficient and dynamic pressure are inversely proportional to each other.

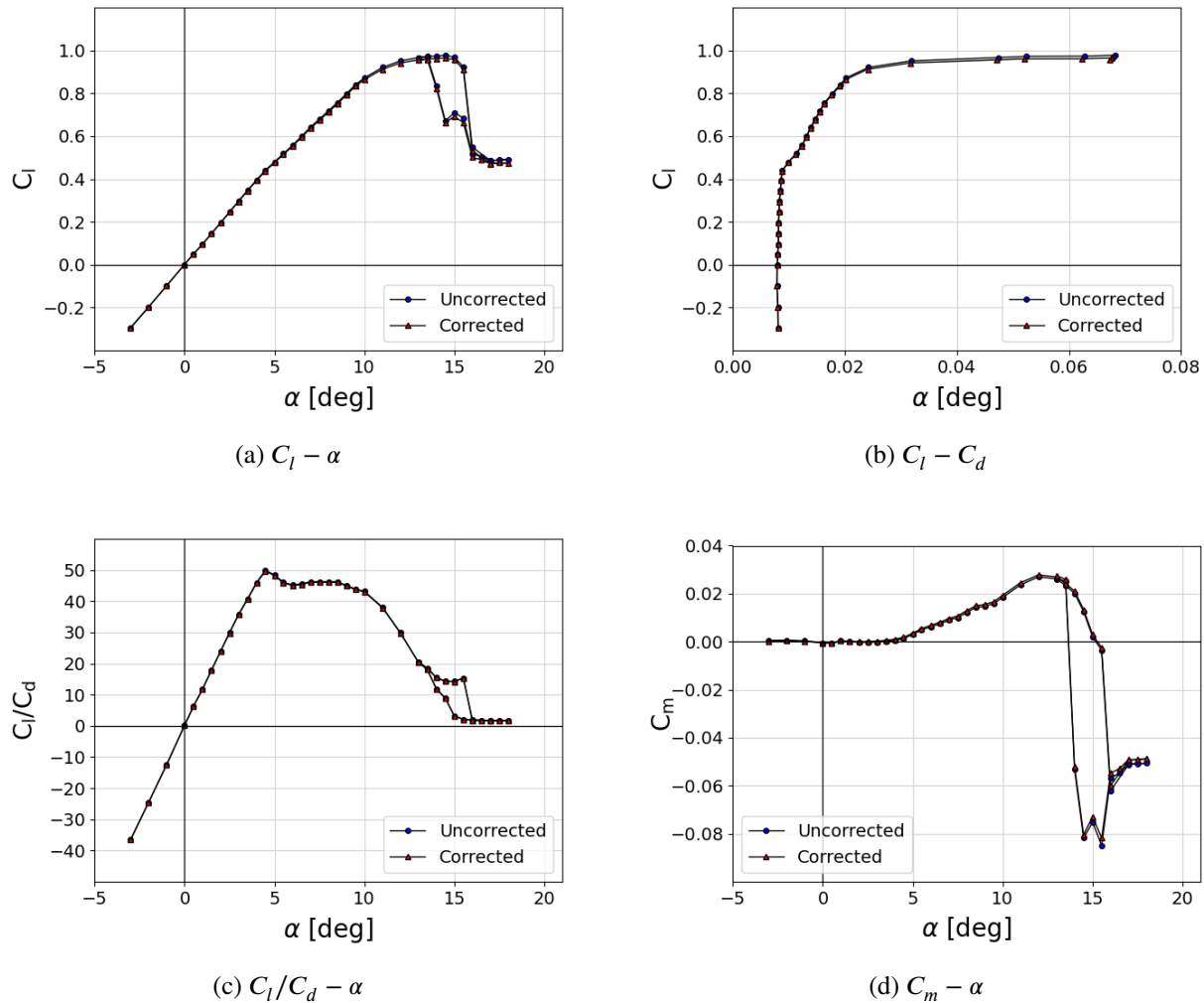
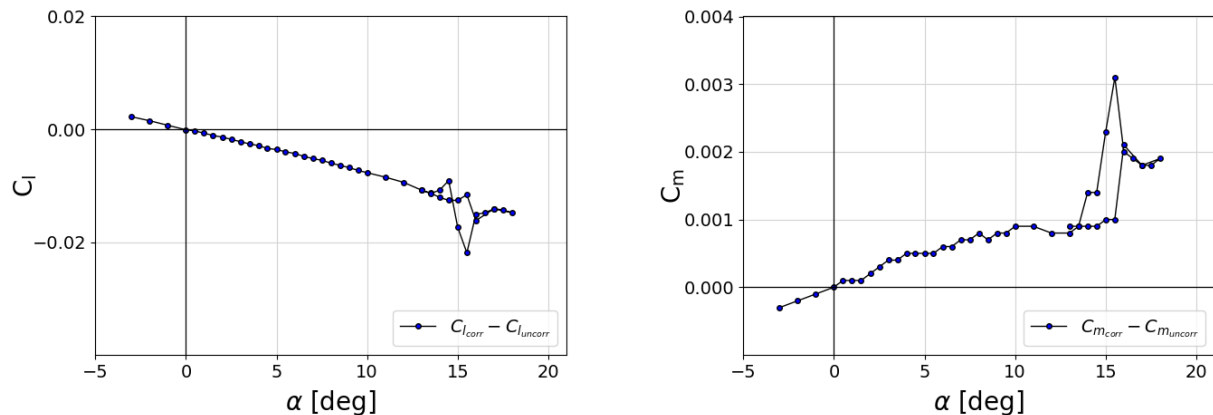


Figure 4.9: Uncorrected and corrected polars for the NACA 64₂A – 015 airfoil tested in the wind tunnel at $Re \approx 860\,000$.

In order to give a better indication of the difference between the two polars, the difference between the polars has been plotted against the angle of attack for the $C_l - \alpha$ and $C_m - \alpha$ polar. The above mentioned changes can exactly be seen in these polars. Even though the polars for the 2D polars have been discussed the same wall corrections apply for the 3D polars. This means that similar results are expected when such an analysis would be done for the 3D polars.



(a) Difference between corrected and uncorrected $C_l - \alpha$ (b) Difference between corrected and uncorrected $C_m - \alpha$

Figure 4.10: A better visualisation of the differences between the two corrected and uncorrected polars

Results 5

In this chapter the results of the simulation and experimental results will be shown, compared and discussed. First in section 5.1, the polars and pressure coefficients obtained through the analysis on the airfoil will be handled. This is followed by section 5.2, in which the same happens but now for a finite wing instead of an airfoil. Thereafter, in section 5.3 the flow phenomena observed on both the airfoil and the wing will be analyzed. In section 5.4, an even deeper look will be taken at several additional research and analysis that could be noted or observed. To conclude, section 5.5 compares the experimental and numerical analysis methods which were used throughout the report, and the benefits and drawbacks of each will be highlighted.

5.1 Airfoil Analysis

In this section the pressure coefficient graphs and polars obtained in the simulation and experiment on the NACA 64₂A – 015 will be discussed. First, the pressure coefficient graphs are analyzed in subsection 5.1.1, which is then followed by an analysis on several different polars in subsection 5.1.2 to 5.1.6.

5.1.1 Pressure Coefficient Graphs

This section focuses on the comparison between the experimental and numerical results of the pressure coefficient graphs. Not all curves will be discussed, but a few important angle of attacks are chosen. The pressure coefficient graphs are presented in order of increasing angle of attack such that the reader may wish to imagine that they are reading the pressures as the airfoil is rotated from -3 degrees to 16 degrees. The C_p graphs for every angle of attack can be found in Appendix A. If the reader wishes to recap on the different part that can be seen in a C_p graph, it is advised to look at Figure 4.2 in chapter 4.

When looking at these graphs one immediate observation can be made with regards to the accuracy of the simulation. For smaller angles of attack the difference between the experimental and numerical result is negligible. This arises from the fact that the pressure at the inner edge and of the outer edge of the boundary layer are equal. Because these pressures are equal the viscosity of the flow does not influence the distribution of pressure around the airfoil. This in turn results in high accuracy of the simulation results as can be seen in Figures 5.1a, 5.1b, 5.1c and 5.1d.

However, for higher angles of attack this argument does not hold. Evidently, at 15°, in Figure 5.1e, it can be clearly seen that according to the simulation the pressure at the upper surface is lower than was measured in the experiment. This is because around 15° the airfoil approaches stall. Fundamentally, this means the air particles near the surface of the airfoil, where lower velocities occur due to friction, cannot climb against the high adverse pressure gradient present. This causes the air particles to reverse direction causing flow separation. However, since these phenomena are viscous effects which XFLR5 is not quite capable of accurately computing, it was to be expected that the software predicted lower pressures than reality. With this in mind, one can have a better understanding when looking at the peculiarities of each graph which will be done below.

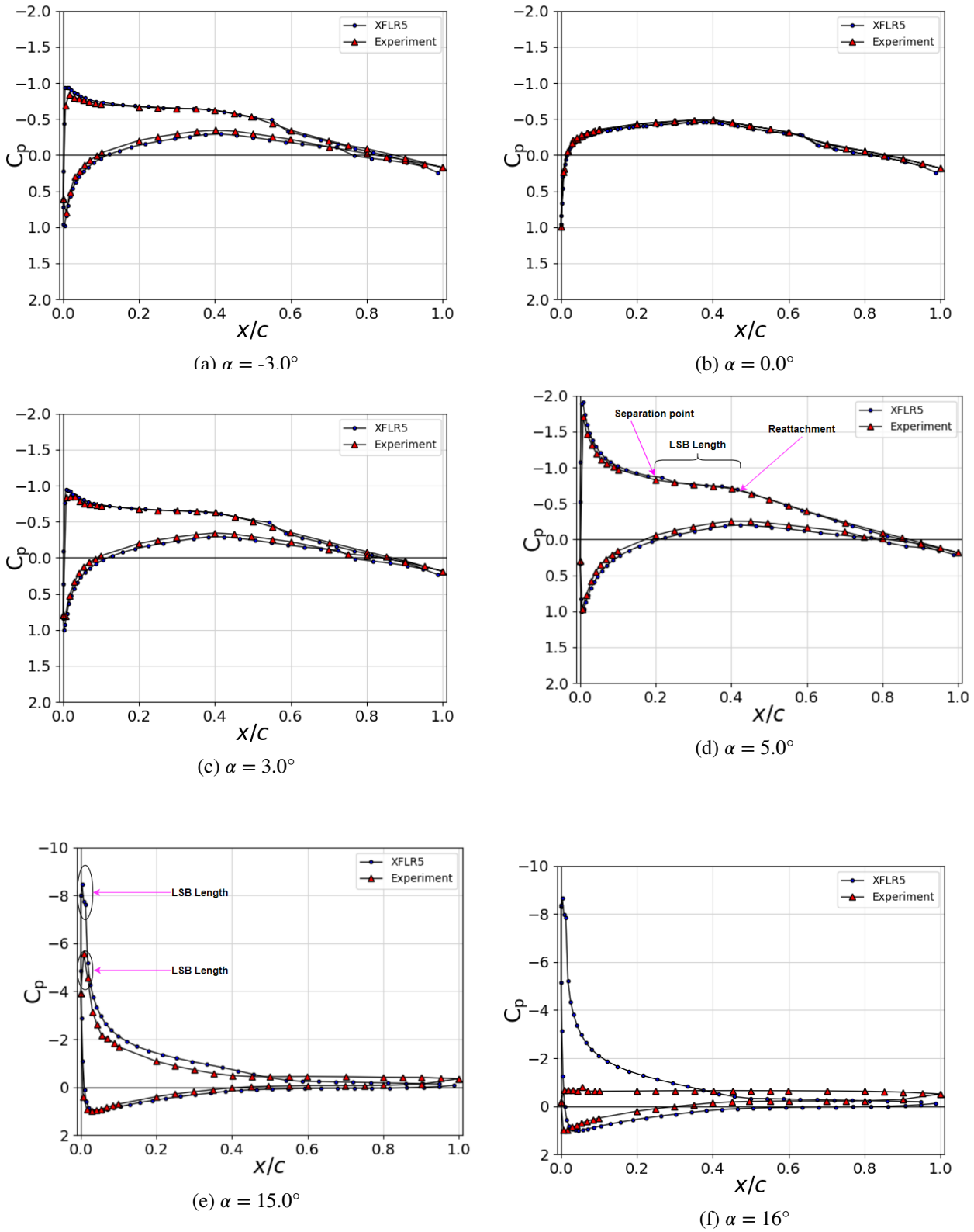


Figure 5.1: C_p vs $\left(\frac{x}{c}\right)$ graphs for the NACA 64₂A – 015 airfoil at various angles of attack simulated using XFLR5 with $Re = 860\,000$ and tested in the wind tunnel at $Re \approx 860\,000$.

-3° AoA

At -3° , in Figure 5.1a, the lower pressure line shown is actually working on the upper surface, meaning that the lift vector is pointing downwards. It also creates negative lift, as a symmetric airfoil creates 0 lift at 0° AoA,

so at lower angles the C_l becomes negative. Both the simulation and experiment yield approximately the same pressure coefficient graphs.

0°AoA

At 0°, in Figure 5.1b, both the upper and lower surfaces show the same distribution. It is interesting to note that the area of the pressure coefficient graph is zero and therefore the airfoil does not provide lift. This is to be expected since the airfoil considered here is symmetric. Another intriguing observation is the location of the position of minimum pressure. According to the 6-digit NACA designation, a NACA 64₂A – 015 airfoil has its location of minimum pressure at 40% of the chord (second digit in the name of the airfoil). [16] This can be confirmed by looking at the pressure coefficient graph. Clearly, at 0.4c the pressure is minimum.

3°AoA

At 3°in Figure 5.1c, as opposed to Figure 5.1a where the lower pressure line is representing the upper surface, in this figure the upper pressure line corresponds to the upper surface resulting in the lift vector pointing upwards. This is because the convention for the direction of the pressure line is into the airfoil/downward positive and out of/ "expanding" the airfoil as negative. The negative pressure lines are the ones that cause lift, as can be seen in Figure 5.2.

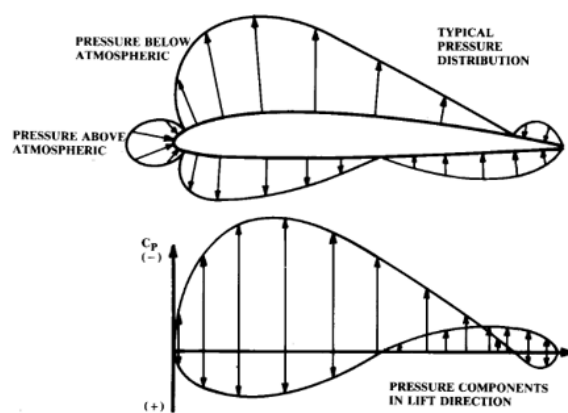


Figure 5.2: Pressure lines on the airfoil for a positive angle of attack [12]

5°AoA

At 5°, in Figure 5.1d, the airfoil produces more lift at than at 3°. This can be seen from the fact that the area of the graph is higher at the former than at the latter one.

However, something that is more interesting is the influence of the laminar separation bubble (LSB) on the C_p graph is visible. The shape the graph shows, is, according to [17] and[18], characteristic for the presence of a LSB. The LSB length is indicated from the separation to the reattachment point within the graph. According to [17] and [18], does the start of the straighter parts indicate the separation point and the knee the reattachment. It should be noted that XFLR5 has also accurately represented this and that the upper line of the XFLR5 pretty much overlaps with that of the experiment.

15°AoA

At 15 degrees, in Figure 5.1e, the shortcomings of XFLR5 start to appear as briefly outlined in the introduction of this section. The difference in the C_p graphs is quite substantial, actually already after an AoA of 1°the

difference between the C_p graphs keeps increasing. This is also what is seen later on in the $C_l - \alpha$ graph of subsection 5.1.2. That mostly shows a difference with the lower line, but a difference in the minimum pressure point is clearly visible around 8° .

In addition to this, the graph shown in Figure 5.1e depicts the point of maximal lift. It can also be noted that the adverse pressure gradient is now really steep and this makes it harder for the laminar flow to overcome this obstacle. Compare this adverse pressure gradient with that of Figure 5.1c, it is much steeper now. In addition to this quite a lot of the airfoil experiences turbulent separation and the LSB is really close to the leading edge as the point with which the LSB length can be indicate is now at around 0 x/c . This is also indicated within the figure for both the simulation and the experiment. The one of the simulation is clearer as the drop and shift are better visible, but the experiment should also have it at that position approximately. Which is later on shown with the help of heat maps.

16°AoA

At 16 degrees, in figure 5.1f, something peculiar has happened; the pressure over the upper surface in the experiment has dropped just below zero. This is because the airfoil reached the stall at an AoA of 15° and now enters the stall region. Still this does not completely explain the sudden drop, this drop is because the laminar separation bubble (LSB) is popped and there is separated and reverse flow now.

Contrary to what happened at the C_p graph of an AoA 5° , it can be seen that XFLR5 did not model this phenomena but just continued with a gradual decrease in the lift coefficient. The reason behind this is highlighted more clearly in section 5.5, but simply said XFLR5 can not simulate the exact boundary conditions happening on an airfoil.

5.1.2 C_l vs α Polar

The wing lift coefficient of the airfoil as a function of the angle of attack is presented in Figure 5.3.

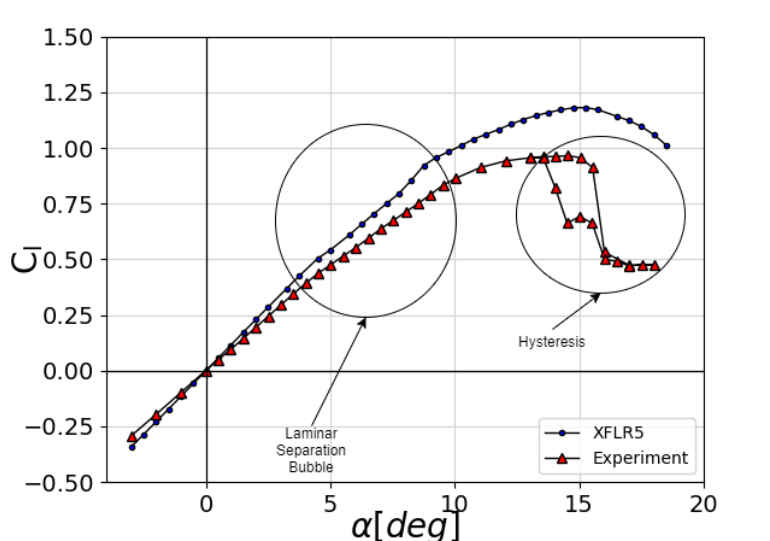
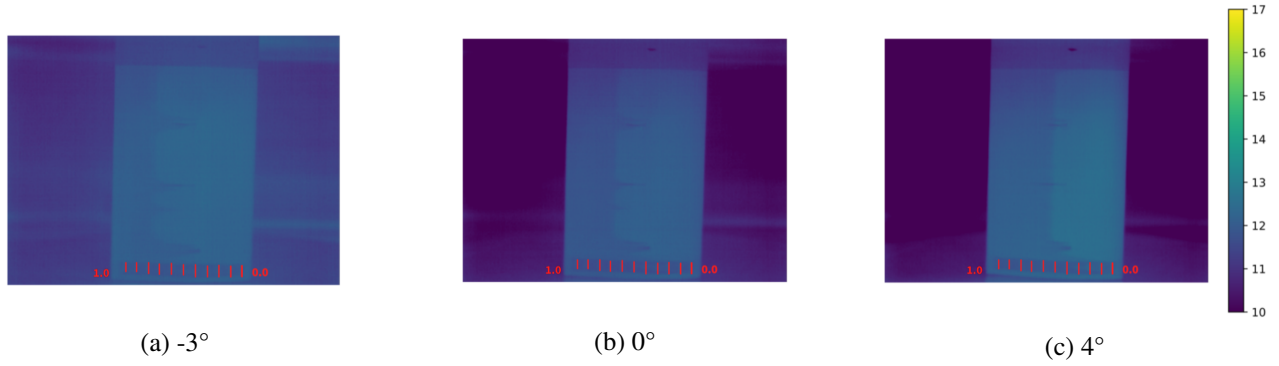


Figure 5.3: C_l vs α polar for the NACA64₂A – 015 Airfoil simulated using XFLR5 with $Re = 860\,000$, and Tested in the Wind Tunnel at $Re \approx 860\,000$.

From -3° to 4° AoA

In this range of angle of attack, the flow is perfectly attached to the surface of the airfoil. The flow is mostly laminar and the transition point is slowly moving forward as can be inspected in Figure 5.4. The darker blue color is the turbulent boundary layer and the lighter blue is the laminar boundary layer.

Figure 5.4: Temperature heatmaps at AoA -3° , 0° and 4°

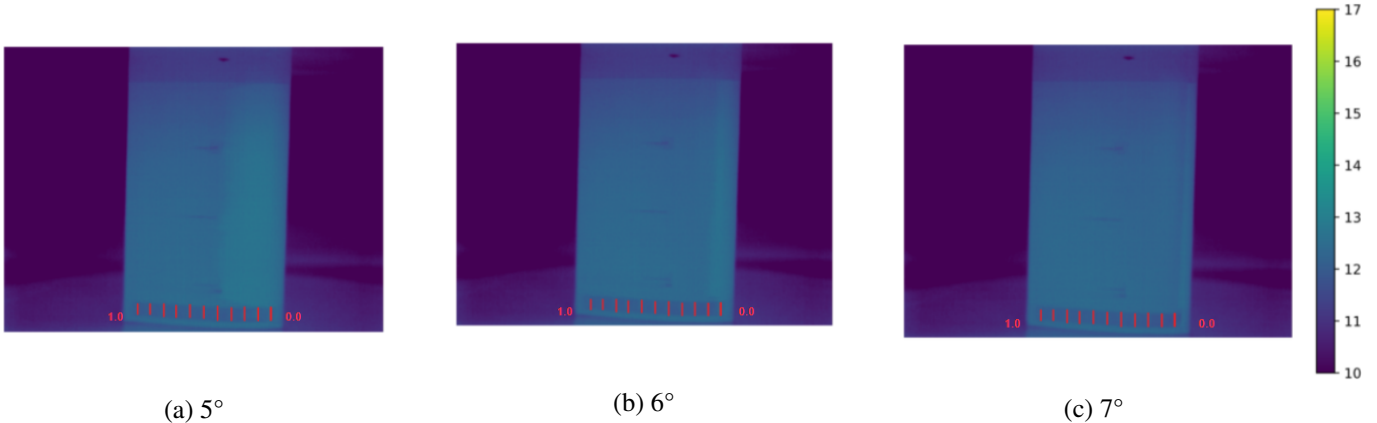
As seen in Figure 5.3 the lift coefficient increases linearly with the angle of attack. This can clearly be seen, as the lift curves from the experimental and numerical results pass through the origin. This confirms that the airfoil is symmetric as it does not provide any lift when the angle of attack is 0 degrees.

Additionally, it is interesting to compare the value of the linear part of lift curve slope with the theoretical result of 2π obtained from thin airfoil theory. The lift curve slope of the experiment is 1.78π . This means that the theoretical curve lies $\frac{\text{theoretical}-\text{experimental}}{\text{experimental}} = 12.3\%$ higher than that of the experiment. The lift curve slope of viscous numerical method is 2.08π , which leads to the theoretical line being $\frac{\text{theoretical}-\text{numerical}}{\text{numerical}} = -3.8\%$ lower than the numerical one.

Another compelling comparison to make is the lift curve slope of the experimental and numerical results. Using the previously determined lift curve slope of 1.78π from the experiment and using a lift curve slope of 2.08π for the viscous numerical result an error of $\frac{\text{numerical}-\text{experimental}}{\text{experimental}} = 16.6\%$ is obtained. This means that the linear part of the numerical curve is 16.6% higher.

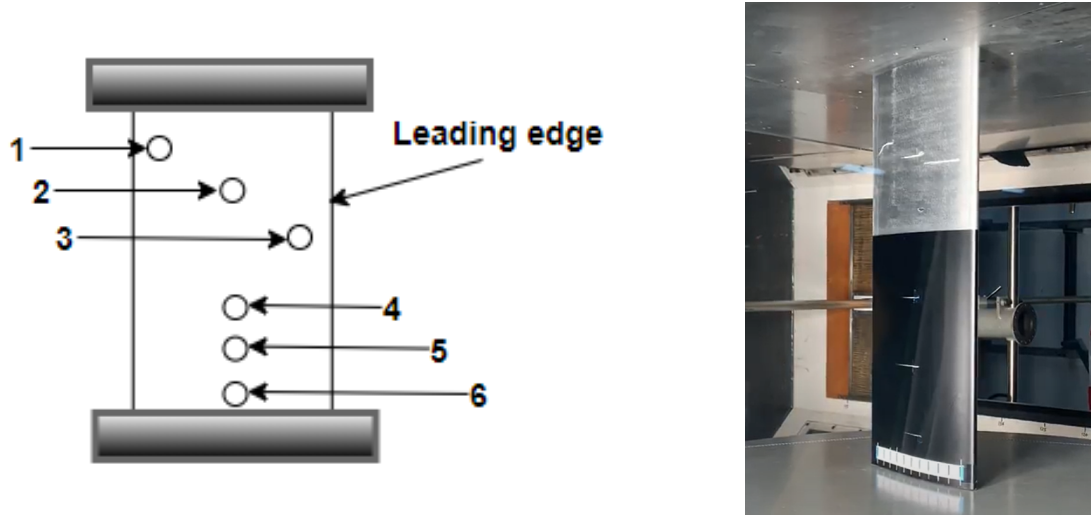
From 4° to 10° AoA

In the range of angle of attack from 4 degrees to 10 degrees the slope of the lift curve has reduced. This is caused by the LSB, for a detailed explanation see section 5.3, but in short; after the reattachment of the LSB there is a turbulent boundary layer, but this will lead to turbulent separation as the angles keep increasing [19]. For lower angles this is not such a problem. In this region of AoA the flow is still completely attached, but the transition point moves more towards the leading edge and this also happens faster. In the range of -3° to 4° the transition point shifted from ~ 0.75 to ~ 0.47 x/c . Now it has shifted from ~ 0.47 to 0 x/c in the AoA range of 4° to 7° , see Figure 5.5.

Figure 5.5: Temperature heatmaps at AoA 5° , 6° and 7°

This is where the distinction between the simulation by XFLR5 and the experiment starts to unfold. Because XFLR5 cannot accurately determine the effect of a turbulent boundary layer this causes XFLR5 to overestimate the lift coefficient at higher angles of attack.

When observing the videos made of the attached tufts to the airfoil at an AoA of 10° , tuft 1 started to move in larger amplitudes, see Figure 5.6. This is because the turbulent separation reached that part of the airfoil [20]. With increasing angles of attack the turbulent separation will move closer to the LSB.



(a) Naming of the tufts on the airfoil (b) Tuft number 1 starts moving in larger amplitudes at 10°

Figure 5.6: Tuft naming and the movement in larger amplitudes of tuft 1

From 10° to 15° AoA

In this range of angle of attack the turbulent separation shifts more forward, which will be better visualised later on in this part. During this period the lift curve starts taking a parabolic shape and also reaches its maximum lift coefficient $C_{l_{max}}$. Both curves start drifting away from each other as XFLR5, as noted earlier, can not accurately predict turbulent and chaotic flow movement. To quantify this error it is interesting to compute the percentage difference between the $C_{l_{max}}$ from the experiment and from the simulation. The $C_{l_{max}}$ for the simulation is 1.1815 and for the experiment 0.965. This means the XFLR5 estimates to $C_{l_{max}}$ to be $\frac{\text{numerical-experimental}}{\text{experimental}} = 22.4\%$ higher than what the experiment yielded.



(a) Tuft 1, 2 and 5 are moving

(b) Tuft 1, 2, 4, 5 are moving with big motions tuft 3 is shaking

Figure 5.7: Tuft agitation on the infinite wing

Next to this, when analyzing the tufts something rather peculiar was happening. On a 2D airfoil it expected that across the whole span the tufts would be moving at that chord position. But as can be seen in Figure 5.7a, at angle of 13 degree the tufts 4, 6 were not moving, while 2 and 5 were with 5 having less movement overall.

Through this it was observed that the length of the tuft and the moment they start moving due to the turbulent separation in big motions are connected with each other. This was confirmed again when the tufts were analyzed at 14.5 degree, Figure 5.7b. Here, tufts 2, 4 and 5 which are located on the same chord position were moving but the smallest tuft 6 was not moving. In addition to this the longest tuft (3) was moving more than the smallest one while being located more towards the leading edge.

Stall and Reconnection

When observing the $C_l - \alpha$ curve for the wind tunnel experiment one notices the erratic drop of the curve. This drop is due to a phenomenon called laminar stall. Laminar stall occurs when the LSB has burst and this will cause region of reverse flow on the airfoils upper side. On Figure 5.8a, the LSB can be seen on the heatmap at the leading edge. The LSB is the dark blue line that is located across the span. In addition to this the heatmaps in Figure 5.8, also show that after the burst occurred on the airfoil the temperature dropped. For the tuft analysis, it is visible in Figure 5.9 that all the tufts are moving due to the burst of the LSB.

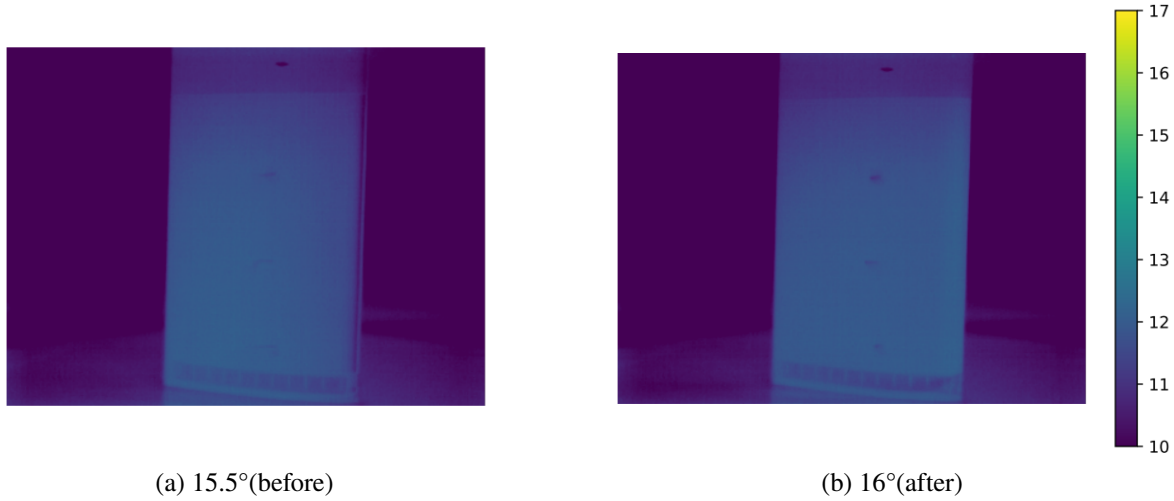


Figure 5.8: Heatmaps before and after the LSB burst



Figure 5.9: Tuft movement at 16 °AoA

Something that is remarkable is that XFLR5 does not have this laminar stall. It even shows a turbulent stall as the stall happens in a gradual way. This can be brought back to the point made earlier at subsubsection 5.1.2, it is hard for XFLR5 to accurately model the turbulent and chaotic movement of the flow. This again leads to the simulation resulting in higher values than the experiment.

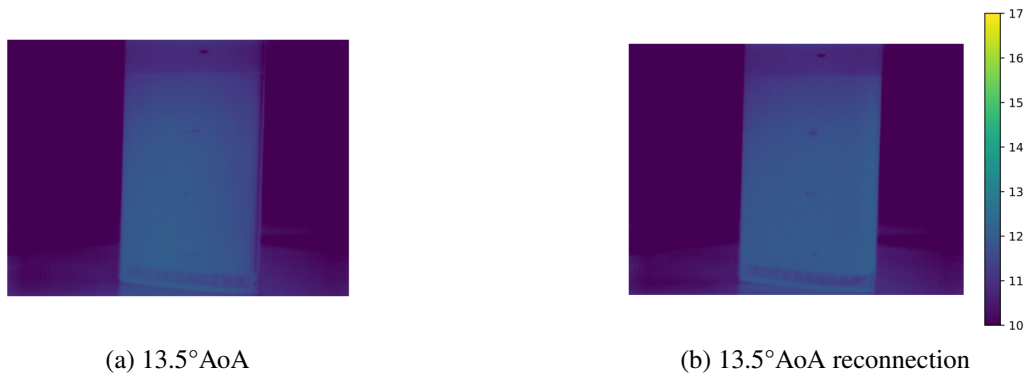


Figure 5.10: Comparing heatmaps at the same angle of attack after reattachment

The final part of the $C_l - \alpha$ curve is called hysteresis and will be discussed in section 5.3 as it is both present in the airfoil and wing measurements. But to give a short description it is the process of reconnecting back to the main $C_l - \alpha$ curve. Observing, the heatmaps show that when the hysteresis reconnects at 13.5° to the main curve that the flow over the airfoil is the same in terms of being completely turbulent flow. But it is less warm than that of the same AoA at before the LSB burst, see Figure 5.10.

5.1.3 C_d vs α Polar

The drag coefficient of the airfoil as a function of the angle of attack is shown in Figure 5.11.

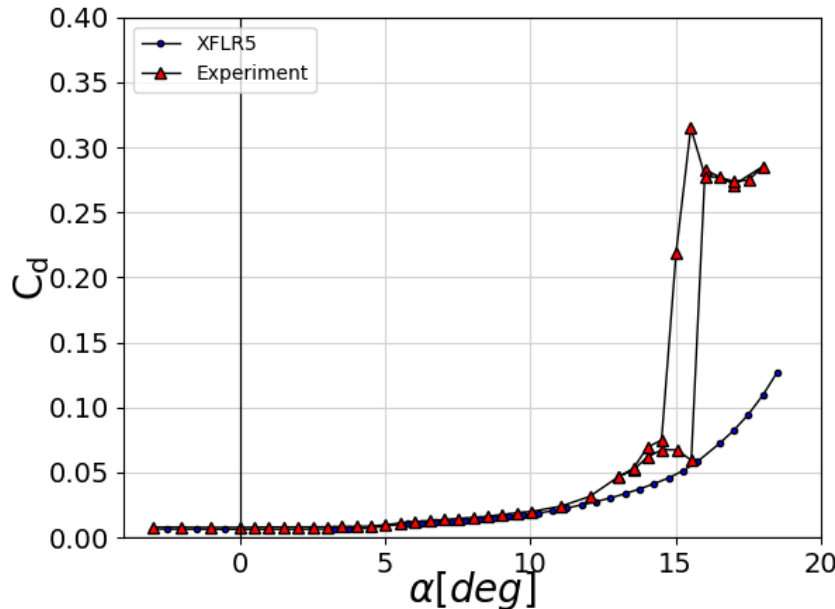


Figure 5.11: C_d vs α polar for the NACA64₂A – 015 Airfoil simulated using XFLR5 with $Re = 860\,000$, and Tested in the Wind Tunnel at $Re \approx 860\,000$

From 0° to 5° AoA

It is noticeable that the drag is constant until an AoA of approximately 5° . This is called a drag bucket and is characteristic of 6-digit NACA airfoils, which belong to the laminar family [12]. This does deviate from the expected value from the NACA number. The design lift coefficient is 0 and the drag bucket extent of the design lift coefficient is ± 0.2 . Looking again at the $C_l - \alpha$ curve this would mean that the drag bucket should continue up to the angle that corresponds to a lift coefficient of 0.2, which is 2° . In reality as can be seen in subsection 5.1.3, it continues up to 3° and after that it slightly increases.

From 5°onwards

The drag coefficient for a given angle of attack from 5 degrees onwards correspond relatively well up until roughly 12 degrees when the experimental values start to deviate greatly. The experimental values of the drag coefficient shoot up from 14.5 degrees onwards. This is around the point at which the airfoil reaches its maximum lift coefficient $C_{l_{max}}$. This sudden spike has to do with the LSB bursting and creating an area of reverse flow which increases the drag immensely.

After this point the experiment shows that the drag remaining somewhat constant with increasing values of the angle of attack. This will be important when observing the $C_l/C_d - \alpha$. The experiment then also starts the hysteresis loop from 18 degrees onwards. It is also interesting to note that the predicted drag coefficient by XFLR5 varies smoothly as opposed to the experimental values. This is not to say that XFLR5 did not predict the LSB, but rather it did not predict the turbulent separation accurately at higher angles of attack and the burst of the LSB. This can be noted by the lines of the experiment and XFLR5 basically overlapping between 5° and 10.5 °.

5.1.4 C_l vs C_d Polar

The C_l vs C_d polar, also called the lift-drag polar, depicts the lift coefficient for each drag coefficient. The ratio of these two coefficients is a good measure of aerodynamic efficiency and therefore this chart can be used to extract useful information regarding this property. As opposed to the previously discussed polars which were analysed on certain angle of attack intervals, this polar will be discussed on intervals of the drag coefficient.

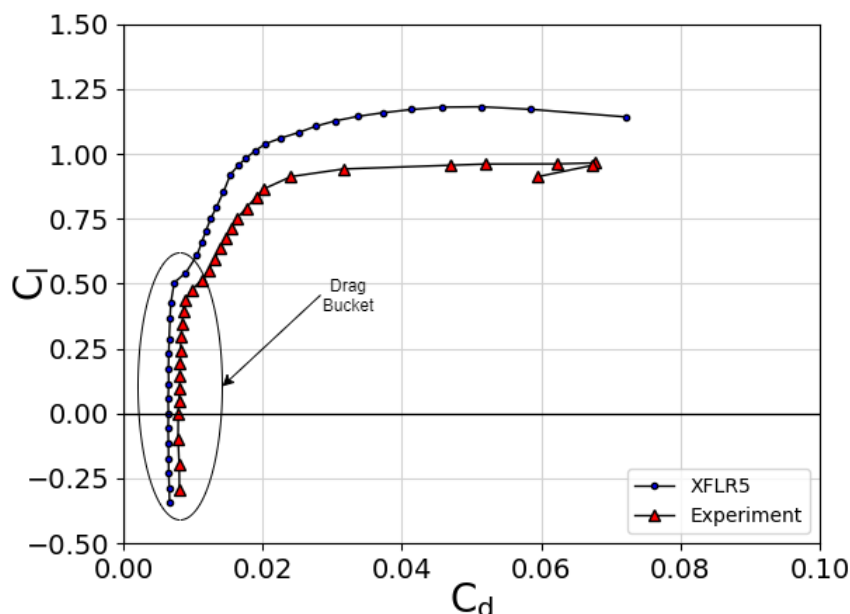


Figure 5.12: C_l vs C_d polar for the NACA64₂A – 015 Airfoil simulated using XFLR5 with $Re = 860\,000$, and Tested in the Wind Tunnel at $Re \approx 860\,000$.

From 0 to 0.01

In this range of drag coefficients one very interesting observation can be made with regards to the shape of this graph: a so-called drag bucket exists, which has been discussed briefly in section 5.1.3. A drag bucket is a range of lift coefficients where drag is minimum. This can be identified in the graph as the points where the lift coefficients can increase or decrease without a change in drag coefficient resulting in a bucket shape. Since this range is at relatively low drag coefficients — and therefore low angles of attack — the experimental and numerical values correspond comparatively well in this range.

From 0.01 to 0.02

It is in this range of drag coefficients that the drag bucket disappears meaning that an increase in lift coefficient results in an increase in drag coefficient. Additionally, the experimental and numerical values diverge from each other with increasing drag coefficient. This is because the boundary layer has become turbulent and there is a LSB present as mentioned before.

From 0.02 onwards

From a drag coefficient of 0.02 onwards the lift coefficient barely increases but the drag coefficient does increase. This corresponds to the parabolic part of the $C_l - \alpha$ curve and the increase in C_d in the $C_d - \alpha$ curve. This is actually the airfoil stalling albeit seen from a different perspective. As was the case for the previous range of values, the difference between the experimental and numerical values has become comparatively large.

5.1.5 C_l/C_d vs α Polar

In this section, the graph of C_l/C_d over alpha, which can be seen below in Figure 5.13, will be analyzed.

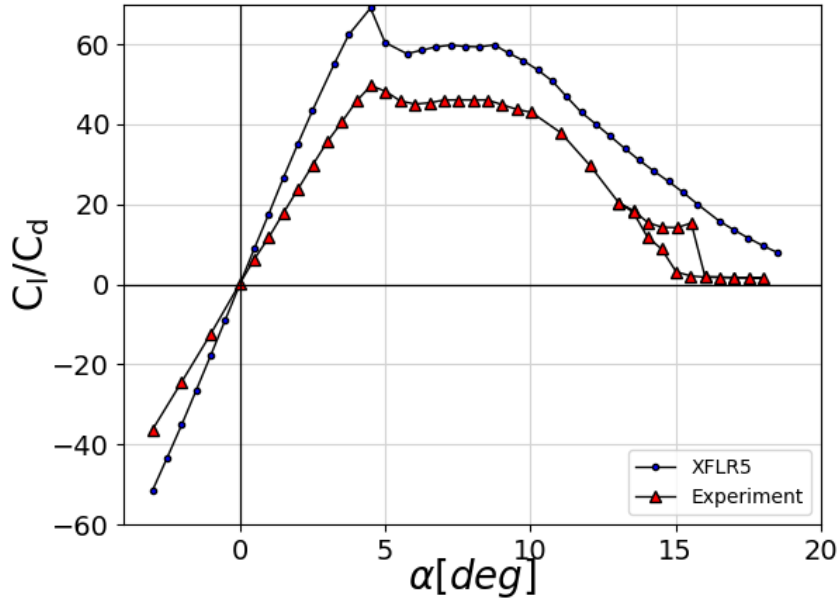


Figure 5.13: $\frac{C_l}{C_d}$ vs α polar for the NACA64₂A – 015 Airfoil simulated using XFLR5 with $Re = 860\,000$, and Tested in the Wind Tunnel at $Re \approx 860\,000$.

From -3° to 4.5° AoA

In this range of angle of attack, the behaviour of both the experiment and simulation graphs are linear and pass through the origin. It can be seen that the simulation graph has a higher slope than the experiment graph. This can be explained by the fact that, while in this range the drag coefficients are almost identical between simulation and experiment, but the absolute values of the lift coefficients predicted by the simulation are consistently higher than the values recorded during the experiment. This results in lower lift-over-drag ratios below 0 degrees and higher lift-over-drag ratios above 0 degrees. As can be seen in the graph, this holds for all of the measured angles of attack, not only the range discussed in this section. At an angle of attack of 4.5 degrees, the maximum lift-over-drag ratio for both the simulation and experiment graph is reached.

From 4.5°to 9°AoA

After reaching the maxima, both the simulation and experiment graphs decrease slightly until 6 degrees, after which both graphs hit a plateau. The plateau can be explained graphically by looking at Figure 5.12, which is the C_l -over- C_d graph. It can be seen that between a C_d of 0.012 and 0.017, which correspond to angles of attack of 6 and 9 respectively, the graphs for simulation and experiment are approximately linear. This means that the ratio C_l over C_d stays constant between 6 and 9 degrees. There is also an explanation available with regards to the aerodynamic behaviour which becomes clear if Figure 5.3 is noted, since between 6 and 9 degrees the airfoil shows the effect of the Laminar Separation Bubble. It can thus be concluded that in this region the Laminar Separation Bubble results in a constant C_l/C_d , which is lower than the peak C_l/C_d .

From 9°AoA onwards

In this region, both graphs experience a decrease in lift-over-drag ratio. From around 11 degrees, this decrease is linear. It can be seen that the slope of the experiment graph is less steep than the simulation graph. This is because stall is reached but for the experimental graph the C_l stays approximately constant while the C_d keeps increasing drastically causing a more drastic change in the slope. For the simulation however the drag coefficient increase is more constant and there is also more increase in the C_l .

At around 15.5 degrees, a steep drop in the experiment graph can be seen, while the simulation graph keeps decreasing linearly. This is due to laminar stall. As mentioned in subsection 5.1.2, laminar stall is initiated by leading edge separation, resulting in unattached flow over the entire airfoil. In the C_l -over-alpha curve in Figure 5.3, it can be seen that laminar stall results in a dramatic reduction in the value of the lift coefficient, while an increase in the drag coefficient can be noted in Figure 5.11, which then translates into a drop in lift-over-drag ratio. As again mentioned in subsection 5.1.2, XFLR5 does not simulate laminar stall, which explains why the described behaviour does not occur in the simulation graph. The hysteresis loop previously described in the sections analyzing C_l over alpha and C_d over alpha is also visible in this graph.

5.1.6 C_m vs α Polar

The moment coefficient of the airfoil as a function of the angle of attack is given in Figure 5.14.

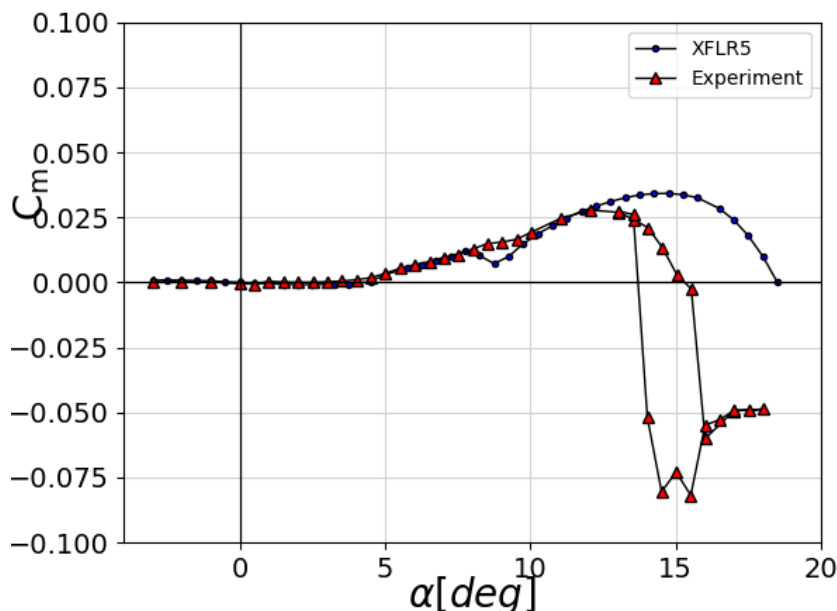


Figure 5.14: C_m vs α polar for the NACA64₂A – 015 Airfoil simulated using XFLR5 with $Re = 860\,000$, and Tested in the Wind Tunnel at $Re \approx 860\,000$.

AoA 0°to 4°

The pitching moment coefficient is the relation between the lift- and drag coefficient with the centre of pressure. The lift and drag act at the centre of pressure but as the centre of pressure moves at increasing angle of attack a fixed point is chosen, during the experiment and simulation this was the leading edge. In this range of AoA, the pitching moment coefficient stays relatively constant around zero and not much can be noted about it. Later on when compared to the inviscid conditions (see subsection 5.4.2), it becomes clear that viscous effects cause this zero C_m .

AoA 5°to 12°

An increase in the moment coefficient is seen in both the numerical simulation and the experiment. The increase in the moment coefficient starts when the second linear part of the $C_l - \alpha$ curve initiates. At that angle of attack the LSB also started and the transition point shifted more towards the leading edge, so this change can be traced back to be caused by the forming of the LSB and shifting of the transition point. Next to this, as mentioned numerous times now, turbulent separation played a part. Nevertheless, the effect of the turbulent separation is seen better after 7.5 °where the some what linear increase stops and a parabolic shape is initiated.

AoA 12°to reattachment

From 12°onwards the moment coefficient starts to decrease for the experiment. However, when the stall angle is reached, an abrupt drop is noted and that is characteristic of laminar stall [21]. Increasing the angle of attack will not change the location of the centre of pressure as all the of the flow is separated on the upper half of the airfoil. When the angle of attack decreases to form the hysteresis and reattach to the main curve, it can be noted that the moment coefficient at first decreases even more. Nevertheless, at 14°it increases drastically meaning the normal conditions will be achieved again.

For XFLR5 the moment coefficient changes gradually and decreases likewise after stall. However, due to the fact that the LSB burst is not simulated and that turbulent conditions are hard to predict, the drop is gradual.

5.1.7 Conclusion Airfoil Analysis

In the 2D analysis for both the simulation and the experiment the pressure coefficient graphs and the different polars are discussed. From these polars the effect of the laminar separation bubble became clear before and after it has burst. Before bursting, the main effects of the LSB were that a second linear part with a lower gradient was introduced in the $C_l - \alpha$ curve, an increase in the drag coefficient and an increase in the pitching moment coefficient. After bursting, the effects of the LSB are severely detrimental, and overcoming it is practically impossible. This is because it leads to a sharp drop in the lift coefficient while the drag coefficient is increasing drastically. Additionally, the moment coefficient shifts drastically towards a negative value instead of positive.

5.2 Wing Analysis

In this section, the polars obtained from the experiment and the simulation using XFLR5 on the 3D wing will be discussed. First, several different polars will be analyzed in subsection 5.2.1 to 5.2.5. This is followed by a conclusion, which can be found in subsection 5.2.6.

5.2.1 C_L vs α Polar

In this subsection, the plot of the wing lift coefficient as a function of the angle of attack will be analysed and compared to the results from the simulations performed by XFLR5. As this curve is central to any wing analysis, it will be discussed thoroughly through different portions of angle of attacks. The $C_L - \alpha$ polar is presented in Figure 5.15.

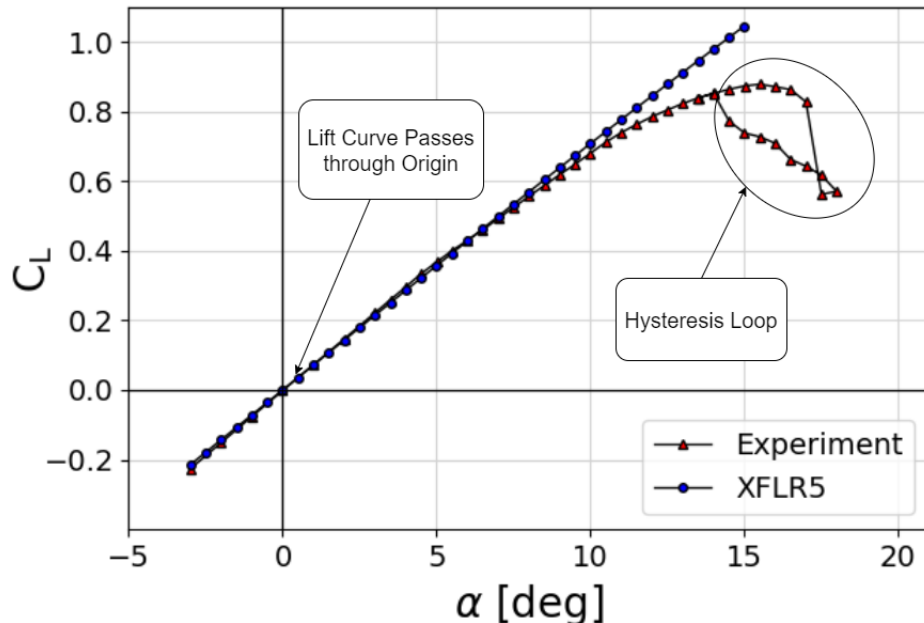
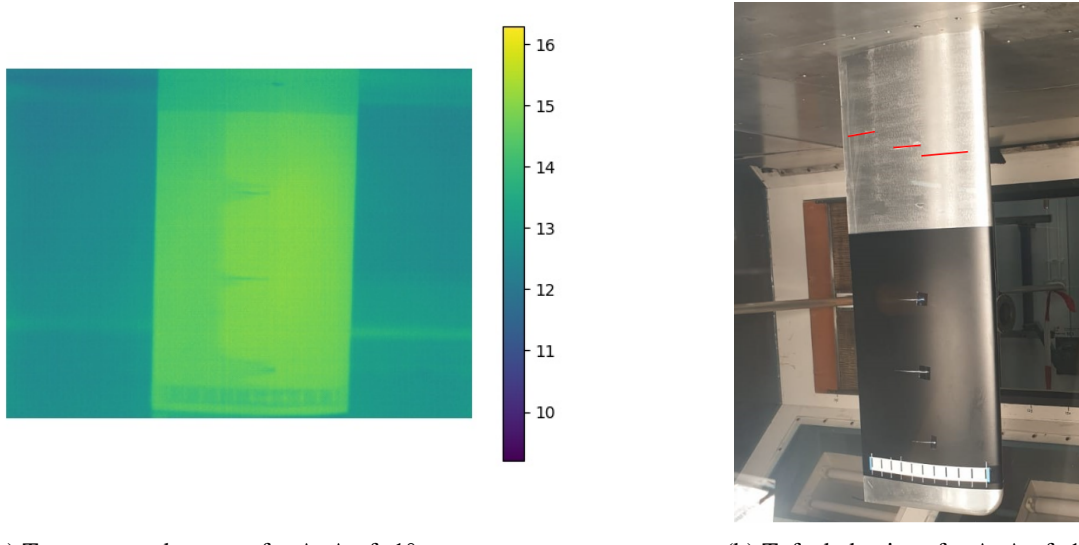


Figure 5.15: C_L vs α polar at $V = 51.69$ m/s

From -3° to 4° AoA

In this range of angles of attack, the flow is still completely attached and the transition occurs at about 0.7 x/c of the chord along the complete span as can be seen from the temperature distribution over the wing in Figure 5.16a. As explained in chapter 2, the larger temperature means that the boundary layer absorbs less energy and therefore the flow is laminar and the opposite is true for turbulent. This transition position very slowly decreases down to about 0.6 x/c of the chord along the span at 4°(see Figure 5.17a) but most of the flow still stays laminar. Another perspective of the same flow is given by Figure 5.16b which shows that the tufts are still completely aligned with the flow direction, meaning that no separation has occurred. Note that a red line was drawn on the tufts to improve the visibility of their position. On both figures, the flow comes from the right side.

(a) Temperature heatmap for AoA of -1° (b) Tufts behaviour for AoA of -1° Figure 5.16: State of the flow at AoA of -1°

As the flow is still attached and mostly laminar, the viscous effects are a lot smaller than for a detached and turbulent flow and therefore the simulation from XFLR5 agrees very well with the experimental results. In this range of angle of attacks, it is seen that the polar is completely linear and the slope of this region can be determined. This can be compared to the thin airfoil theory stating that the slope of the linear part of the $C_l - \alpha$ curve has a slope of 2π [6], and that the slope of the wing polar is given by Helmbold equation (5.1)[1].

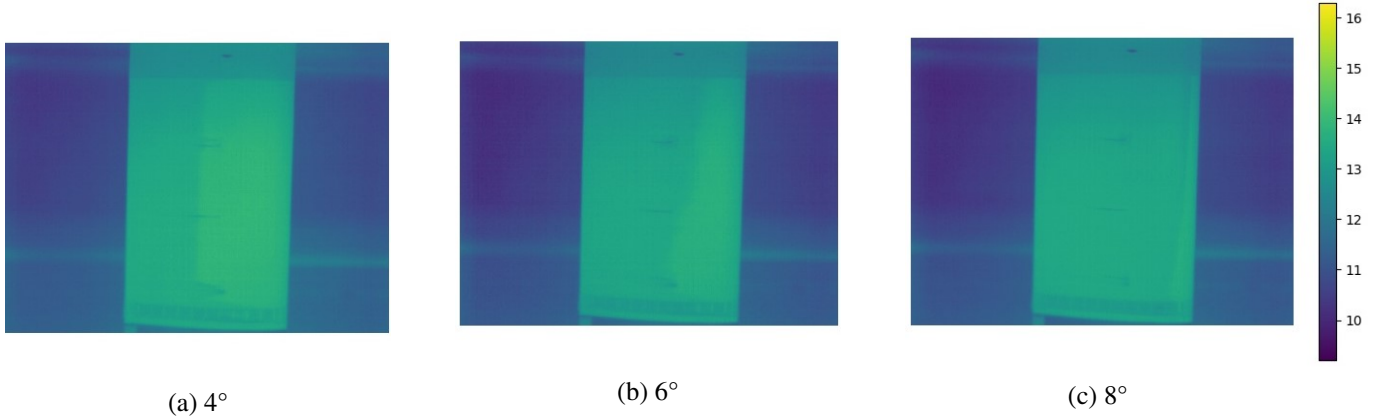
$$C_{L_\alpha} = C_{l_\alpha} \cdot \frac{A}{\left(\frac{C_{l_\alpha}}{\pi} + \sqrt{\frac{C_{l_\alpha}}{\pi}^2 + A^2} \right)}^{\text{TWT}} = C_{l_\alpha} \cdot \frac{A}{2 + \sqrt{4 + A^2}} \quad (5.1)$$

From this equation, it is then expected that the slope of the wing polar will be smaller than the airfoil polar. This comes from the trailing vortices that are present on a 3D wing (finite aspect ratio) and not on an airfoil. From Equation 5.1 and the aspect ratio of 5.35 determined in chapter 2, using thin wing theory and $C_{l_\alpha} = 1.78\pi$ per rad from subsection 5.1.2, the predicted slope of the linear part of the polar is 1.28π . While the one found from the experimental data is determined to be 1.33π per rad. The relative error of the theory with respect to the experimental results is then found to be $\left| \frac{\text{theory} - \text{experiment}}{\text{experiment}} \right| = 3.55\%$. This shows that the thin wing theory is fairly accurate but slightly underestimating the actual slope of the polar.

It is also noted that the polar goes through the origin of the graph which confirms that the airfoil is symmetrical as could be seen from its naming: NACA 64₂A – 015.

From 4° to 8° AoA

Over this region of angles of attack the flow is still completely attached but the transition moves to the leading edge faster than previously. Indeed, from -3° to 4° AoA, the position of the transition was changed from 0.7 x/c of the chord along the entire span to 0.6 x/c fairly slowly (over 7° AoA). Therefore, as no significant change was happening in this range (transition and separation), the slope was nearly perfectly constant between two data points. However, from 4° to 8° , the transition position changes from about 0.6 x/c of the chord to the LE suddenly. This can be seen in Figure 5.17.

Figure 5.17: Temperature heatmaps at AoA 4° , 6° and 8°

The reason for this fast change comes from the formation of the boundary layer at an AoA of about 5° . As will be explained in subsection 5.3.1, the flow right after the re-attachment of such Laminar Separation Bubble is turbulent. Therefore, as it forms along the span, the complete flow on the wing becomes turbulent (as the bubble forms at the LE). It is also noted that generally the position of the transition from a laminar to turbulent flow is not constant along the span. This is mainly the case because of the effective angle of attack not being constant across the entire span (see section 5.4) and therefore the LSB is not directly to be seen across the entire span. Note that the bubble cannot be seen on the infrared images from Figure 5.17 as it was just formed.

One of the effects of this fast change in the transition position is that the flow suddenly becomes mainly turbulent at angles of attack above $4\text{-}5^\circ$ and the size of the boundary layer suddenly increases. The slope of the lift curve therefore decreases as the flow will perceive a shape different from the actual wing (thicker). The slope of the line between two data points on Figure 5.15 is given in Figure 5.18 and is about 1.09π per rad.

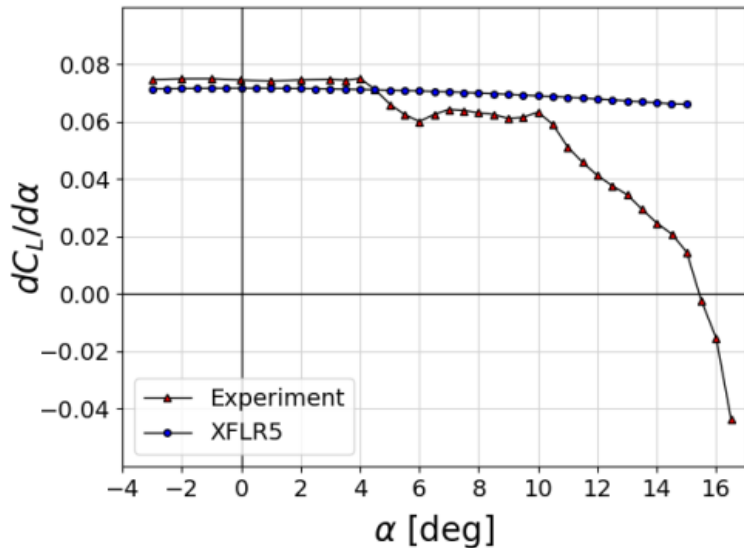


Figure 5.18: Slope between two points on Figure 5.15 as a function of the angle of attack

It can thus be seen from Figure 5.18 that the linear behaviour that was present from -3° to 4° becomes quadratic between 4° and 6° before again having a second approximately linear portion from 6° to 10° . This second linear portion comes from the LSB that will deform the airfoil seen by the flow. This is further explained in subsection 5.3.1.

From 8°to 10°

From 8°to 10°, not much changes compared to the previous range. Though, the transition completely occurs at the LE along the complete span and therefore the flow is completely turbulent over the wing as can be seen in Figure 5.19. This range is still considered apart from the previous one as the deviation from the XFLR5 simulation becomes more clearly visible on Figure 5.15. From Figure 5.18, it is seen that the lift polar is still approximately linear over this region of AoA's but is also a lot less stable than on the first linear region. This mainly comes from the fact that turbulent separation slowly starts to occur at the trailing edge (TE). This, however, can only very slightly be seen on the image of the tufts and therefore no figure is provided. It is still noted that only the very end of the TE tuft at the root is agitated at angles of attack of 9°and 10°. There, the linearity is completely lost as will be seen in the next sub-subsection.

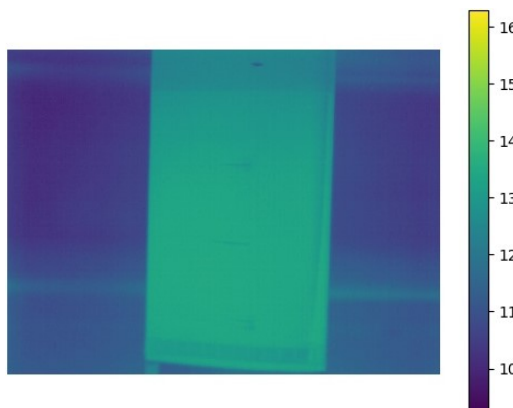


Figure 5.19: Temperature heatmap for AoA of 9°

From 10°to 15.5°

In this range of angles of attacks, the curve is not linear anymore as can be seen from Figures 5.15 and 5.18. The flow over the wing is also completely turbulent and the laminar separation bubble continues to grow over the airfoil. The shape of the lift polar curve takes a quadratic form which describes the stall behaviour of the wing, reaching a maximum value at an angle of attack of 15.5°. The wing therefore attains a maximum of the lift coefficient of $C_{L_{max}} = 0.8792$ at a 15.5°AoA. An essential feature of the $C_L - \alpha$ polar is the stall behaviour but XFLR5 fails to describe it. This comes from the fact that the software uses the results from the airfoil analysis as a way to account for viscous effects by interpolation in parallel to the VLM (see chapter 3). But the C_l itself comes from a linear calculation taking viscous effects into account, therefore the linearity.

The stall behaviour shown by the wing is a bit uncommon for an airfoil having a thickness being $(t/c)_{max} \geq 14\%$, as the NACA 64₂A – 015 is (15% thickness). Under most different flow conditions, no LSB is formed, and the stall behaviour is a lot smoother as seen in Figure 5.20. Indeed, such bubble can form for any airfoil but only under quite specific flow conditions[22].

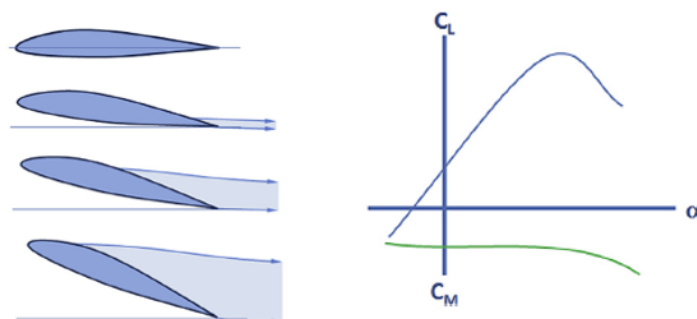


Figure 5.20: Typical stall behaviour for $(t/c)_{max} \geq 14\%$ wings from [12]

It is important to point out that there is a critical difference between Figures 5.20 and 5.15 which concerns laminar separation. Indeed, the latter shows a more brutal drop in C_L values than the other. Note that at the maximum wing lift coefficient, complete separation has not yet occurred. This is shown by the agitation of the tufts placed on the wing from Figure 5.21. As can be seen, only the two rear ones at the root are agitated, meaning that separation is not yet happening at the leading edge. The mid-chord tufts at the tip of the wing are also not yet agitated.



Figure 5.21: State of the tufts at an AoA of 15.5° for maximum lift coefficient



Figure 5.22: State of the tufts at an AoA of 18°

The type of stall actually seen on Figure 5.15 is typical for a laminar stall. Laminar separation occurs when a LSB is formed on the airfoil and bursts at some angle of attack. At the burst, a sudden drop in lift coefficient occurs as the flow becomes entirely separated.

From 15.5° to 18°

From AoA of 15.5° and 18°, the separation bubble continues to spread until the LE while the flow is still completely turbulent. Complete leading edge separation over the whole wing occurs at an angle of attack between 17° and 18°, this explains the sudden drop in lift coefficient between those two values. The tufts used to understand this are shown in Figure 5.22.

From 18° to 14°

In this range of angle of attack, the phenomenon of Hysteresis is investigated. This concerns the reattachment behaviour of the wing after reaching deep stall at an AoA of 18°. Though, as it is a phenomenon that is highly relevant for the comparison between the airfoil and wing comparison, a more thorough explanation is given in section 5.4.

5.2.2 C_D vs α polar

In this subsection, the C_D vs α polar obtained from the XFLR5 simulation and the experimental data is discussed, analyzed and compared. This section is essential to understand and demonstrate the influence of viscosity in the overall drag of the wing through comparison with the XFLR5 results.

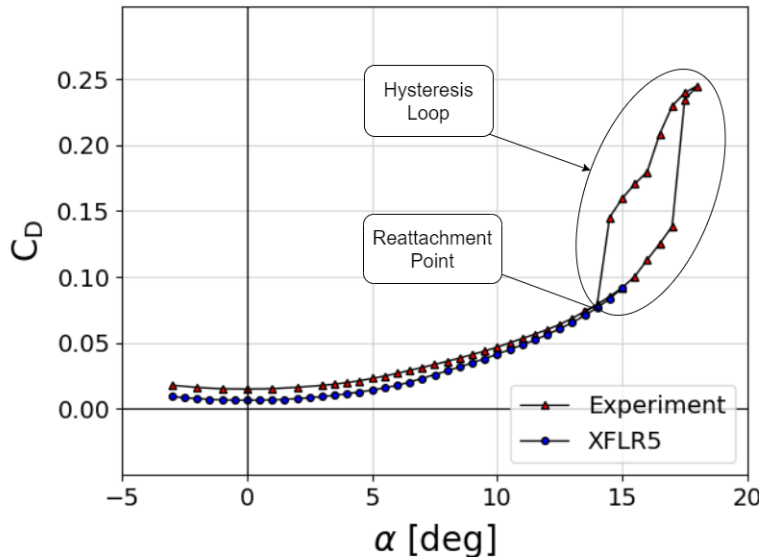


Figure 5.23: The drag coefficient, C_D , plotted against the Angle of Attack, α , at $V=51.9$ m/s

As can be observed in Figure 5.23, the wing drag coefficient increases in a parabolic fashion as the angle of attack deviates from 0 degrees. This can be interpreted, in a practical sense, as being the result of the increased frontal area that the flow "sees" as it approaches a more inclined wing. However, this definition is limited as it does not contemplate for the effect of drag-generating effects, such as wingtip vortices. Consequently, it would be more accurate to say that the (3D) wing drag coefficient arises from various effects, of which the most important for this experiment are form drag, skin friction drag and induced drag. Form drag is particularly readily obtained through software such as XFLR5, as it simply originates from the pressure distribution dictated by the shape of the body [6]. The issues come to be when considering the latter two, as skin friction drag is an effect that is a byproduct of the viscosity of air, which, as was explained in chapter 3, is not contemplated effectively in XFLR5, while the induced drag is a result of the aforementioned vortices, which are not modelled perfectly due to the flat wake.

As a result of these differences between reality and the simulation, a substantial difference is generated in the drag coefficient, with the experimental values being larger than the simulation ones. This is not captured effectively in Figure 5.23 due to the large values for the drag coefficient at large angles of attack, but in reality at low and medium angles of attack (-3 to 12.5) the difference is very large at 65 drag counts on average, with a maximum difference of 91 drag counts at an angle of attack of 6 degrees. As was expected, due to the theory that is applied to the simulation, the VLM underestimates the true drag that is experienced by the wing, which will inevitably result in an overestimation of glide characteristics in the C_L/C_D . Furthermore, despite XFLR5's attempts to correct the lack of consideration of viscosity by extrapolating 2D viscosity from XFOIL into the 3D wing, the results are still not correlated to reality.

Nevertheless, the simulation correctly identifies the quadratic nature of the drag polar from -3 to 15 degrees, that is until substantial flow separation becomes the dominant factor to determine the drag coefficient. After this occurs, at roughly 15.5 to 17 degrees, the drag coefficient suffers a large increase due to the large amount of pressure that has large components in the direction of the drag force, jumping to a maximum drag coefficient of 2448 drag counts at 18 degrees of angle of attack. Following this maximum angle of attack, it was reduced in efforts to reattach the flow, which created the hysteresis loop denoted in Figure 5.23. Finally, flow reattachment was achieved by lowering the angle of attack to 14 degrees, demonstrating the large reduction in angle of attack needed in order to reattach the flow.

5.2.3 C_L vs C_D Polar

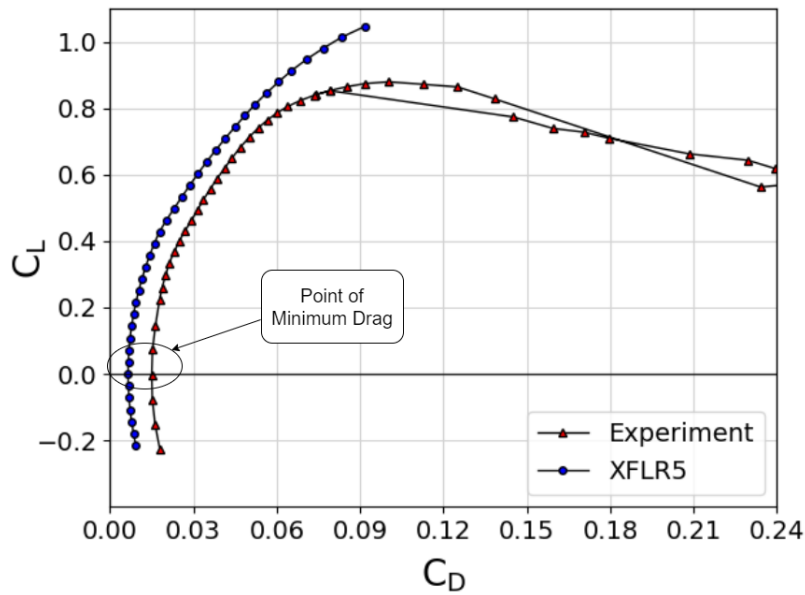


Figure 5.24: The lift coefficient C_L plotted against the drag coefficient C_D at $V=51.9$ m/s.

The next polar to be analyzed is the so-called "lift-drag polar", in which the lift coefficient (denoted as C_L) is plotted against the drag coefficient (denoted as C_D). As explained earlier, the ratio between the lift coefficient is generally an accurate measure of the efficiency of the wing geometry. The higher the C_L/C_D ratio, the more efficient the wing geometry.

The analysis of this polar will follow a slightly different structure than previously. Because this polar does not have the angle of attack as its x-axis, it is not logical to break down the analysis into increments of angles of attack. Instead, the analysis will be broken down into increments of C_D , as that is what lies on the x-axis.

From 0.00 to 0.09

There are a number of interesting observations that may be taken from the very left hand side of this graph. Firstly, it is interesting to see that there is no noticeable drag bucket present in this polar. This is a stark contrast to the 2D airfoil polars, where the drag bucket could be fairly easily seen. The likely cause of this would be the effect of the wing tip on the overall wing performance. The wing tip increases the drag caused by the wing as a whole. This is due to a phenomena known as tip vortices (more in depth explanation will come later). This effect is very sensitive to the value of lift coefficient. Therefore, even at low lift coefficient values, the minimum drag coefficient does not flatten out (drag bucket), as every slight change in lift coefficient will result in a change in drag coefficient. As a result, the drag polar for a 3D wing will always be more parabolic than the 2D airfoil. This is exactly what is observed between the two graphs.

The second (and perhaps more interesting) observation is that it can be immediately seen that the XFLR5 software is very effective in estimating this polar at low drag coefficients. The shape of the theoretical and experimental curves are uncannily similar. The only noticeable difference is that there is a small offset between the two curves, which remains fairly constant throughout the entirety of this interval. The source of this offset is not certain, however, there are some clues which could shine more light on it.

1. At low angles of attack (and hence, low drag coefficients), the XFLR5 software approximates the lift coefficient almost perfectly, as can be seen in Figure 5.15. This explains why the shape of the curve is almost perfect in Figure 5.24 too. Therefore, the offset is unlikely to be due to inaccuracies in the lift coefficient estimation.

2. Upon looking at Figure 5.23, it can be seen that there is a slight discrepancy between the simulated drag coefficient and the actual drag coefficient. This likely suggests that the source of error originates from inaccuracies in measuring C_D .
3. In both Figure 5.23 and Figure 5.24, the simulated drag coefficient is estimated to be lower than the realistic drag coefficient. Therefore, the simulation must have overlooked a certain component of the drag coefficient throughout its analysis.

Taking all these factors into account, it is important to consider the possible mistakes that the XFLR5 software makes when estimating the drag coefficient of the wing. The largest of these errors is the "inviscid flow assumption". What this means is that the XFLR5 assumes a flow with viscosity to be travelling over the wing. The effect of the viscosity The practical reason for this is that there is no theory sufficient for 3D modelling of viscous drag. However, what this means is that there will always be a slight difference between simulated and real drag coefficients (especially at low Reynolds numbers, which is 860000). The viscous drag coefficient is given according to the equation:

$$C_{Dv} = \frac{D_v}{1/2 \cdot \rho \cdot S \cdot V^2} \quad (5.2)$$

Where D_v is the viscous drag, C_{Dv} is the viscous drag coefficient, ρ is the air density, S is the wing area and V is the flow speed. As all of these parameters are kept constant throughout the entirety of the simulation and experiment, it may be deduced that an error with the the viscous drag coefficient will likely cause a quasi constant offset between simulated and real values of drag coefficient. This is exactly what is noticed in Figure 5.24. Therefore, it is likely that the "inviscid flow assumption" is the source of the error in the graph.

From 0.09 to 0.24

There is one final observation that should be noticed on the right hand side of this graph: XFLR5 is not capable of modelling stall behaviour. As soon as the drag coefficient reaches 0.09 and the wing begins to stall, the XFLR5 runs into errors. As a result of this, the simulated drag polar does not extend further. Furthermore, other phenomena such as hysteresis loops may not be modelled either. This was already noticed in the previous polars and further reinforces one of XFLR5's largest weaknesses.

5.2.4 C_L/C_D vs α Polar

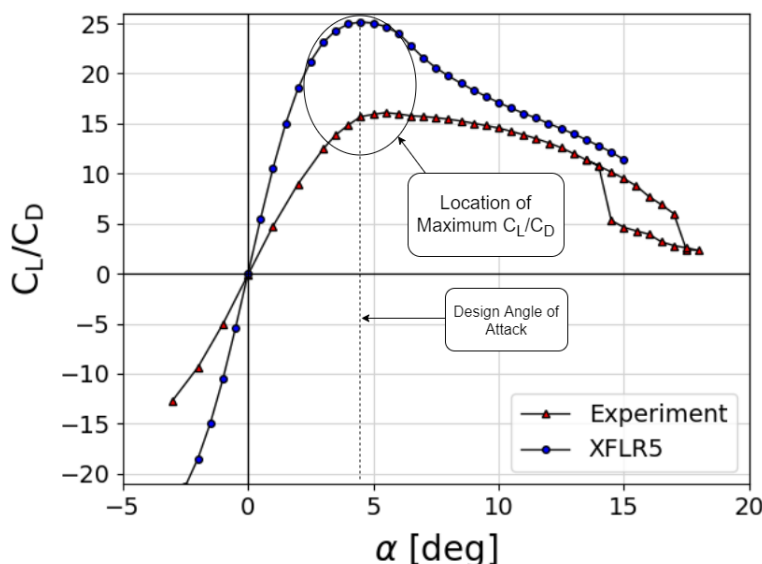


Figure 5.25: Experimental and simulation results of C_L/C_D ratio plotted for different angles of attack at $V = 51.9$ m/s

When looking at Figure 5.25 it is notable that XFLR5 overestimates $\frac{C_L}{C_D}$ for every angle of attack. This is to be expected, seen that the software underestimates drag. XFLR5 does not take viscous effects into account which largely implies a lower drag estimation, as explained on subsection 5.2.2.

Some similarities between the theoretical and experimental results can be drawn from the plot, namely the location of $\left(\frac{C_L}{C_D}\right)_{MAX}$. As shown above, both results roughly indicate the same location for the design angle of attack (the angle of attack at which the C_L/C_D is highest, as that is when the wing is most efficient) of close to 5° . Moreover, both plots go through the origin, which again is to be expected seen that both analysis were performed on a symmetrical airfoil.

The simulation is also unable to model the $\frac{C_L}{C_D}$ ratio around the hysteresis phase due to the absence of flow separation, attributed to the fact that XFLR5 does not include viscous effects in its analysis. As it can be seen from the experimental data, for the same value of angle of attack, at the hysteresis loop, there are distinct values for $\frac{C_L}{C_D}$. This can be attributed to the fact that during the reconnection phase the flow has not yet been able to reattach to the contour of the airfoil, thus leading to a lower value of C_L for angles of attack around that region.

The difference in slopes for the experimental and XFLR5 data, between -3° and 3° , can be explained when looking at Figure 5.15 and Figure 5.23. It can be seen that the C_D for XFLR5 is approximately 50% lower than the experimental C_D between -3° and 3° . Furthermore, the C_L for XFLR5 is slightly higher than the experimental C_L . The lower C_L and the higher C_D of the XFLR5 data results in a steeper slope.

Overall, XFLR5 is really optimistic when evaluating $\frac{C_L}{C_D}$. This was evaluated above and attributed mostly to the fact that XFLR5 does not take viscous effects into account. Nonetheless, some major key point can still be drawn from the simulation, namely the design angle of attack and $\frac{C_L}{C_D}$ at zero angle of attack.

5.2.5 C_M vs α Polar

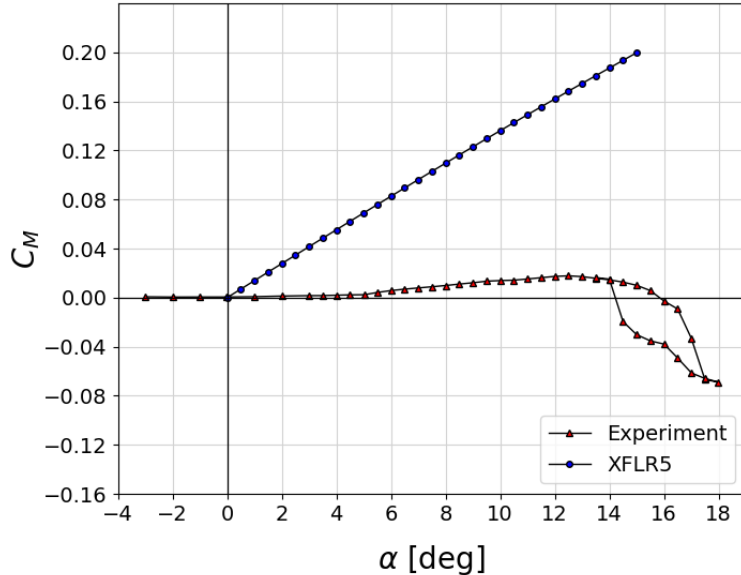


Figure 5.26: The moment coefficient, C_M , plotted against the Angle of Attack, α , at $V = 51.9$ m/s

The final polar to be examined for the three dimensional wing geometry is one which plots the so-called "moment coefficient" against the angle of attack. This is shown in figure 5.26. This plot is useful, as it shines light on the stability properties of the wing, which in turn may impact the design of other aircraft subsystems.

The analysis of this polar will follow the same structure as the other polars that came previously: the graph will be sectioned into ranges of angle of attack where important observations can be made. Every graph section will then be analyzed in great detail in order to draw meaningful conclusions about the validity of the XFLR5 software.

From 0°to 12°

Between 0°and 12°it may be easily noticed that the XFLR5 simulated estimations of the wing moment coefficient differ immensely from the obtained experimental results. In fact, by the time an angle of attack of 12°is attained, the simulation overestimates the wing moment coefficient to be 10 times larger than the actual value. Such large margin of error is in stark contrast to the two dimensional analysis, in which the simulation approximates the experimental data fairly well. There are a number of potential causes for this, and each of them must be taken into special consideration.

One of the likely root causes for the large sources of error between the simulated results and the actual results is viscous effects. Throughout the course of the three dimensional analysis, it has already become evident that viscous effects is a large source of error for many of the previous polars. And for moment coefficients, this proves to have an enormous effect, as is explained in Section 5.4.2. XFLR5 is well capable of estimating viscous effects for a two dimensional airfoil, when calculating the moment coefficient as a function of the angle of attack. However, this is not the case for three dimensional wings, as it will be seen in Section 5.4.2. This critical error is likely responsible for the large margins of error between the experimental and theoretical results as shown in Figure 5.26.

Another potential cause for error (although much more unlikely) is that the inertial properties of the wing (more specifically, the centre of gravity location along the chord line), may have been determined incorrectly. When calculating the moment coefficient for a three dimensional wing system, the moment due to the lift force is taken to be about the centre of gravity of the wing. Given that the lift itself is acting at the center of pressure of the wing system, the moment arm of the lift force is thus given to be the distance between the center of gravity and center of pressure of the wing. As a result, by altering the centre of gravity of the wing, the magnitude and direction of the resulting moment due to lift can be dramatically effected, thus leading to large variations in subsequent moment coefficients.

In order to illustrate the importance of the wing center of gravity location, the following figure shows the experimental data once again, but with three simulated XFLR5 curves. One curve takes the center of gravity (denoted in the graphs and further text as x_{cg} location to be the centroid of the wing (denoted as "C" in Figure 5.27, note that this is also the XFLR5 curve in Figure 5.26), another takes the x_{cg} to be the wing leading edge (denoted as "LE" in Figure 5.27), and the last one assumes a x_{cg} to be at the quarter chord point of the wing (denoted as "1/4c" in Figure 5.27). Figures 5.28, 5.30 show some screenshots of the XFLR5 simulation for the varying locations of the center of gravity.

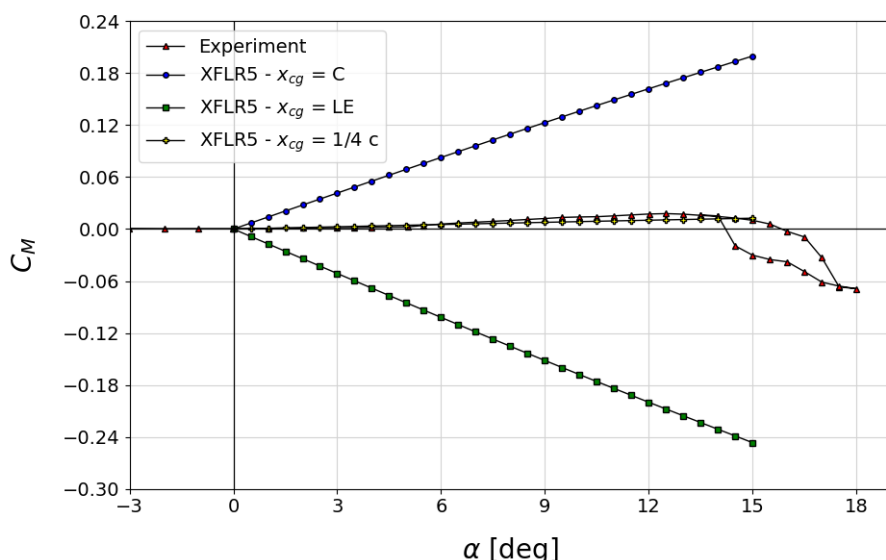


Figure 5.27: Variation in Moment Coefficients, C_M due to Variation in x_{cg} location

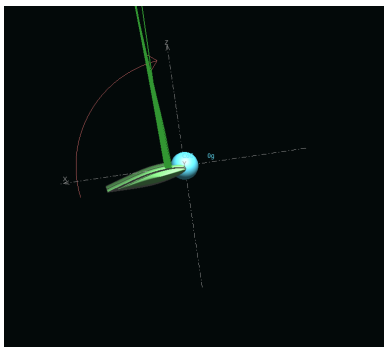


Figure 5.28: XFLR5 Simulation of Lift for x_{cg} at Leading Edge

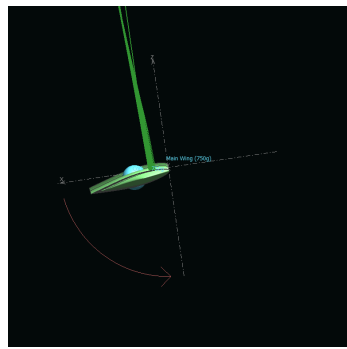


Figure 5.29: XFLR5 Simulation of Lift for x_{cg} at centroid

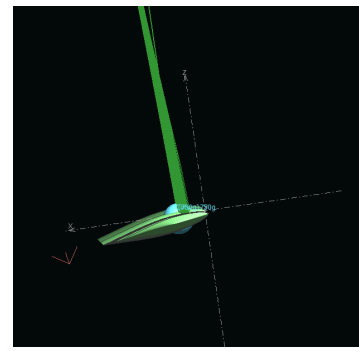


Figure 5.30: XFLR5 Simulation of Lift for x_{cg} at Quarter-Chord Point

As it can be seen in these figures, the change in center of gravity leads to enormous changes in results. When the center of gravity (denoted as the turquoise sphere in the screenshots) is taken at the leading edge, the lift (denoted as the green vertical line) causes a pitch down moment, leading to a negative sloped curve in Figure 5.27. The reverse occurs when the center of gravity is taken at the centroid of the wing box, leading to a high positive slope. When the center of gravity is taken at the quarter-chord point, the moment arm is very small, leading to moments and moment coefficients which are close to zero. However, for the green curve in particular, it can be seen that it agrees mostly with the experimental results with the exception of hysteresis effects at large angles of attack. The goal of these screenshots and figures was to show the impact of the center of gravity location on the calculation of the moment coefficients. However, despite this, it is still deemed unlikely for this to be a leading cause for error. For the purpose of the simulation, assuming the centre of gravity to be at the centroid is deemed to be an acceptable approximation. This is because it was assumed that the model is solid (ie, not hollow) and that a uniform material is used. This was confirmed (or at least in part) by visual inspection of the model prior to starting. XFLR5 is capable of automatically determining the centroid of an airfoil shape, and the results seemed to be logical. Despite this, it is good to keep this in mind given how influential this factor may be in the event of error.

In short summary, there are two main possible factors which may account for the large deviations between the software modelling estimates and the actual results for the wing moment coefficient: incorrect viscous modelling and incorrect wing inertia properties. It is highly likely that a combination of these two factors lead to the errors noticed in 5.26, with the viscous effects being the main cause.

From 12° to 18°

Towards the right side of this graph, the deviations between the simulated and actual results continue to be evident. However, an interesting phenomena occurs, in which the experimental data begins to sharply fall. In the simulated results, this sharp drop-off is not modelled, and the wing moment coefficients continue to follow a linear trend. In order to understand the reasoning behind this large difference, one must consider the limitations of the XFLR5 analysis, in particular the neglect of viscous phenomena. As was discussed previously, the lack of consideration of viscosity does not allow the data of the wing to be modelled realistically at all angles of attack, but even more so at high ones where flow separation and hysteresis become the predominant effects that drive the results of the moment coefficient. As can be seen in Figure 5.26, the experimental results fall off after an angle of 12° where a maximum in the pitching moment coefficient is reached. After this point there is an increment in the decreasing behaviour of the coefficient demonstrated by the more negative slope of the curve, which is due to flow separation causing the pressure resultant to act more towards the back of the airfoil, where speeds are increased, causing a pitch down moment. This is mainly due to the lift-generating geometry of the airfoil being lost when flow separation occurs, and the forces act in an undesired direction. In order to reattach the flow, it can be seen that the angle of attack was needed to be reduced to around 14 °, forming the clear hysteresis loop that can be appreciated in Figure 5.26.

5.2.6 Conclusion on the Wing Analysis

Throughout the entirety of this section, the aerodynamic properties of the finite wing were analyzed through the use of XFLR5 simulating tools as well as wind tunnel experimental results. These results were plotted in the figures shown in Subsections 5.2.1, 5.2.2, 5.2.3, 5.2.4, 5.2.5 and a subsequent explanation of results was presented for each. After having done this, it is reasonable to conclude that XFLR5 can plot the wing aerodynamic properties with reasonable accuracy. However, throughout all plots there was a certain degree of error. This is largely due to errors which were made when certain flow phenomena was either neglected or approximated poorly.

These flow phenomena are more specifically the approximation of the boundary layer, stall behaviour and the drag effects of tip vortices, leading to overly optimistic values for lift and drag coefficients. Furthermore, the effect of the flow viscosity on the stability of the three dimensional wing is also completely neglected, leading to large margins of error.

In the following Section, further details about the flow phenomena will be explained as well as further rationale for why the XFLR5 simulation may have been incorrect in its approximations of certain aerodynamic constants.

5.3 Flow Phenomena

In this section, the various flow phenomena observed in the measurements and pictures are described. First subsection 5.3.1 will present a discussion of the Laminar Separation Bubble that was frequently mentioned in earlier sections. Then, the phenomenon of hysteresis will be further explained in subsection 5.3.2. The tip vortices and their effect on the finite wing performance will be addressed in subsection 5.3.3.

5.3.1 Laminar Separation Bubble

This flow phenomena has a huge impact on the different polars when it comes to larger angles of attack. For lower angles of attack the boundary layer is predominantly laminar and the flow is laminar as is indicated in Figure 5.31. In previous sections, the LSB was only mentioned as its topic is quite complex and clearly present in both the infinite and finite wing analysis. However, a more detailed description of this phenomenon is given in this section. The laminar separation bubble is, as the name indicates, a bubble that is present when the adverse pressure gradient cannot be overcome by the laminar flow anymore. This comes from the fact that the momentum of the flow is not high enough to stay at the surface, it therefore separates. However, it can reattach later on to the airfoil/wing and a 'bubble' is formed as can be seen from Figure 5.32.

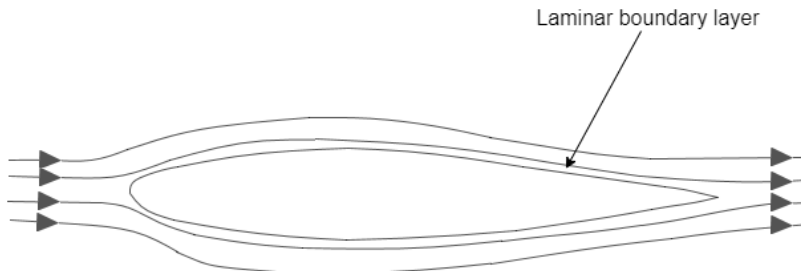


Figure 5.31: Sketch of laminar flow around an airfoil at lower angles of attack.

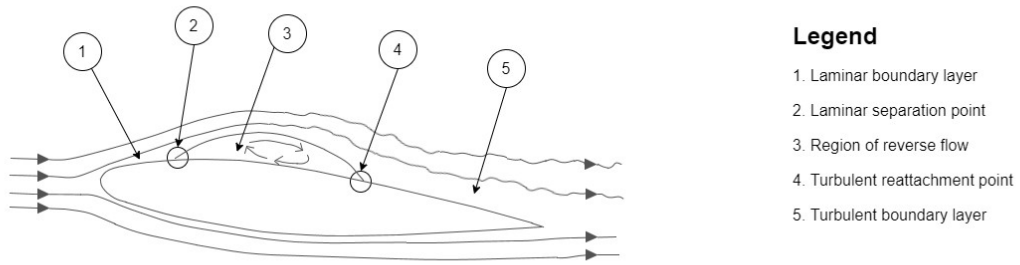


Figure 5.32: Sketch of flow around an airfoil with a laminar separation bubble [Own work]

As can be seen on the Figure 5.32, the flow is turbulent behind the laminar separation bubble. Inside the bubble, all the properties of 'common' separation can be found such as large viscous effects and a region of reversed flow. This is sketched in Figure 5.33.

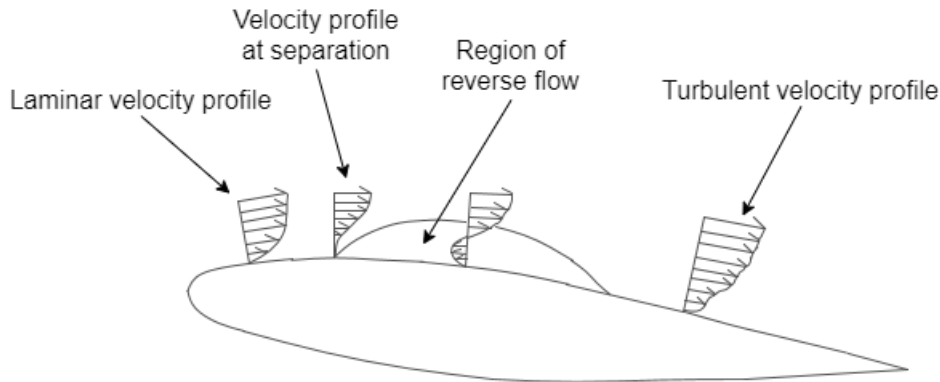


Figure 5.33: Sketch of the velocity profile of the airflow at multiple over an airfoil in the presence of a laminar separation bubble [Own work]

After there has been a turbulent boundary layer initiated, at higher angles of attack this turbulent boundary layer will separate and turbulent separation will occur on the airfoil/wing. As mentioned in the wing and airfoil analysis (see Subsections 5.1.2 and 5.2.1), this turbulent separation can be visualised by the tufts attached to the airfoil/wing. This turbulent separation together with the LSB will cause the airfoil/wing to stall together.

When stall is reached the LSB will burst, either because the turbulent separation reached the bubble located at the trailing edge or simply because reattachment is not possible anymore. This burst will cause a region of reversed flow over the airfoil which dramatically increases the drag, reduces the lift and shifts the centre of pressure in front of the aerodynamic chord ($0.25 \times c$). This is really dangerous as could be inspected in Sections 5.1 and 5.2. The separated flow and region of reversed flow over the airfoil can also be found in Figure 5.34, which happens at large angles of attack. This figure shows complete separation at an AoA of about 15.5° for the finite wing and 15° for the airfoil.

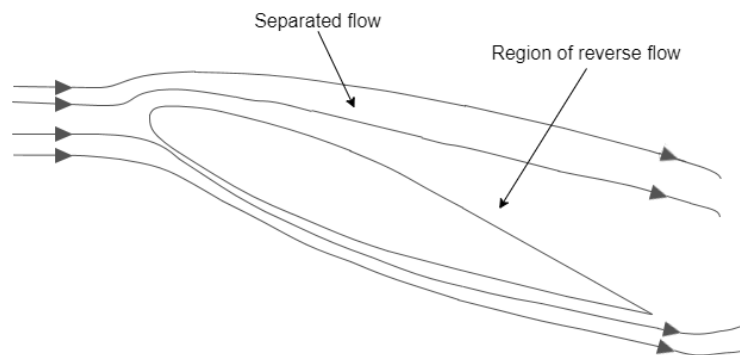


Figure 5.34: Sketch of a stalled airfoil [Own work]

It is interesting to note that the LSB can actually be seen using the infrared images before its burst. For illustration purposes, such images for the finite wing are given in Figure 5.35. On Figure 5.35a, the LSB is seen from the darker line present at the LE along the entire span. Though, a few angles of attack further, Figure 5.35b has no sign of the bubble while the drag immensely increased and the lift dropped (see Figures 5.23 and 5.15)

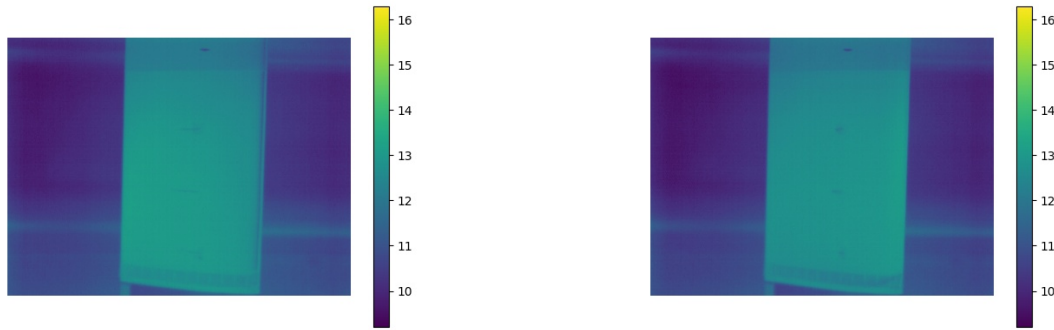
(a) LSB before burst (15.5° AoA)(b) After LSB burst (17.5° AoA)

Figure 5.35: Visualisation of the LSB on infrared images

5.3.2 Hysteresis

Many references have been made with regards to the hysteresis loops that have formed continuously in all the experimental data that was collected. This is due to it being an important phenomena that plagues any wing in a 2D or 3D scenario. Hysteresis can be defined as the dependence of a system with its history, and this is precisely what occurs in aerodynamic analysis once stall occurs.[1]

Once flow separates from the top surface of the wing due to large adverse pressure gradients, a sharp change in the aerodynamic properties of either the wing or airfoil occurs. This change is often for the worse, as was explained previously throughout chapter 5, in the form of reduced lift or increased drag. After this variation, a large decrease is required in the angle of attack in order to attach the flow once again to the surface of the airfoil to return its benign aerodynamic properties. This effect can be witnessed in all of the experimental curves of the graphs of the previous sections. However, it cannot be found in any simulation results due to hysteresis being an effect that has to do with laminar boundary layer separation and transition, which are viscous effects.[23]

Additionally, an important analysis on the effects that hysteresis has on flow phenomena can be made through the thermal analysis on the upper surface of the wing. Observing Figure 5.36a and Figure 5.36b, it can be seen that the detached flow in the hysteresis loop (meaning in the process of reducing the angle of attack to reattach the flow) has higher and more homogeneous temperatures (and velocities thereof) in comparison to the attached flow situation. This means that there is a more or less uniform pressure distribution in detached flow with an overall lower lift than in the case of the attached flow, where it can be seen that low velocities are reached at the leading edge due to the flow following the contour of the airfoil. Effectively, this uniform pressure distribution causes a lower lift coefficient and higher drag coefficient at a given angle of attack within a hysteresis loop when reducing the angle after stall.

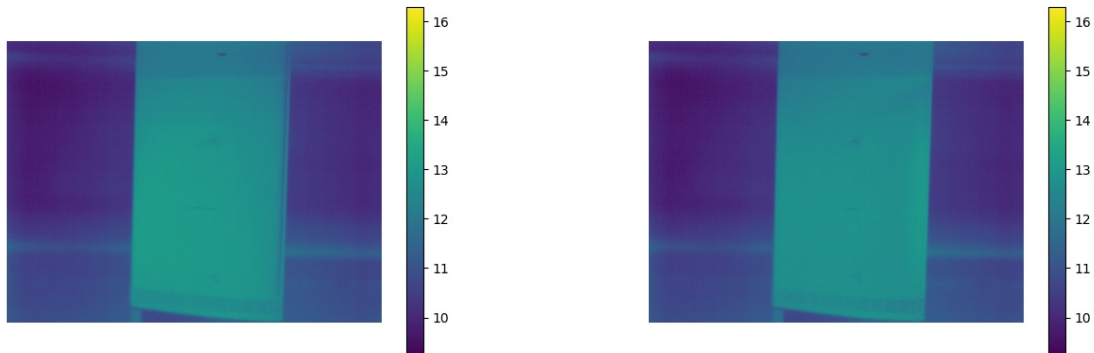
(a) Heat map for attached flow at 16.5° (b) Heat map for detached flow in hysteresis loop at 16.5°

Figure 5.36: Infrared picture hysteresis analysis

5.3.3 Tip vortices

Throughout the entirety of the report, there has been a lot of references to "tip vortices" as being a phenomena which accounts for certain anomalies which occur with the two dimensional and three dimensional polars. The subject of this subsection is to describe the physical meaning of tip vortices and what effect this has on flight performance of finite wings. This will become useful particularly in Section 5.4 in which the two dimensional and three dimensional polars are compared against each other.

Tip vortices is a phenomena which occurs specifically with three dimensional finite wings. Whenever a finite wing is travelling through air, a pressure differential is created between the upper and lower surfaces of the wing. However, by the wing tip, this pressure differential must equalize. [24] As a result of this, air will generally travel around the wing tip from the lower surface to the upper one. This will cause a circular motion within the flow, known as "tip vortices". In XFLR5, "tip vortices" are simulated in the form of "vortex sheet roll-up", in which the streamlines take on a circular trajectory after having passed over the wing tips. [1] This is clearly represented in Figure 5.37.

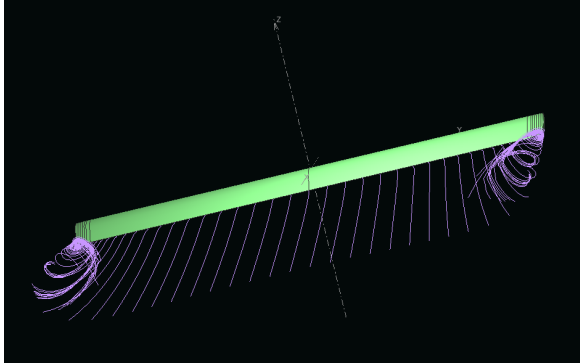


Figure 5.37: XFLR5 representation of tip vortices affecting the lift performance of three dimensional finite wings

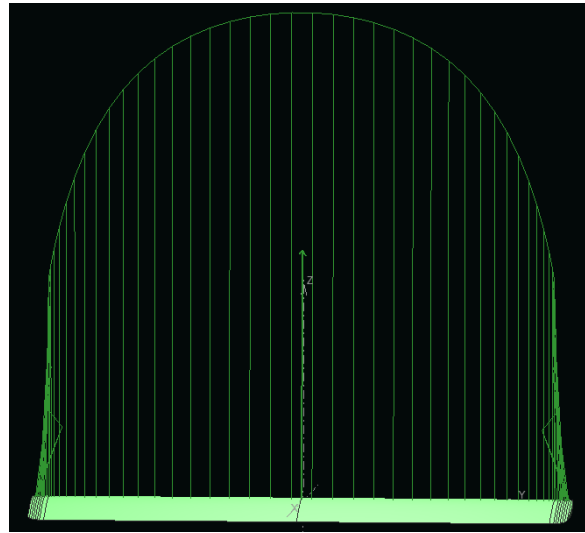


Figure 5.38: Lift Distribution of a Finite Wing

Tip vortices are an unavoidable flight phenomena. However, its effects are generally adverse, as it reduces a wing's lifting performance in a number of ways. Firstly, because the pressure must equalize at the wing tips, the lift distribution across the span of a three dimensional wing cannot be uniform (such as in a two dimensional airfoil case). Instead, it must follow a quasi elliptical distribution, such as the one shown in Figure 5.38. As a result of this, naturally the two dimensional airfoil will produce more lift than the three dimensional wing at the same angle of attack. This becomes more and more significant as the generated lift increases, as a larger pressure difference must be equalized by the time the wing tip is reached.

In addition to the change in lift distribution which is created by the fundamental principles of fluids, there is another adverse affect created *specifically* by the tip vortices. Whenever air passes over the wing tip, the circular motion of the tip vortices creates a so-called "downwash". [25] The downwash is a component of the airfoil which is directed perpendicular to the motion of the wing (thus, downwards in most cases). This downwash component is non-zero at the location of the wing, or simply put, the wing has to fly through its own downwash.[24] The downwash adds a downwards component to the oncoming flow. This results in two aerodynamic phenomena. First, the angle of attack of the wing is reduced, leading to a lower amount of lift generated. This is clearly shown in Figure 5.39, in which the nominal angle of attack. The equation describing the reduction in lift coefficient is given below:

$$C_L = \frac{C_{L0}}{1 + \frac{C_{L0}}{\pi \cdot AR}} \quad (5.3)$$

In which C_L is the lift coefficient with induced Angle of Attack, C_{L0} is the lift coefficient without the induced Angle of Attack, and the Aspect ratio is a fundamental geometric constant pertaining to the wing's slender-

ness.[25] The difference between C_{L0} and C_L is thus given as follows:

$$\Delta C_L = C_{L0} - \frac{C_{L0}}{1 + \frac{C_{L0}}{\pi \cdot AR}} \quad (5.4)$$

Plotting this will show that the difference between the two lift coefficient values will increase linearly as the angle of attack is increased. This is exactly what is observed in graph 5.40.

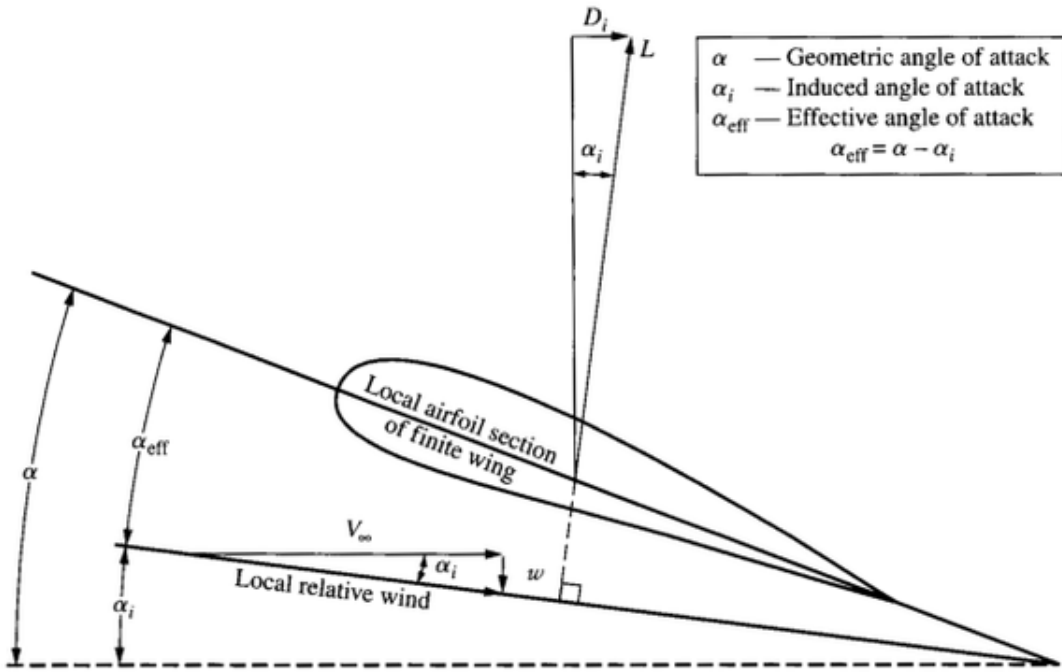


Figure 5.39: Depiction of the Angle of Attack Reduction due to Tip Vortices, source: [24]

The second aerodynamic result from tip vortices is that the induced drag is increased due to the downwards airflow. [25] This is governed according to the following equation:

$$C_{di} = \frac{(C_L)^2}{\pi \cdot AR \cdot e} \quad (5.5)$$

In which C_{di} is the induced drag coefficient and e is the "Oswald efficiency factor" which is a measure of the shape of the wing lift distribution. The remaining variables are declared as before. As it can be seen, the induced drag increases parabolically with lift. As a result, the three dimensional wing will not exhibit any sort of drag bucket nature, like in the two dimensional case. This will become very noticeable when comparing two dimensional and three dimensional results in subsection 5.4.1, especially when looking at graph 5.44.

In short summary, tip vortices are an unavoidable phenomena which occurs during flight because of the laws of nature governing fluid flow. However, although unavoidable, continuous efforts are being made to reduce its effects, such as adding wing lets (which increases Aspect ratio and thus increases lift coefficient and decreases induced drag) and other devices to the wing. The effects of such devices in practice is beyond the scope of this report, but would be an interesting topic to investigate in the future.

5.4 Further Analysis

In this section, some further investigations are made concerning a few topics. Namely, a comparison between the case of an airfoil and a 3D wing (subsection 5.4.1), a discussion of the viscous and inviscid simulation of XFLR5 (subsection 5.4.2) and the transition position of the flow for different Reynolds numbers (subsection 5.4.3).

5.4.1 Comparison between 2D and 3D Wing

Throughout the vast majority of this chapter, lots of attention was given to assessing the validity of the XFLR5 software compared to actual results. However, very little emphasis was given to the differences which exist between the experimental results of the two dimensional "infinite" and three dimensional "finite" wing sections. This will be the subject of this subsection.

Throughout the examination of the XFLR5 and experimental results, there were a number of polars which were present in both the 2D and 3D analysis. These were the lift coefficient, drag coefficient and moment coefficient vs. angle of attack polars, as well as the lift coefficient vs. drag coefficient and lift coefficient over drag coefficient vs. angle of attack polars. The experimental results from these polars will be replotted once again against each other, so that discrepancies may be highlighted and examined. These are shown in the figures below.

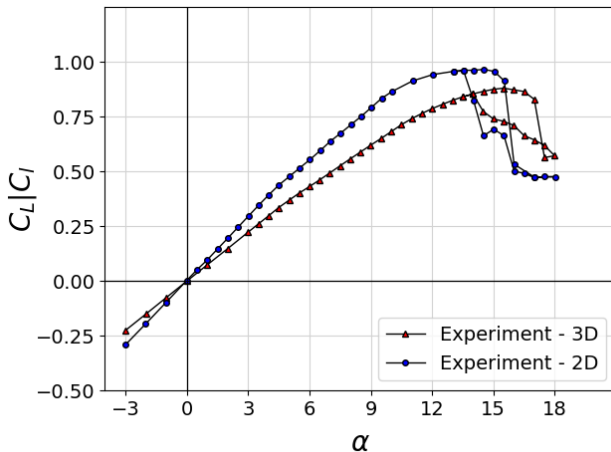


Figure 5.40: Lift Coefficient, C_L versus Angle of Attack, α for 2D and 3D Experiments

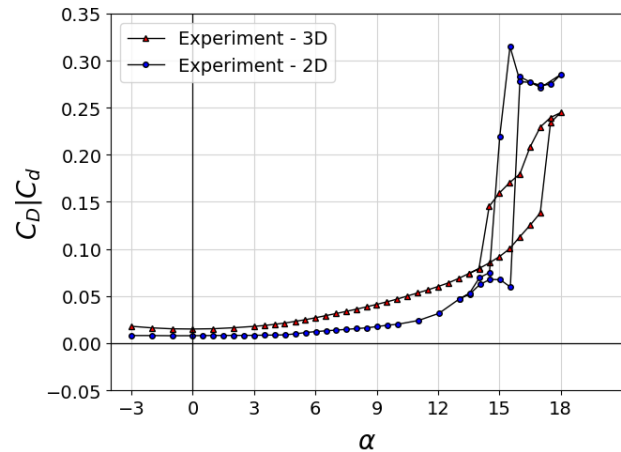


Figure 5.41: Drag Coefficient, C_D versus Angle of Attack, α for 2D and 3D Experiments

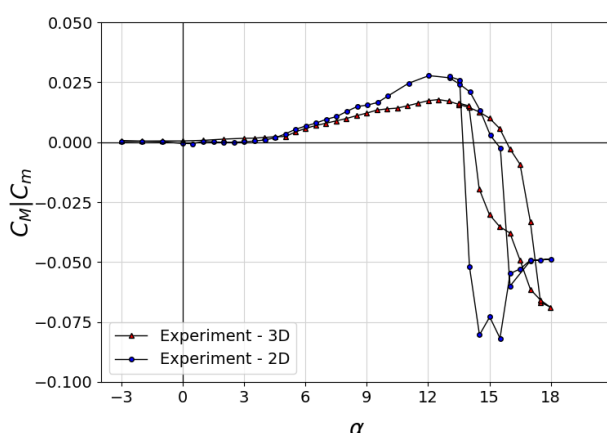


Figure 5.42: Moment Coefficient, C_M versus Angle of Attack, α for 2D and 3D Experiments

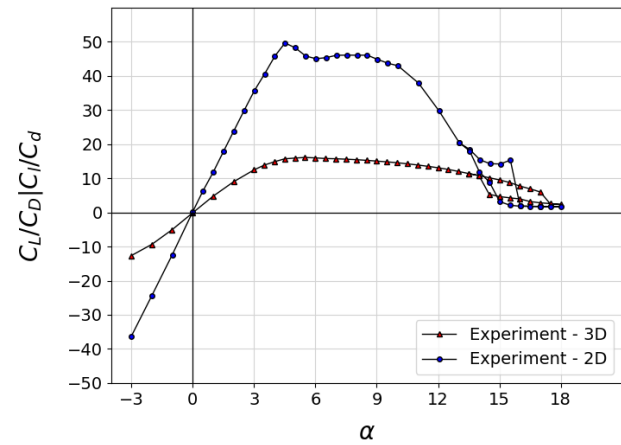


Figure 5.43: Lift to Drag Ratio, $\frac{C_L}{C_D}$ versus Angle of Attack, α for 2D and 3D Experiments

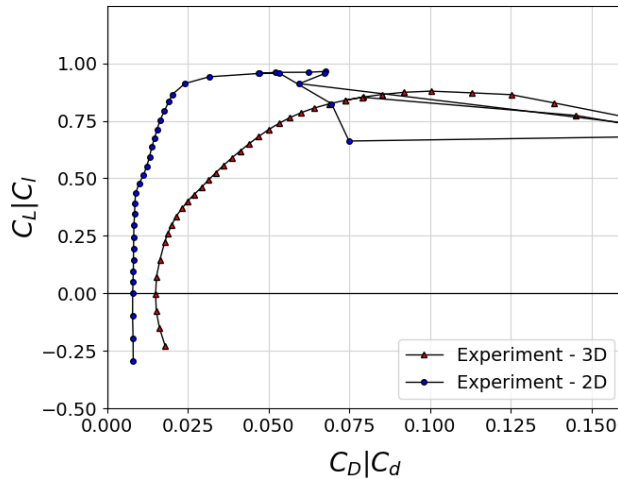


Figure 5.44: Lift Coefficient, C_M versus Drag Coefficient, C_D for 2D and 3D Experiments

Upon examining these graphs, it may be noticed that there are small deviations which lie between the two and three dimensional analysis. In general, it is found that the two dimensional "infinite" wing produces more lift and lower drag at the same angles of attack. The result of this is that the lift to drag ratio of the infinite wing is significantly larger than the three dimensional "finite wing". In short, the two dimensional wing is more efficient. However, because the three dimensional wing produces less lift, it is found that the finite wing is more stable (in essence, smaller positive moment coefficients). This is beneficial when designing other aircraft subsystems.

The root causes for the differences between the two and three dimensional wing analysis are very similar to the ones already discussed when evaluating the validity of the XFLR5 software: the change in lift distribution and the effect of tip vortices. Both of these will be discussed briefly here. However, for more in depth about the subject, the reader is encouraged to proceed to subsection 5.3.3.

The change in lift distribution is an important factor to consider when analysing the discrepancies between 2D and 3D analysis. In a two dimensional analysis, the lift distribution is considered to be uniform along the span of the "infinite wing". This is because the airfoil geometry does not change at all throughout the entire span. However, this is not the case for a finite wing, as much less lift is produced at the wing tip, partially due to the smaller chord length and partially due to tip vortices (see next paragraph). A result of this is that the wing produces less lift at lower angles of attack, which is what is observed in the graphs. The difference between a uniform and a varying lift distribution becomes increasingly large with increasing lift, which therefore accounts for the increasing gaps which can be seen in most trend lines in the graphs.

The effect of tip vortices also plays a key role in the difference between infinite wings and finite wings. As explained in Subsection 5.3.3, high pressure flow from below the wing tends to curl around the wing tip towards the low pressure flow on the top side of the wing. The result of this is that the effective angle of attack is reduced, and the flow loses kinetic energy, leading to a higher induced drag. Such phenomena never occur in infinite wings, as there are no wing tips. This effect becomes increasingly prominent the higher the lift produced is, as the difference in pressure between the upper and lower surfaces of the wing (in essence, lift), dictates the intensity of the tip vortices. As a result, this explains why in figures 5.40, 5.41, 5.44, it can be seen that the difference in lift and drag between the two and three dimensional wing becomes increasingly large. The increase in induced drag and the decrease in lift become more prominent. And so, the three dimensional wing becomes less and less efficient.

As a final concluding element to the comparison between the two and three dimensional wing analysis, it is important to analyze the stall conditions in both cases. As it can be seen, the stall behaviour of both wing geometries are fairly similar, with C_L and C_D values being fairly close. However, upon closer examination, in Figure 5.40 it can also be seen that the hysteresis cycle for the two dimensional airfoil surface tends to be far more abrupt than for the finite wing. This could perhaps be explained by the effect of wing vortices, which due to their downward motion could in fact push the air back towards the surface of the wing and thus delaying and

reducing the effect of the separated flow on stall recovery. Furthermore, a more attached flow would recover the beneficial geometry of the airfoil, which allows for improved lift geometry. Nevertheless, this point is simply a result of speculation.

5.4.2 Comparison of Viscous and Inviscid Simulation in XFLR5

In this section, the numerical analysis used is put into perspective by comparing its viscous and inviscid version as this shows the effect of the theory used by XFLR5. Figure 5.45 shows the $C_l - \alpha$, $C_d - \alpha$ and $C_m - \alpha$ curves for the inviscid and viscous analysis of the NACA 64₂A – 015.

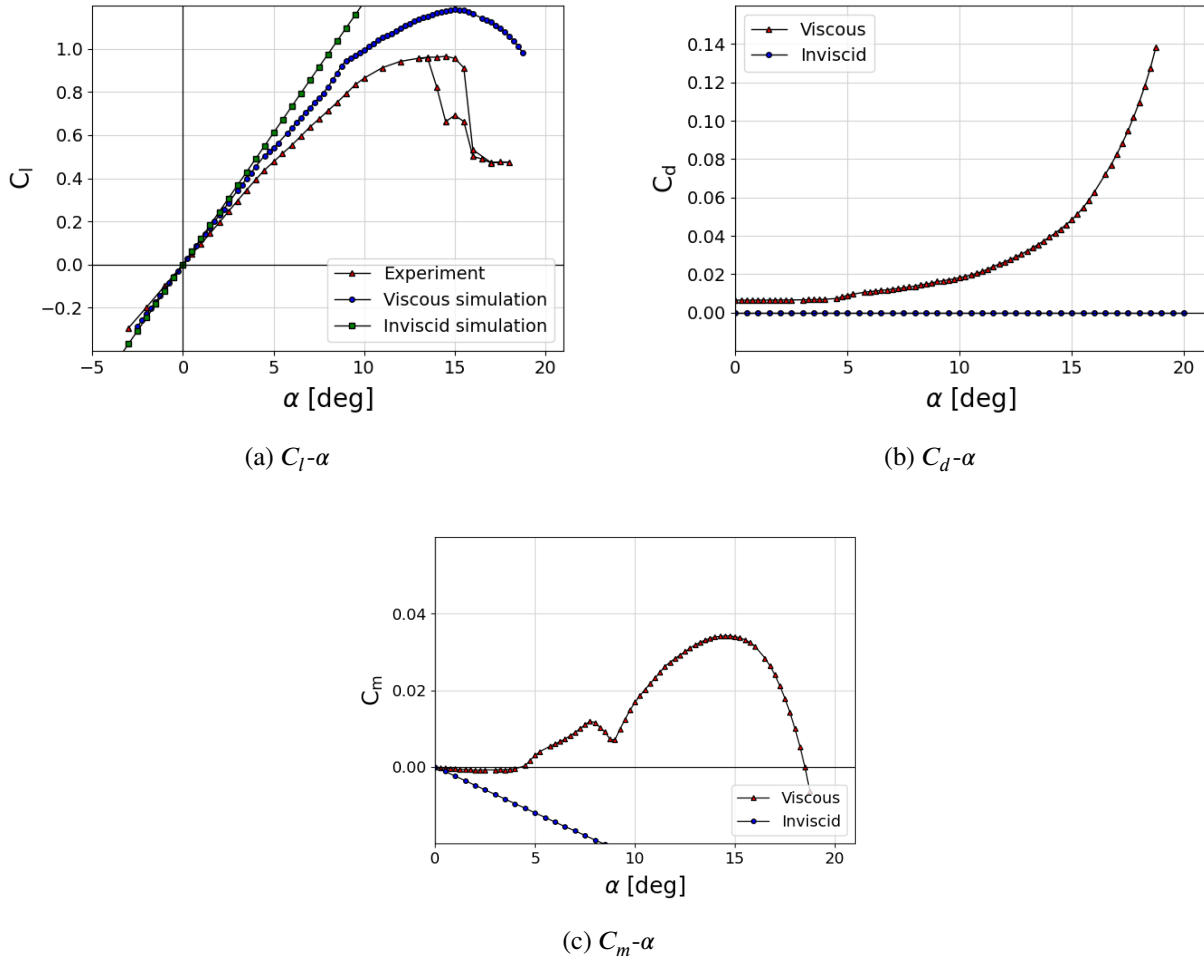


Figure 5.45: Graphs showing the comparison between viscous and inviscid simulation methods for the NACA 64₂A – 015. The viscous analysis was performed at $\text{Re} = 860000$.

Figure 5.45a presents the inviscid and viscous versions of the simulation performed for the lift curve. The error of the viscous lift slope was presented in subsection 5.1.2, though a similar analysis can be made using the inviscid numerical solution. From Figure 5.45a, the slope of the squared curve is found to be 2.22π which can be compared to the value of 1.78π found from the experimental data. This yields an error of $\frac{\text{numerical-experimental}}{\text{experimental}} = 24.6\%$, against 16.6% for its viscous counterpart.

D'Alembert's paradox [6], which states that the drag of an object is zero according to potential flow theory, is very well shown in Figure 5.45b. Indeed, this theory is used by XFLR5 for the inviscid simulation and the paradox is clearly seen on the blue curve. Therefore, for the airfoil analysis, it is seen that the entirety of the drag taken into account by XFLR5 is of viscous form and exponentially increases with the angle of attack.

Next, Figure 5.45c presents the inviscid and viscous versions of the simulation performed for the two dimensional airfoil analysis for the moment coefficient. As can be easily noticed the two are sensibly different, and this was already previously encountered in subsection 5.2.5, Figure 5.26. The results from the viscous analysis yield

results that resemble much like the experiment results. However, the inviscid analysis is not even close, leading to a linear trend which resembles the trend line which can be seen in the Figure 5.26 (albeit with a different slope). The goal of the following paragraphs will be to explain why the numerical and experimental results may be so different. In order to calculate the moment coefficient of an airfoil, the following equation is used:

$$C_m = \frac{M}{\frac{1}{2} \cdot \rho \cdot V \cdot c^2} \quad (5.6)$$

In which M is the moment generated by the lift force. This moment is taken about the leading edge of the airfoil, and the lift is said to be acting at its centre of pressure (thus the lift moment arm is the center of pressure location minus the leading edge)[26]. ρ is the air density at the considered altitude, V is the airspeed and c is the chord length. Now, for a three dimensional wing, the moments are taken about the centre of gravity (which can be adjusted, thus leading to a change in moment arm as discussed in subsection 5.2.5) and the denominator term c^2 is transformed to $S \cdot c$ where S is the wing surface area[27]. But the principle itself is the same. In the inviscid analysis, this equation is used for both 2D and 3D analysis. As a result, when the lift (and corresponding lift coefficient) increases, the generated moment is increased, thus leading to an increased moment coefficient. This variation in moment coefficient occurs linearly with lift coefficient, which explains why inviscid analysis (both in 2D and 3D) lead to linear trend lines. Depending on whether the moment generates a pitch up (positive) or pitch down (negative) moment, the slope of the linear trend will differ. A positive pitch up leads to longitudinal instability (as an increase in angle of attack or pitch up motion will lead to an increase in lift and moment) whereas the negative pitch leads to longitudinal stability (as an increase in angle of attack or pitch up motion will lead to an increase in lift, but a decrease in moment).

Whenever viscosity is introduced to the stability analysis, it becomes much more complex, as this alters the lift distribution and drag distribution which in turn impacts the moment distribution as well. And although the physical reasons for how this impacts the moment coefficient is beyond the scope of the report, the results from the 2D inviscid and viscous results shine some light on what exactly is happening. Contrarily to the inviscid analysis, the trend is no longer linear and it is much closer to zero. This suggests that viscosity reduces the moment arm between the center of pressure and where the moments are taken about. Furthermore, the viscosity makes the flow about the wing inherently more unstable, leading to a positively trending moment coefficient. Because the differences between inviscid and viscous analysis are so large, an accurate model for viscous flow is necessary. This is available for two dimensional analysis, but not for three dimensional ones.

As mentioned numerous times previously, XFLR5 uses interpolated results from a two dimensional analysis in order to predict the viscous effects occurring on a two dimensional wing[28]. However, this is very much prone to error, and that continues to be the case here. Figure 5.46 below illustrates the viscous vs. inviscid modelling for the three dimensional wing moment coefficients. As it can be seen, there is absolutely no difference, apart from the viscous modelling ending slightly earlier (likely an interpolation error due to stall behaviour). This similarity between the curves is in clear contrast to the two dimensional plots shown in Figure 5.45, and is thus a clear red-flag that something has gone wrong. As a result, this illustrates a clear limitation of XFLR5 when modelling moment coefficients.

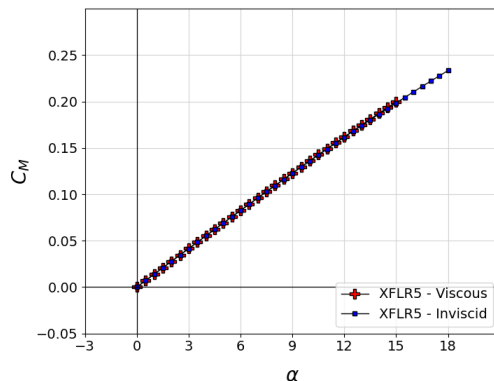


Figure 5.46: Graphs showing the comparison between viscous and inviscid simulation methods for three dimensional finite wings. The viscous analysis was performed at $Re = 860000$

5.4.3 Transition Position from XFLR5

In this subsection, the transition position from a laminar to turbulent flow on the airfoil using the XFLR5 simulation will be discussed. This will be done at an angle of attack of 0° and will be compared to the thermal images available. This will be done for a critical Reynolds's number of 500 000 and 1 000 000. A value of the friction coefficient C_f will also be determined from XFLR5 for those two flow conditions.

The transition position can easily be seen from the pressure graphs as given in Figure 5.47. The transition between laminar and turbulent flow is located at the sudden drop in pressure (as was seen previously in section 5.1) and therefore, the location of the transition is at 0.6935 and 0.6490 x/c for Reynolds's numbers of 500 000 and 1 000 000 respectively. This can easily be seen in the graphs, the transition position occurs where a drop (adverse gradient) in C_p is seen.

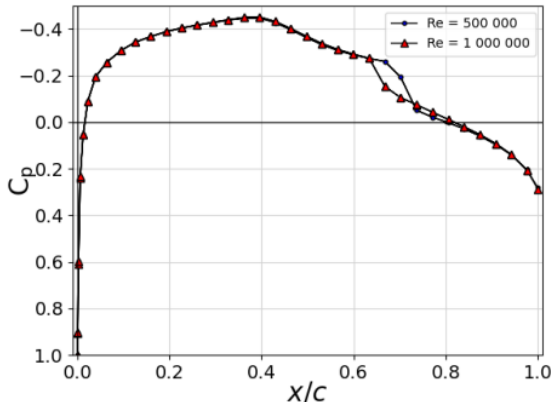


Figure 5.47: Pressure distribution on the NACA

64₂ - 015 at 0° AoA for $Re = 500\ 000$ and $Re = 1\ 000\ 000$

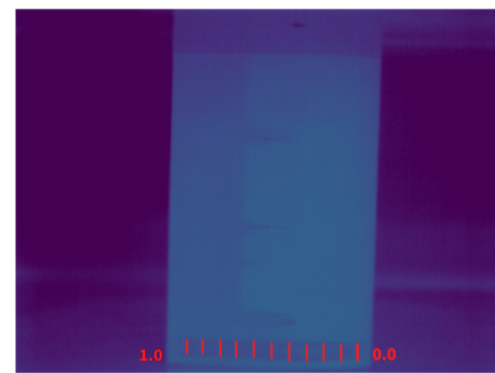


Figure 5.48: Infrared image of the airfoil at 0° AoA

This confirms that the transition position is moved forward when higher Reynolds numbers are reached and gives rise to less drag in case no separation occurs (as is the case at 0° AoA), this is also illustrated by the friction coefficient C_f (see Figure 5.49). The results obtained for the position of the transition point can be interpolated to have an estimate of this same point for the test conditions: $\frac{0.649 - 0.6935}{\Delta Re} \cdot (860000 - 500000) + 0.6935 = 0.66146x/c$. From Figure 5.48, the transition position is found to be 0.66 x/c. Therefore, even using a linear interpolation, the simulation from XFLR5 is accurate for this purpose.

The skin friction coefficient is also directly given from the analysis on XFLR5 as a function of the position and side (top or bottom) on the airfoil. However, at 0° angle of attack, the state of the flow is exactly the same on the top as on the bottom of a symmetrical airfoil. The graph showing C_f as a function of x/c is given in Figure 5.49.

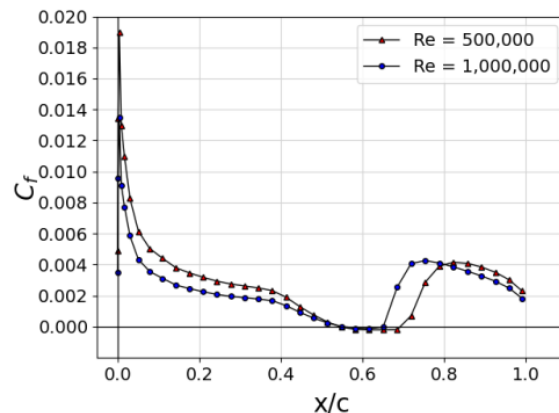


Figure 5.49: Skin friction coefficient as a function of x/c

As can be seen, first a lot of friction is present at the leading edge due to the flow coming to rest at the stagnation

point. Regions a bit behind the leading edge also experience relatively large forms of friction as the flow is mainly deformed at those positions. The coefficient then lowers down to zero as the shape of the airfoil does not deform the flow directly anymore after a position around $0.4 \times c$ (the flow simply follows the shape but does not encounter the object). A spike in C_f then occurs at the transition from a laminar to a turbulent flow at the positions mentioned earlier. Those curves can also be integrated to obtain the total skin friction coefficient of the airfoil in both cases, those are given in Table 5.1.

Table 5.1: Skin friction coefficient

$Re = 500\,000$	$Re = 1\,000\,000$
0.00548	0.00480

Note that the values given above are for the complete airfoil and therefore include the upper and lower surface. Note also that, as expected, the skin friction coefficient is less for higher Reynolds's number although the transition occurs earlier. The reason behind this is easily seen from the area under the graph on Figure 5.49 and is explained by the fact that the Reynolds's number is a measure of how important viscosity is compared to inertial forces. The larger Re is, the less significant viscosity is and thus the less friction there is.

5.5 Comparison Experimental and Numerical Analysis

Both a numerical and experimental analysis were performed to obtain the results presented in this report. In this section, the two approaches are compared to each other to evaluate their pros and cons.

Application of the Methods

In the context of a design, both methods are used at different stages. As the use of a wind tunnel is expensive and those facilities are busy during the complete year which makes them quite hard to access, a simulation software is often (if not always) used first. The purpose of a software such as XFLR5 is not to be fully accurate but to give an idea about the characteristics of the airfoil or the wing. Furthermore, as will be seen below, the numerical method tends to overestimate the performance of the model. This means that in case the simulation software used predicts bad performance, the experimental results would probably give even worse results. Thus a change in the design can be made early on and avoid wasting money and time in real-life testing.

Rapidity of the Results

One of the main advantages of the low-level numerical analysis in comparison to the experimental one is that it is a lot less time consuming. Guidelines are easily found online to perform some analysis and it only takes a few minutes in case handled with expertise. This permits to obtain rapid preliminary results at early design stages. However, even within the numerical analysis domain some software are more developed and provide better results than others. But this is always a trade off between time and accuracy of the results. For instance, a much more accurate program also available is ANSYS but getting very accurate results can take days of processing.

Accuracy of the Results

In order to evaluate the exact performance of the model, an experiment will always outperform any numerical analysis given that the data is processed correctly and that all the measurement devices are calibrated accurately. That is the reason why a simulation will never replace the actual testing of a design. As was seen in both Sections 5.1 and 5.2, the simulations in XFLR5 tend to overestimate the performance of the model such as the lift over drag ratio which predicts a value of 25 for the wing while the experiment shows a result of about ~ 16 (the same kind of observation was made for the airfoil). Another important aspect is the drag created by the wing in the

flow, which is underestimated as was seen in subsection 5.2.3 and again the same type of conclusions can be drawn from the airfoil (see subsection 5.1.4).

In a general manner, due to the simplifications (see chapter 3) made by XFLR5 to provide rapid results, some flow phenomena cannot be described by the software. For instance, the stall behaviour cannot be described as it happens with large viscous effects which are vastly underestimated by the program. Though, for the airfoil, Figure 5.3 shows that XFLR5 found a value for $C_{L_{max}}$ of 1.18 while the experiment gives 0.97 (the comparison was already assessed in the relevant section) but it then draws some sort of approximate stall behaviour. That comes from the fact that some theory is available for 2D viscous flows and is taken into account by XFLR5 (although it is of course far from perfect). In contrast, the simulation for the finite wing does not show any stall behaviour. Another flow phenomena that cannot be described at all by XFLR5 is the hysteresis that was observed in the experimental data.

Those are only a few examples of what was discussed in Section 5.1 and 5.2.

Conclusion on the Comparison

Two important points need to be taken into account when it comes to selecting the method to be used. Those are given in the form of question in the following:

- *How soon must the results be found?*
- *How accurate do the results need to be?*

In case fast and not too accurate results are necessary (as in a preliminary design phase), a simulation using XFLR5 can be used. If more accurate data is preferred but shall still be obtained rapidly, a more advanced software such as ANSYS can be used. Finally, when the exact characteristics of the wing need to be determined (such as for a final design), an experiment *must* be used.

Conclusion and Recommendations

6

The aim of this report was to analyse and compare an airfoil and wing both in a simulation and in the Low Turbulence wind tunnel of the Delft University of Technology. For the wind tunnel experiment the same model was used for the wing measurements as for the airfoil measurements, the only difference was that the table present at the tip chord during the airfoil measurements is replaced by a rounded tip attached to the tip chord. The speed used for the measurements was $\sim 52 \text{ m s}^{-1}$. The measurements were performed with the use of the following equipment:

- Six component force balance
- Electronic pressure Scanner
- Wake pressure rake
- Infrared cameras and heat lamps
- Tufts on the wing

The experimental data obtained with this equipment still needed to be corrected for the following wall corrections; Lift interference, Model blockage and Wake blockage. All of these increased the dynamic pressure over the airfoil as they caused the velocity to increase. This lead to the graphs being corrected for lower dynamic pressure to obtain more realistic values.

For the simulation the software XFLR5 was used for both the airfoil and wing analysis. The polars and pressure coefficient graphs obtained from this program were directly compared with the experimental results. The polars and graphs obtained from the simulation are different than those of the experiment. For lower angles of attack the polars are almost identical, but as the angle of attack increases the difference becomes more and more visible. This happens when the flow became more turbulent and the simulation can not predict turbulent flow accurately enough. This was the same for the airfoil and wing analysis. The most vital finding was that the software is not able to predict the hysteresis. Which again traces back to the software not being able to predict turbulent or chaotic movement well.

Another thing to be noted is the difference in the transition lines for airfoil and wing. On the airfoil the transition line was at the same chord position along the span, but for the wing the transition point along the span differed depending on the chord position due to the effect of the tip vortices.

Recommendations

It is recommended, when testing a wing to begin by simulating airfoils to establish airfoil characteristics (or use data from pre-performed tests which are available for all NACA type airfoils at a range of Re). This will keep costs down in the preliminary stage until an airfoil or shortlist of suitable airfoils has been chosen. Then, simulations are recommended to be used to design the planform, before testing the planform or shortlist of planforms in a wind tunnel to verify their characteristics, as the discrepancy between simulation and experiment in the 3D case is larger than in the 2D case.

An intermediary step between XFLR5 and wind tunnel testing which is recommended (if the shortlist is still longer than is possible to test) would be to use a much more complex (but accurate) software such as ANSYS

in order to simulate the wing. Although more time and CPU intensive than XFLR5, this doesn't have the same booking limitations as the wind tunnels so is attractive for more accurate results prior to experimental testing.

In a future report on the discrepancy between simulation and test results, it would be advised to test swept wings or wings with alternative tips or flaps, or a non-symmetrical wing. This report has only shown the differences between simulation and experiment for a straight wing with a symmetric cross section and a flat tip, and as such does not show the additional discrepancies which are caused by any of the above additional characteristics.

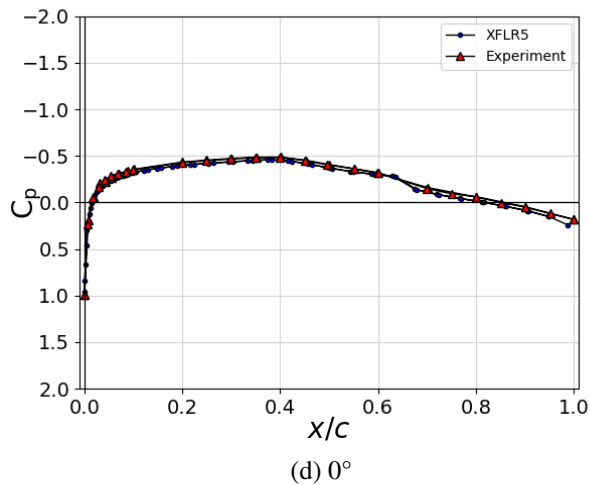
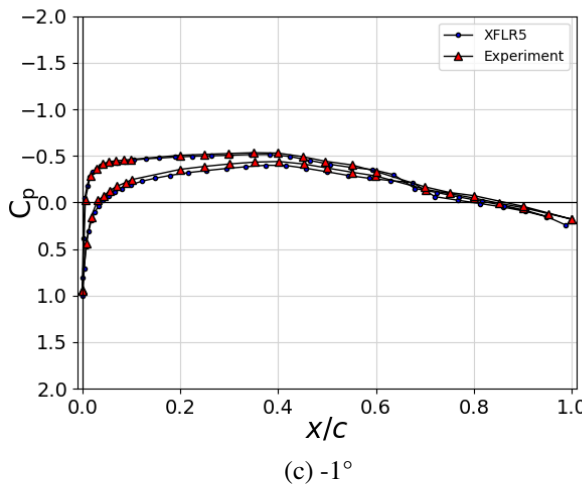
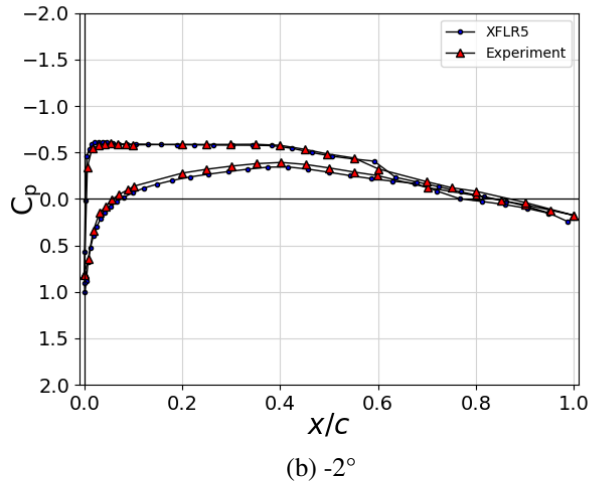
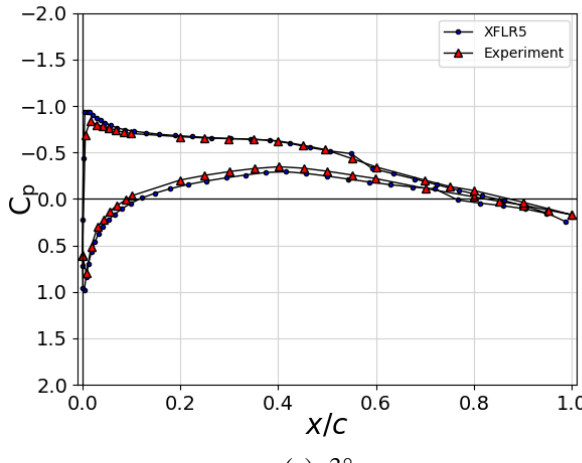
References

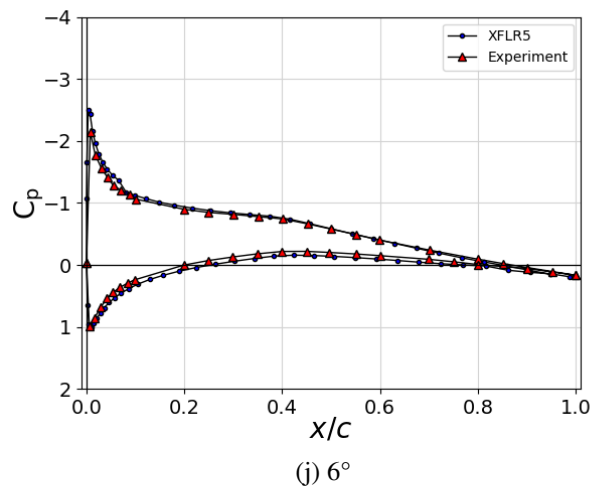
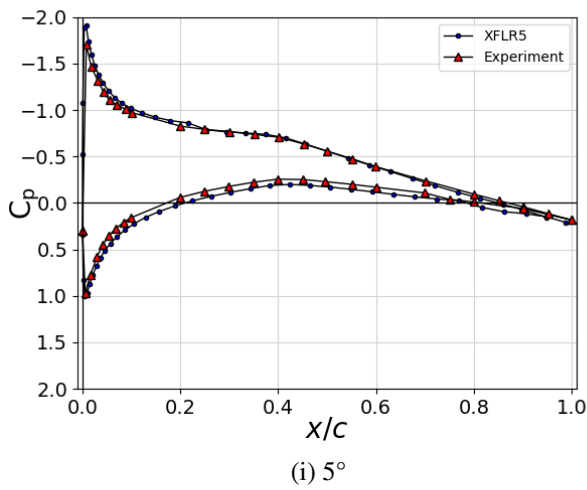
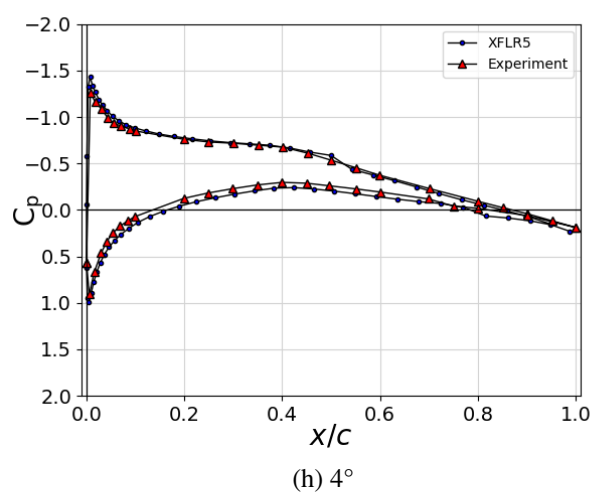
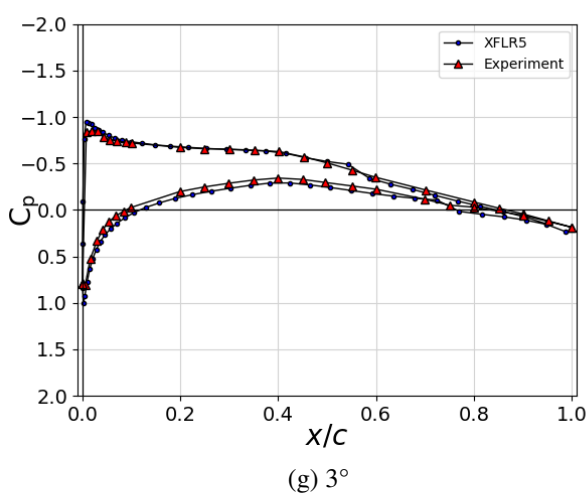
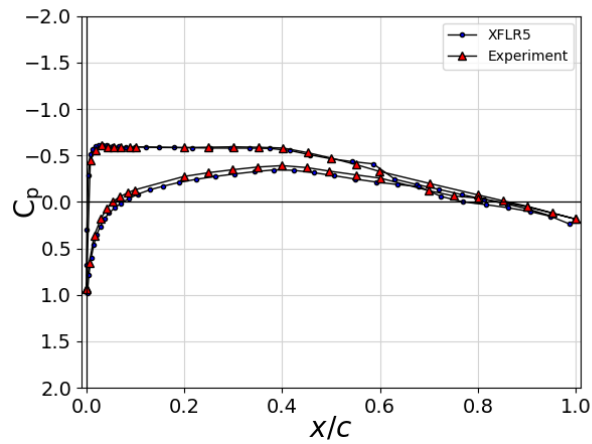
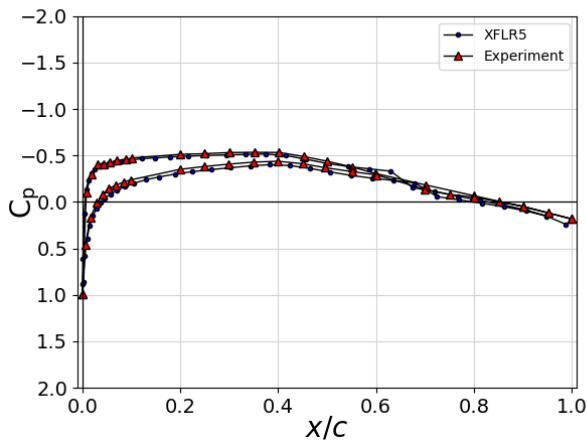
- [1] L. Veldhuis, *Manual for low speed windtunnel test (ae2130-ii)*, 1.4, TU Delft, 2016.
- [2] CSIR - National Aerospace Laboratories. (2018). “Tuft flow visualization,” [Online]. Available: <https://www.nal.res.in/en/techniques/tuft-flow-visualization#:~:text=Tuft%5C%20flow%5C%20visualization%5C%20is%5C%20a,separation%5C%2C%5C%20reattachment%5C%20and%5C%20recirculation%5C%20region..>
- [3] Scribbr. (2020). “Independent and dependent variables,” [Online]. Available: <https://www.scribbr.com/methodology/independent-and-dependent-variables/>.
- [4] M. Drela. (2013). “Xfoil,” [Online]. Available: <https://web.mit.edu/drela/Public/web/xfoil/>.
- [5] M. Gerritsma, *Aerodynamics lectures*, TU Delft, 2020.
- [6] J. Anderson, *Fundamentals of Aerodynamics*, 6th international ed. New York, United States: McGraw Hill Education, 2017.
- [7] O. Cleynen, *Horseshoe vortex*. [Online]. Available: [https://commons.wikimedia.org/wiki/File:Aircraft_wing_lift_distribution_showing_trailing_vortices_\(1\).svg](https://commons.wikimedia.org/wiki/File:Aircraft_wing_lift_distribution_showing_trailing_vortices_(1).svg).
- [8] M. Drela, *XFLR5 Analysis of foils and wings operating at low Reynolds numbers*. 2009.
- [9] A. Deperrois. (2019). “Theoretical limitations and shortcomings of xflr5,” [Online]. Available: <http://www.xflr5.tech/docs/Part%5C%20IV:%5C%20Limitations.pdf>.
- [10] J. L. van Ingen, “The en method for transition prediction: Historical review of work at tu delft,” *American Institute of Aeronautics and Astronautics*, 2008.
- [11] R. M. Cummings, W. H. Mason, S. A. Morton, and D. R. McDaniel, *Applied Computational Aerodynamics: A Modern Engineering Approach*. Cambridge University Press, 2015.
- [12] F. Oliviero, *Aerospace design and system engineering elements ii-aircraft aerodynamic fundamental analysis*. 2020.
- [13] J. Anderson, *Introduction to Flight*, 8th international ed. New York, United States: McGraw Hill Education, 2016.
- [14] N. Hall. (2015). “Aircraft rotations,” [Online]. Available: <https://www.grc.nasa.gov/www/k-12/airplane/rotations.html>.
- [15] I. Ross, “Wind tunnel blockage corrections: An application to vertical axis wind turbines,” 2010.
- [16] B. Cantwell, “The naca airfoil series.” [Online]. Available: https://web.stanford.edu/~cantwell/AA200_Course_Material/The%5C%20NACA%5C%20airfoil%5C%20series.pdf.
- [17] H. Shah, S. Mathew, and C. M. Lim, “Numerical simulation of flow over an airfoil for small wind turbines using the $\gamma - re_\theta$ model,” 2015. [Online]. Available: <https://link.springer.com/article/10.1007/s40095-015-0188-7>.
- [18] M. Selig, “Low reynolds number airfoil design lecture notes,” 2003. [Online]. Available: <https://m-selig.ae.illinois.edu/pubs/Selig-2003-VKI-LRN-Airfoil-Design-Lecture-Series.pdf>.
- [19] M. Jahanmiri, “Laminar separation bubble: Its structure, dynamics and control,” 2011. [Online]. Available: <http://publications.lib.chalmers.se/records/fulltext/138928.pdf>.
- [20] M. V. S.I. Benton, “Understanding abrupt leading edge separation as a mechanism for the onset of dynamic stall,” 2018. [Online]. Available: https://www.researchgate.net/publication/322311392_Understanding_Abrupt_Leading_Edge_Separation_as_a_Mechanism_for_the_Onset_of_Dynamic_Stall.

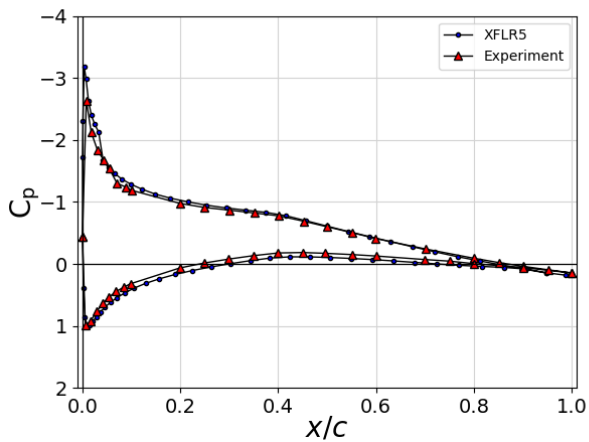
- [21] E. Thorbecke, *Synthesis of Subsonic Airplane Design*. Martinus Nijhoff Publishers, 1982.
- [22] M. Baragona, “Unsteady characteristics of laminar separation bubbles,” 2004.
- [23] Z. Yang, H. Igarashi, M. Martin, and H. Hu. 2008.
- [24] M. Drela. (2005). “Fluids - lecture 5 notes,” [Online]. Available: <https://ocw.mit.edu/courses/aeronautics-and-astronautics/16-01-unified-engineering-i-ii-iii-iv-fall-2005-spring-2006/fluid-mechanics/>.
- [25] N. Hall. (2015). “Downwash effects on lift,” [Online]. Available: <https://www.grc.nasa.gov/www/k-12/airplane/downwash.html#:~:text=If%5C%20the%5C%20atmosphere%5C%20has%5C%20very,%decreases%5C%20toward%5C%20the%5C%20wing%5C%20root..>
- [26] G. Dimitriadis, *Aircraft design, lecture 2: Aerodynamics*, 2016.
- [27] A. Deperrois, *About Stability Analysis Using XFLR5*, 2010.
- [28] A. Deperrois, *FAQ: Why do I get the message 'Point is Out of the Flight Envelope'*, 2010.

Pressure Coefficient Graphs A

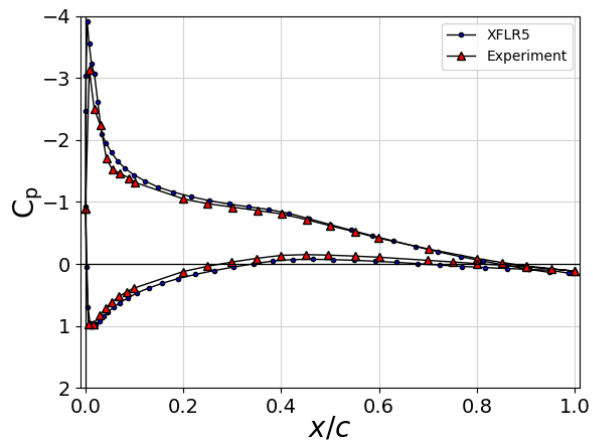
In this appendix pressure coefficient graphs for the airfoil analysis can be found. They are present in whole angles of attack.



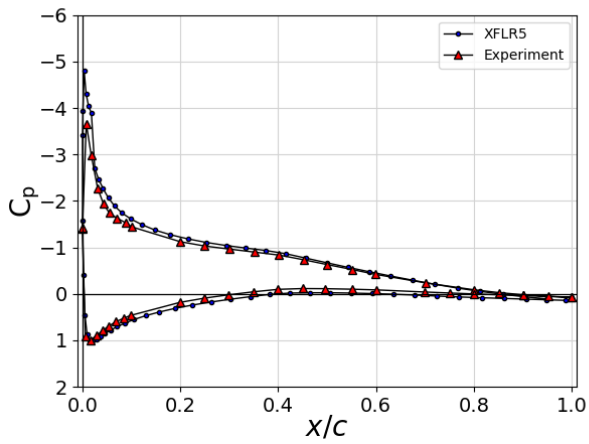




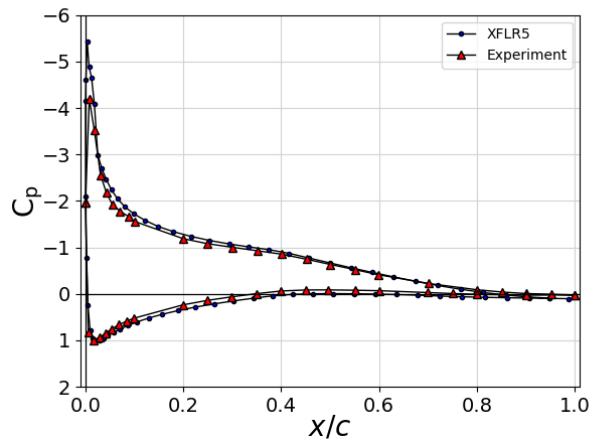
(k) 7°



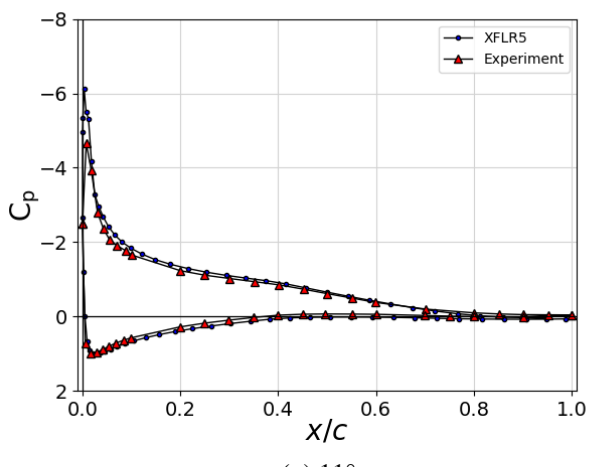
(l) 8°



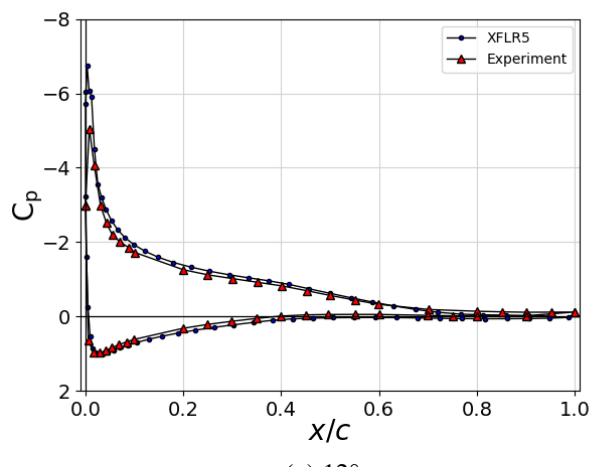
(m) 9°



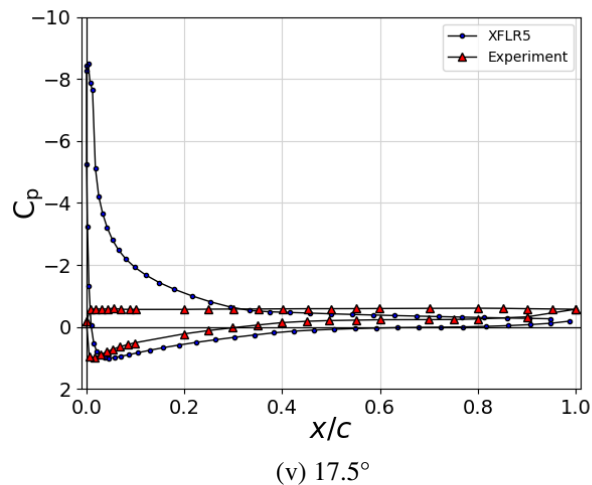
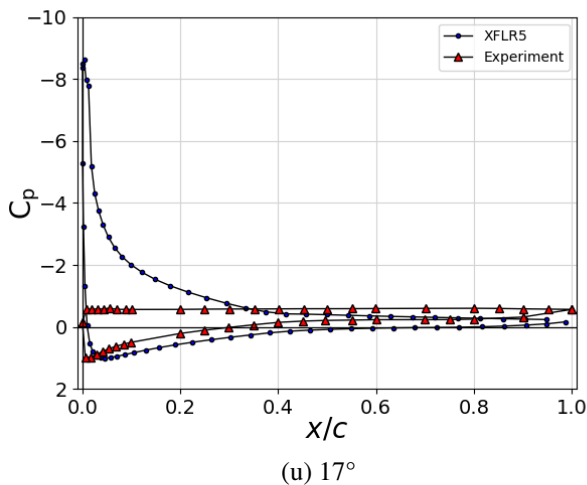
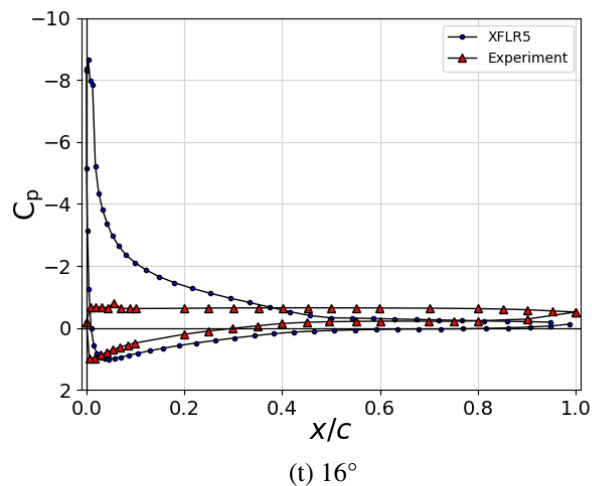
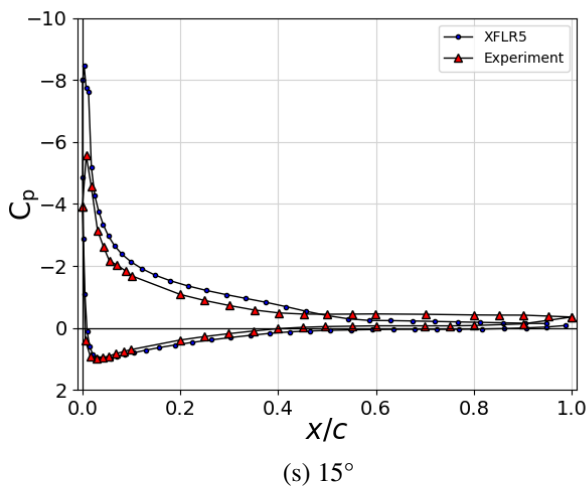
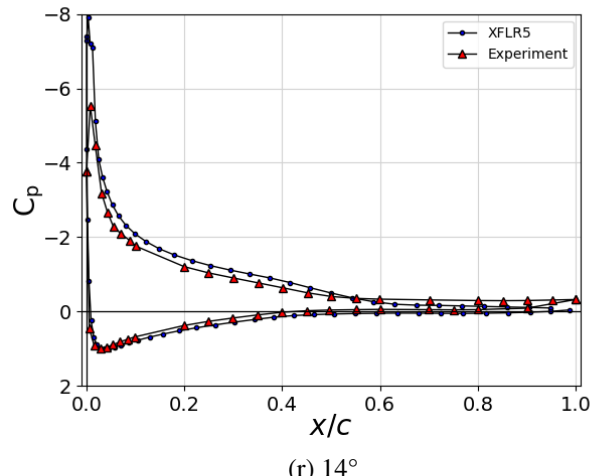
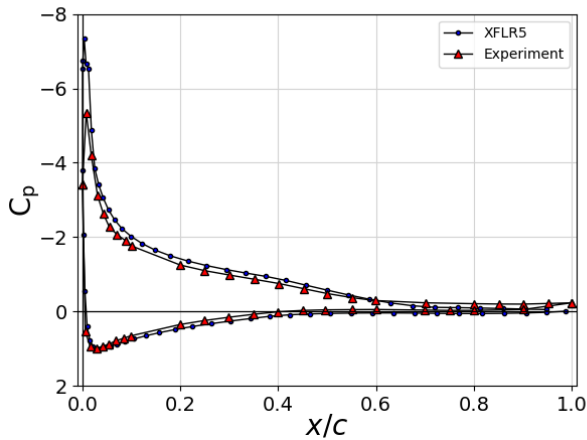
(n) 10°



(o) 11°



(p) 12°



Task Distribution

B

The following table presents the task distribution of the various deliverables present in the report.

Section	Made by	Proofread by
Summary	Eliot Watson	Bahier Khan & João Rodríguez & Niek Zandvliet & Lorenz Veithen
Introduction	Lorenz Veithen & Walid Amezguio	Bahier Khan, João Rodríguez & Eliot Watson & Niek Zandvliet
chapter 2		
section 2.1	João Rodríguez & Niek Zandvliet & Walid Amezguio	Lorenz Veithen & Anibal Luciano Pastinante
section 2.2	João Rodríguez & Niek Zandvliet & Walid Amezguio	Lorenz Veithen & Anibal Luciano Pastinante
subsection 2.2.1	João Rodríguez & Niek Zandvliet & Walid Amezguio	Lorenz Veithen
subsection 2.2.2	João Rodríguez & Niek Zandvliet & Walid Amezguio	Lorenz Veithen
section 2.3	João Rodríguez & Niek Zandvliet	Lorenz Veithen
section 2.4	João Rodríguez & Niek Zandvliet	Lorenz Veithen & Walid Amezguio
section 2.5	João Rodríguez & Niek Zandvliet	Lorenz Veithen & Walid Amezguio
chapter 3		
section 3.1	Oscar Rots	Lorenz Veithen, Anibal Luciano Pastinante & João Rodríguez
subsection 3.1.1	Oscar Rots	Lorenz Veithen, Anibal Luciano Pastinante & João Rodríguez
subsection 3.1.2	Oscar Rots	Lorenz Veithen, Anibal Luciano Pastinante & João Rodríguez
section 3.2	Bahier Khan	Lorenz Veithen, Anibal Luciano Pastinante & João Rodríguez
section 3.3		
subsection 3.3.1	Oliver Ross	Lorenz Veithen & João Rodríguez
subsection 3.3.2	Benjamin Slijper	Lorenz Veithen & João Rodríguez
chapter 4		
section 4.1	Bahier Khan	Lorenz Veithen & João Rodríguez
section 4.2	Bahier Khan	Lorenz Veithen & João Rodríguez
section 4.3	Bahier Khan	Lorenz Veithen & João Rodríguez

section 4.4	Bahier Khan	Lorenz Veithen & João Rodríguez
subsection 4.4.1	Bahier Khan	Lorenz Veithen & João Rodríguez
subsection 4.4.2	Bahier Khan	Lorenz Veithen & João Rodríguez
subsection 4.4.3	Bahier Khan	Lorenz Veithen & João Rodríguez
subsection 4.4.4	Bahier Khan	Lorenz Veithen & João Rodríguez
chapter 5		
section 5.1		
subsection 5.1.1	Bahier Khan & Oscar Rots & Eliot Watson	Oliver Ross
subsection 5.1.2	Bahier Khan & Oscar Rots & Eliot Watson	Oliver Ross
subsection 5.1.3	Bahier Khan & Oscar Rots & Eliot Watson	Oliver Ross
subsection 5.1.4	Bahier Khan & Oscar Rots & Eliot Watson	Oliver Ross & Walid Amezguio
subsection 5.1.5	Benjamin Slijper & Eliot Watson	Bahier Khan & Oliver Ross
subsection 5.1.6	Walid Amezguio & Bahier Khan & Eliot Watson	Oliver Ross & Anibal Luciano Pastinante
subsection 5.1.7	Bahier Khan	Oliver Ross & Walid Amezguio
section 5.2		
subsection 5.2.1	Lorenz Veithen	Bahier Khan, Anibal Luciano Pastinante & João Rodríguez
subsection 5.2.2	Anibal Luciano Pastinante	Bahier Khan, Anibal Luciano Pastinante & João Rodríguez
subsection 5.2.3	Oliver Ross	Bahier Khan, Anibal Luciano Pastinante & João Rodríguez
subsection 5.2.4	João Rodríguez & Niek Zandvliet	Lorenz Veithen & Anibal Luciano Pastinante & Bahier Khan & Oliver Ross
subsection 5.2.5	Anibal Luciano Pastinante & Oliver Ross	Anibal Luciano Pastinante
subsection 5.2.6	João Rodríguez & Oliver Ross	
section 5.3		
subsection 5.3.2	Anibal Luciano Pastinante	
subsection 5.3.1	Bahier Khan & Lorenz Veithen	
subsection 5.3.3	Oliver Ross	
section 5.4		
subsection 5.4.1	Anibal Luciano Pastinante & Oliver Ross	Niek Zandvliet
subsection 5.4.2	Lorenz Veithen & Oliver Ross	Niek Zandvliet
subsection 5.4.3	Lorenz Veithen	Niek Zandvliet
section 5.5	Lorenz Veithen	Oliver Ross & Niek Zandvliet
Conclusion	Bahier Khan	Eliot Watson
Recommendations	Eliot Watson	
Additional		
2D Data processing	Benjamin Slijper & Eliot Watson	
3D Data processing	Lorenz Veithen & Oliver Ross	
2D Simulations	Eliot Watson	
3D Simulations	Lorenz Veithen & Oliver Ross	
Thermal images processing	Lorenz Veithen & Niek Zandvliet	-
Sketches	Benjamin Slijper	

